EIHE 2025

Conference on Electrochemistry for Industry Health and Environment

January 21 – 25, 2025
DAE Convention Centre,
Bhabha Atomic Research Centre, Mumbai

Souvenir cum bulletin of

Indian Society for ElectroAnalytical Chemistry

Indian Society for ElctroAnalytical Chemistry
Mumbai, India
www.iseac.org.in

Volume 7, Issue 1, 2025

Souvenir Cum Bulletin of Indian Society for ElectroAnalytical Chemistry

Being released during

3rd DAE-BRNS Conference on Electrochemistry for Industry Health and Environment-2025

DAE-BRNS-EIHE-2025

January 21-25, 2025

DAE Convention Centre, Anushaktinagar,

BARC, Mumbai

Editors
A. K. Satpati
S. Manna
M. Jafar

Indian Society for ElectroAnalytical Chemistry
Mumbai, India
www.iseac.org.in

DAE-BRNS-EIHE-2025

Analytical Chemistry Division, Chemistry Group, Bhabha Atomic Research Centre &
Indian Society for Electro Analytical Chemistry (ISEAC)

Welcomes you to

DAE-BRNS-EIHE-2025

January 21-25, 2025

विवेक भसीन
Vivek Bhasin

निदेशक, भाभा परमाणु अनुसंधान केंद्र
Director, Bhabha Atomic Research Centre
सदस्य, परमाणु ऊर्जा आयोग
Member, Atomic Energy Commission

MESSAGE

Electrochemical Science and Technology is one of the frontier areas of research, which has evolved important strategies in solving several recent industrial and societal challenges, especially in relation with the energy, environment and health care. Over the years, these subject areas have grown immensely leading to applications in industrial challenges like, recovery of rare materials, investigation of corrosion and its mitigation, development of batteries, supercapacitors, solar energy harvesting devices, biomedical sensors, and fabrication of devices. Electrochemical techniques have also been utilized in the preparation and characterization of some of the advanced radiopharmaceuticals. I am glad that our Research Centre has the finest state-of-the-art facilities for this kind of frontline research and are actively pursuing developmental activities in this discipline, covering almost all of its dimensions, from laboratory scale studies to the industrial scale applications.

I am delighted to know that the 4th DAE-BRNS Conference on, "Electrochemistry for industry, Health and Environment (EIHE-2025)" is organized by Analytical Chemistry Division (ACD), Chemistry Group (CG), Bhabha Atomic Research Centre (BARC), in association with the Indian Society for Electroanalytical Chemistry (ISEAC) during January 21-25, 2025 at DAE Convention Centre, Anushaktinagar, Mumbai. Present conference has attracted participation of scientists from all over the world whose interaction with young researchers will pave the way into cutting-edge research in the days ahead.

I am sure that the deliberations of the conference will be very exciting and will offer a common platform for the intense scientific discussions and exchange of ideas amongst the young researchers in this field. It will bring out new ideas and understandings to carry forward quest for collaborative and interdisciplinary research activity in emerging frontiers.

I complement the organizers for putting forward such a technically enriched event and wish EIHE-2025 a grand success.

30.12.2024

(Vivek Bhasin)

Bhabha Atomic Research Centre

Analytical Chemistry Division

Chandra N. Patra
Head, Analytical Chemistry Division
Tel: 2559 0295 ; Fax: 2550 5151
Email: chandra@barc.gov.in

3-237-S, Mod. Labs
Mumbai 400 085

MESSAGE

Greetings and a Happy New Year 2025 from the desk of the Organizing Committee of EIHE-2025.

Electrochemical Science and allied subjects have always provided a major break-through in many industrial challenges due to its inherent association with the modern technologies and devices. Research in the field of generation of molten salt database, electrochemical metal processing, corrosion engineering and energy storage devices are some of the important projects, on which many scientific institutes are currently working on. A number of state-of-the-art instruments, fabricated using electrochemical principles ware at various stages of their operations and functioning.

On behalf of the Organizing Committee, it gives me great pleasure in welcoming you all to the to this DAE-BRNS Conference on, "Electrochemistry in Industry, Health and Environment (EIHE 2025)". The conference has been planned to provide ample opportunities to the students and young researchers to present their scientific findings and discuss along with the peers. The topic of the conference has been shortlisted considering the recent societal programs in scientific and technological challenges in Electrochemistry for Industry, Health, and Environmental Sciences.

I welcome all the invited speakers from India and abroad for attending the conference.

With great expectations from you all, let us collectively wish the conference a grand success!

Sincerely,

Cnpatra

January 10, 2025

Chandra N. Patra

Dr. Ashis Kumar Satpati
Head, Electrochemical Methods Section
Secretary, ISEAC and Convener, EIHE-2025
Bhabha Atomic Research Centre, Trombay, Mumbai 400085, Phone: 022-25590744 (O)
Email: asatpati@barc.gov.in &
aksatpati@gmail.com

Dear Delegates

Greetings!!

On behalf of the organising team, I welcome you all in this DAE-BRNS conference on "Electrochemistry for Industry, Health and Environment, EIHE-2025" at DAE Convention Centre Anushaktinagar, Mumbai durig January 21-25, 2025. I thank all of you for coming here to attend this conference.

We have tried our best to make this event technically reach, and thank you for your cooperation and enthusiasm. Since its inception, scope of the society has been broadened to cover the entire spectrum of the scientific activities in the field. I take this forum to request all of you to enhance the activities of the society and promote your colleagues and students to become the life member of this organisation.

Being stationed at Bhabha Atomic Research Centre, we enjoy the fame of this institute and excellent logistics support, we sincerely thank our authorities for their supports in making those facilities available to us. I thank Heavy Water Board (HWB), ONGC Energy Centre, International Society of Electrochemistry (ISE), American Chemical Society (ACS), Royal Chemical Society (RSC), Elsevier for supporting this event.

I am happy to announce that some selected abstracts will be published as full paper in a special volume in **Electrochimica Acta**. I wish all of you for excellent outcome from your research, ISEAC will provide all possible platform to promote your research activities. Let us join together and bring the fascinating science in the field of ***electrochemical science and technology*** to its fullest potential for the benefit of the society.

On behalf of the organising committee EIHE 2025 and the Secretary, ISEAC, I express my sincere thanks once again to DAE-BRNS, the ISEAC life members, all sponsors and the delegates of EIHE 2025.

January 10, 2025

(A K Satpati)

Since foundation, the Society has evolved magnificently to represent a truly National Organization and at present, it comprises more than 350 life-members from different parts of India and Overseas. The Executive committee of ISEAC, which manages the activities of ISEAC, is being elected triennially by all the members of ISEAC.

International Events organized by ISEAC:

ISEAC organizes International Conferences, Discussion Meets and Workshop cum Symposium on Electrochemistry and allied topics in association with the Departments of Government of India, International Society of Electrochemistry (ISE) and other Scientific Organizations and Industries. ISEAC has organized several national and International Events in India.

1. Workshop EST-2024 at Multipurpose hall, Training School Hostel, Anushaktinagar, Mumbai 400094 on during July 06, 2024.

2. International Conference on Electrochemistry in Industry Health and Environments (EIHE 2023) at DEA Convention Centre, Anushaktinagar, Mumbai during February 7-11, 2023.

3. International Conference on Electrochemistry in Industry Health and Environments (EIHE 2020) at DEA Convention Centre, Anushaktinagar, Mumbai during January 21-25, 2020.

4. Discussion meeting on Spectro electrochemistry (DM-ISEAC-2022) at Multipurpose hall, Training School Hostel, Anushaktinagar, Mumbai 400094 on 16-07-2022

5. International Conference on Electrochemistry in Advanced Materials, Corrosion and Radiopharmaceuticals (CEAMCR-2018) at DEA Convention Centre, Anushaktinagar, Mumbai during February 15-17, 2018.

6. Twelfth ISEAC Discussion Meet in Electrochemistry (12th ISEAC-DM-2016) held at The Acres Club, Chembur, Mumbai during December 7-8, 2016.

7. Eleventh ISEAC International Discussion Meet on Electrochemistry and its Applications (ISEAC-DM-2014) held at Hotel Radisson Blu, Amritsar during February 20-25, 2014.

8. Fifth ISEAC Triennial International Conference on Advances and Recent Trends in Electrochemistry (ELAC-2013) held at Sitara Hotel, Ramoji Film City, Hyderabad during January 16-20, 2013.

9. *ISEAC International Symposium cum Workshop on Electrochemistry (ISEAC-WS-2011) at Cidade de Goa, Dona Paula, Goa during December 7-10, 2011.*

10. *Fourth ISEAC International Discussion Meet on Electrochemistry and its Applications (DM-ISEAC-2011) at Mascot Hotel, Thiruvananthapuram, Kerala during February 7-10, 2011.*

11. *Fourth International Conference on ElectroAnalytical Chemistry and Allied Topics (ELAC-2013) at Toshali Sands, Puri, Orissa during March 16-18, 2010.*

12. *Discussion Meet on ElectroAnalytical Techniques and Their Applications (DM-ELANTE-2008) held at Tea County, Munnar, Kerala during February 25-28, 2008.*

13. *Third International Conference on ElectroAnalytical Chemistry and Allied Topics (ELAC-2007) at Toshali Royal View Resort, Shilon Bagh, Shimla during March 10-15, 2007.*

14. *Discussion Meet on Role of Electrochemistry in Biosensors, Nanomaterials, Fuel Cells and Ionic Liquids (DM-BNFL-2006) held at Bhabha Atomic Research Centre, Mumbai during September 24-25, 2006.*

15. *Discussion Meet on Coulometry (DM-COUL-2005) at Bhabha Atomic Research Centre, Mumbai on May 5, 2005.*

16. *Second International Conference on ElectroAnalytical Chemistry and Allied Topics (ELAC-2004) held at The International Centre, Dona Paula, Goa during January 18-23, 2004.*

17. *Workshop cum Seminar on ElectroAnalytical Chemistry and Allied Topics (ELAC-2000) held at Bhabha Atomic Research Centre, Mumbai during November 27 – December 1, 2000.*

Objectives of ISEAC:

➢ *Promote the growth of Electrochemistry in India.*

➢ *Provide a common world-wide platform to the experts, scientists and scholars working in the area of Electrochemistry and its Allied Sciences.*

➢ *Disseminate scientific and technological knowledge in the area of Electrochemistry to advance both national and international collaborations.*

➢ *Share the information on Electrochemistry with other International Societies viz. European Society for Electroanalytical Chemistry (ESEAC), Society for Electroanalytical Chemistry (SEAC) and International Society of Electrochemistry (ISE), Bioelectrochemical Society (BES).*

➢ *Work in harmony with other Indian Electrochemical Societies viz. Society for the Advancement of Electrochemical Science and Technology (SAEST) based at CECRI,*

Karaikudi and Electrochemical Society of India (ECSI) based at Indian Institute of Science, Bengaluru.

➢ *Provide incentive by way of awards to researchers for the best thesis, the best paper published in the journal and the best paper presented in National and International Conferences/Symposia.*

➢ *Encourage young as well as experienced Indian researchers for participation in International Electrochemistry Conferences by providing partial funds, if possible.*

Procedure to join ISEAC:

ISEAC has the provision for individual to join as Life-members and for company to join as Corporate Member. The Life-membership fee w.e.f. April 1, 2011 is Rs. 4000/- (Rs. Four thousand only) for Indians and € 300/- (Euro three hundred only) for others. The Fee has to be transferred electronically (NEFT or wire transfer) to ISEAC Bank Account and then you have to sign-up through "Join ISEAC as Life-Member" icon available on www.iseac.org.in with the fund transfer details.

Name of Bank: **State Bank of India, BARC Branch, Mumbai-400 085, India**
Branch code: **1268**
Beneficiary name: **Indian Society for ElectroAnalytical Chemistry (ISEAC)**
Account number: **34209997299**
BIC (Swift Code): **SBININBB508**
IFSC code (for within India): **SBIN0001268**

Please contact us for any further information:

Dr. A K Satpati
Secretary, Indian Society for ElectroAnalytical Chemistry (ISEAC)
Analytical Chemistry Division,
Bhabha Atomic Research Centre, Trombay,
Mumbai – 400 085, India
Email: electrochembarc@gmail.com;
web.: www.iseac.org.in
Phone: +91-22-2559 0744 (office hours only)

You are Welcome to Join

ISEAC

EIHE 2025

DAE-BRNS Conference on Electrochemistry for Industry, Health and Environment

January 21-25, 2025

DAE Convention Centre, BARC, Mumbai – 400094, INDIA

Email: electrochembarc@gmail.com

Organized by :	**Supported by :**
Analytical Chemistry Division, Chemistry Group, Bhabha Atomic Research Centre Mumbai – 400085, INDIA *In Association with* **Indian Society for Electroanalytical Chemistry, Mumbai**	**Board of Research in Nuclear Sciences Department of Atomic Energy Government of India**

Present conference under the series title "DAE-BRNS Conference on Electrochemistry for Industry, Health and Environment, EIHE-2025" is proposed to be organized in association with the Indian Society for ElectroAnalytical Chemistry (ISEAC) at DAE Convention Centre, Anushaktinagar, Mumbai 400094 during January 21 to 25, 2025. Excellence of electrochemistry in a wide spectrum has been included under the scope of this conference. This series of conference has been admired by national and international scientists and is expected to have a large number of eminent scientists from India and overseas attending the conference. It will be an excellent opportunity to the academia and students of the country to interact with national and international experts and widen the scope of scientific collaboration. Experts, researchers, students, and industrial units working in this interesting area of research are invited to participate.

Patron

Vivek Bhasin, Director, BARC, Mumbai

Advisory Committee

U. Kamachi Mudali (HBNI)	B. C. Pathak (NPCIL)
D. K. Shukla (AERB)	H. N. Ghosh (NISER)
C. G. Karhadkar (IGCAR)	A. K. Tyagi (HBNI)
S. Satyakumar (HWB)	Komal Kapoor (NFC)
Sudeep Gupta (TMC)	Peter Wipf (UK)
P. Mukherjee (BRIT)	R. Tewari (BARC)
U. D. Malshe (BARC)	U.W. Vaidya (BARC)
F. Marken (UK)	D. Koley (USA)
Shigeru Amemiya (USA)	S. Sampath (IISC)
C. M. A. Brett (Portugal)	S.M. Yusuf (BARC)
S. Carsten (UK)	P.A. Hassan (BARC)
M. Opallo (Poland)	A.M.O. Brett (Portugal)
D. K. Aswal (BARC)	R. Kataky (UK)
Y. K. Bhardwaj (BARC)	M. L. Mascarenhas (BARC)
K. T. Shenoy (BARC)	S. Adhikari (BARC)
P. D. Naik (ex. BARC)	S. K. Aggarwal (Mumbai)
G. Wittstock (Germany)	J. Chattopadhyay (BARC)
G. Sugilal (BARC)	Joe Mohan (BARC)

Organizing Committee

A. Kumar, A.C. Bhasikuttan & C. N. Patra (Conference Chair)	
A. Awasthi (BARC)	Krishna Mohan T.V (BARC)
S. Mukhopadhyay (BARC)	M. K. Saxena (BARC)
Tapas Das (BARC)	A. K. Singh (BARC)
A. SenthilKumar (VIT-Vellore)	R. Pai (BARC)
S. Jeyakumar (BARC)	Mario Alpuche (USA)
K. Bhanja (BARC)	P. S. Mukherjee (IISC)
Amrit Prakash (BARC)	N. Choudhary (BARC)
R. Acharya (BARC)	Kulamani Dash (BARC)
S. C. Parida (BARC)	S. Prasad (USA)
R. N. Singh (BARC)	R. J. Mascarenhas (Bengaluru)
A. Dutta (IITB)	A. Mukhopadhyay (IITB)
V. Sudarshan (BARC)	C. Bhattacharya (IIEST)
T. N. Narayanan (TIFRH)	S. Kundu (CECRI)

Local Organizing Committee

A. K. Satpati (Convener)	Subir K. Ghosh (Co-Convener)	Kothandaraman R. (Co-Convenor)	P. K. Mishra (Secretary)
M. K. Dey (Jt. Secretary)	V. T. Aher (Treasurer)	Srikant Sahoo (Jt. Treasurer)	K. K. Swain (BARC)
S. D. Kumar (BARC)	S. A. Kumar(BARC)	Manoj Neergat (IITB)	S. Shendage (KET)
N. P. Shetti (Hubballi)	P. S. Remya Devi (BARC)		M. Ghosh (BARC)
H. Basu (BARC)	Manoj K. Sharma (BARC) P. Chandra (IITBHU)	Jayashree R (BARC)	Naina R.H. (BARC)
M. Kathiresan (CECRI)	Mohsin Jafar (BARC)	Harshala Parab (BARC)	R. Gupta (BARC)
S. Manna (BARC)		Abhishek Sharma (S.M.S.L GC)	J. Kumar (BARC)

EIHE 2025

DAE-BRNS Conference on Electrochemistry for Industry, Health and Environment

Scope

→ Catalysis and interfaces
→ PEC water splitting
→ Instrumentations and devices
→ Battery, Supercapacitor, Fuel cell and Solar cell
→ Nonaqueous Electrochemistry
→ Computational Electrochemistry
→ Electrodeposition, Electrosynthesis
→ Scanning probe technique and spectroelectrochemistry
→ Electrochemistry in Pharmaceuticals and Drugs
→ Nanoscale Electrochemistry
→ Electrochemistry in Nuclear Energy
→ Electrochemical Sensors and Biosensors
→ Corrosion and mitigation

Important dates

Abstract submission

Up to 30th November, 2024

Registration

Up to 15th December, 2024

Category		Registration fee
From Universities/ Government institutes, India	Faculty	INR 5500
	Student	INR 3000
	Accompany	INR 3000
From Universities/ Government institutes, Overseas	Faculty	US$ 300
	Student	US$ 200
	Accompany	US$ 200
Industries/ Public Sectors/Private institutes	Employee/ Accompany	INR 12000

Registration fee is only accepted through Online Fund Transfer to the following account:
Name of Bank: State Bank of India, BARC Branch, Mumbai-400 085, India
Branch code: 1268
Beneficiary name: EIHE 2025
Account number: 00000043314680195
BIC (Swift Code): SBININBB508
IFSC code (for within India): SBIN0001268

Please pay the specified fees through your online banking system and then submit the registration form enclosing the transaction receipt (your name.pdf) through the conference website.
We have limited funding option for the students presenting a paper in the conference and the selection will be based on the quality of abstract. There will be poster and oral presentation awards possibly sponsored by ACS, Elsevier and RSC to encourage the students to carry out research in this area.

The delegates from abroad (holding Foreign Passport including PIO) must submit their details of valid passport (which will be carried during the event) at the earliest through email. It is mandatory to obtain Conference VISA for foreign nationals.

Registration

Registration fee includes conference proceedings, lunch & dinner during the conference. Accommodation can be arranged during January 20– 25, 2025 at the conference venue or at nearby hotels at a separate cost. The conference proceeding will be given to the primary registered delegates. Life members of ISEAC will avail a discount of INR 500 on the registration fee

How to reach

Mumbai is well connected to other parts of India and the rest of the world.

Participants arriving by train may alight at Lokmanya Tilak Terminus (LTT), Dadar, Mumbai Central, Mumbai CST or Bandra Terminus.

Participants travelling by flight will arrive at Chhatrapati Shivaji International Airport (Terminal T1 or T2)

Plenty of options for cabs are available at airports and railway stations. Delegates are advised to take prepaid cab/call cabs (UBER, OLA etc.) service at airport and railway stations.
Conference venue is at Anushaktinagar, which is also known as BARC Colony. The conference venue can also be reached by suburban trains in the harbour line and the nearest railway station is Mankhurd and the conference venue can be reached from Mankhurd by Autorickshaw. Accommodation for most of the delegates will be arranged close to the conference venue.

3rd DAE-BRNS Conference on

Electrochemistry for Industry, Health and Environment

EIHE-2025

January 21-25, 2025

DAE Convention Centre, Anushaktinagar, Mumbai – 400094, India

Organized by

Academic Partners

Programme Schedule

9:00- 10:30 hrs	:	**Registration** at *DAE Convention Centre*
10:30 – 11:45 hrs	:	**Session 1 (Auditorium A)** *Invited Lecture (20+5 minutes)*
		Chairperson: C. N. Patra
		IT-39; Prof. Deepa Khushalani **New Materials for New Batteries: Formation of Solar Rechargeable Batteries**
		IT-26; Prof. Subir Kumar Ghosh **Electrochemical Investigation of Molten Salt and Exploration of Deposition of Thick Mo and W Coatings**
		IT-45; Prof. Shilpa N Sawant **Designing electrochemical biosensors for affordable healthcare**
11:45-12:00 hrs		**Tea at Lobby**
12:00-13:30 hrs		**Session 2 (Auditorium A)** *Invited Lecture (20+5 minutes)* **Chairperson: P.D. Naik**
		IT-48; Prof. Rubel Chakravarty **Production and Electrochemical Separation of Radiometals for Formulation of Radiopharmaceuticals**
		IT-35; Prof. Jyoti Prakash **Electrochemical Energy Storage and Sensing by Carbon Nanomaterials**
		Technical Presentation by Sinsil International
13:30-14:30 hrs	:	**Lunch at dining hall, DAE Convention Centre**
14:30– 17:00 hrs		**Session 3 (Poster Session)** **Poster session (CP 1-CP 56)** at *Poster Hall*

16:30– 17:00 hrs		**Tea at Lobby**
17:00 - 18:30 hrs	:	**Inauguration of the Conference** (**Auditorium A**) **Opening of exhibition, Group photograph & High Tea**
19:00-19:40 hrs		**Evening Lecture** (**Auditorium A**) **Chairperson: A.C. Bhasikuttan**
		Speaker: Dr. Sudeep Gupta, Director, Tata Memorial Centre **"Cancer care in India - Contribution of TMC"**
20:00-21:30 hrs	:	**Dinner at dining hall, TSH, Anushaktinagar**
		January 22, 2025; Wednesday
09:30 – 11:30 hrs	:	**Session 4 (Auditorium A)** **Chairperson: A.K. Tyagi**
		Plenary Lecture **(30+5 minutes)**
		IT-30; Prof. Ritu Kataky **Electrochemical studies of Biological Interactions at Soft Interfaces**
		Invited Lecture (20+5 minutes)
		IT-15; Prof. T N Narayanan **Role of Electrolyte Structure in Heterogeneous Catalysis**
		IT-09; Dr. S. Senthil Kumar **Electrogenerated Chemiluminescence : Carbon Based Nanomaterials As An Effective Luminophores And Co-Reactants And Its Application Towards Biosensor**
		IT-12; Prof. Amit Paul **Electrochemical Dimerization of 3-Substituted-2-Oxindoles: Many Routes, One Destination**

11:30-11:45 hrs	:	**Tea** at *Lobby*
11:45–13:00 hrs	:	**Session 5 (Auditorium A)** *Invited Lecture (20+5 minutes)*
		Chairperson: H Pal & D. K. Maity
		IT-06; Prof. Stijn F. L. Mertens **Real-time Dissolution and Speciation of Manganese from Battery Electrodes during Charging and Discharging**
		IT-18; Prof. Jogendra Nath Behera **Inorganic Functional Materials for Sustainable Energy Applications**
		IT-24; Dr. M. Kathiresan **Electrochemical Conversion of CO_2 to value-added chemicals**
13:00-13:45 hrs		**Lunch at dining hall, DAE Convention Centre**
13:45-16:00 hrs		**Session 6** **Poster Presentations: CP-57** to **CP-112** at *Poster Hall*
15:30-16:00 hrs		**Tea at Lobby**
16:00–18:30 hrs		**Session 7 (Auditorium A)** *Invited Lecture (20+5 minutes)*
		Chairperson: Probal Chaudhury & R. Acharya
	:	*IT-31; Prof. A.K. Mishra* **Metal Air Batteries: Alternatives to Li-ion Batteries**
	:	*IT-07; Prof. Sasanka Deka* **Non-Precious Metal-Based Electrocatalysts for efficient Overall Water Splitting Reaction**
	:	*IT-38; Prof. Thandavarayan Maiyalagan* **Molybdenum based Electrocatalysts for Efficient and Low-cost Green Hydrogen Production**
	:	*IT-17; Prof. Bhaskar R. Sathe* **New Modifications in Electrocatalytic Hybrid materials for Water Splitting and Fuel Cell Reactions**

	:	*IT-33; Prof Pravin Popinand Ingole* **Reactive CO_2 capture and photo-electrochemical photocurrent polarity switching effect via tuning the electrochemical interfaces**
		IT-47: Prof. Ujjal Pal **Beyond Single-Atom Catalysts in Green Energy Transition**
18:30–19:00 hrs		**Tea** at *Lobby*
19:00 – 20:00hrs	:	**Cultural programme (Auditorium A)**
20:00-21:30 hrs	:	**Dinner at dining hall, DAE Convention Centre**
		January 23, 2025; Thursday
09:30–10:40 hrs	:	**Session 8 (Auditorium A)**
		Chairperson: R. Tewari
		Plenary Lecture **(30+5 minutes)**
	:	*IT-44; Prof. Shalini Prasad* **(online)** **Electrochemical Point of Care device for profiling of vWFA2 for Systemic Inflammatory State Detection**
	:	*IT-28; Prof. Sangaraju Shanmugam* **Single-Atom Electrocatalysts for Nitric Oxide Reduction to Value-Added Chemicals**
10:40–11:00 hrs	:	**Tea at *Lobby***
11:00–13:00 hrs	:	**Session 9 (Auditorium A)**
		Chairperson: Sulekha Mukhopadhyay & N. Choudhury
		Plenary Lecture **(30+5 minutes)**
		IT-29; Prof. Frank Marken **(online)** **Intrinsically Microporous Polymers in Electrochemistry**
		IT-25; Prof. Rama Kant **EIS Response for Anomalous Dynamics of EDL and Supercapacitor: Theoretical Aspects**

		Invited Lecture (20+5 minutes)
		IT-32; Prof. Partha Sarathi Mukherjee **Water-Soluble Molecular Vessels**
		IT-22; Prof. Ruma Ghosh **Reduced Graphene Oxide based Portable Sensors for PCA3**
13:00 – 13:45 hrs	:	**Lunch at dining hall, DAE Convention Centre**
13:45– 16:00 hrs	:	**Session 10** **Poster Presentations: CP-113** to **CP-168** at *Poster Hall*
15:30-16:00 hrs		**Tea at lobby**
16:00 – 18:15 hrs	:	**Session 11; (Auditorium A & Auditorium B)**

Auditorium A	Auditorium B
Chairperson: R. Pai & T. Das	**Chairperson: S. Jeyakumar & Virendra Kumar**
Short talks (12+3 mins)	*Oral presentation (8+2 mins)*
IT-43; Dr. S. Sahoo **Engineering Nano Composites for Electrochemical Sensing Applications**	**CP 3, 15, 35, 60, 82, 93, 111, 117, 121, 144, , 155, 221**
IT-20; Dr. Bholanath Mahanty **Polymeric membrane based potentiometric sensors for lanthanides and actinides**	
IT-51; V Nafees Ahmed **Feasibility study of closed loop Iodine-H2S process for Hydrogen production**	
Oral presentation (8+2 mins)	
CP 2,7, 29, 37, 46, 118, 148, 160, 215	

18:15 hrs	:	**Tea** at *Lobby*
20:00 21:30 hrs	:	**Dinner at Anushaktinagar**
		January 24, 2025; Friday
09:30 – 11:35 hrs	:	**Session 12 (Auditorium A)** *Invited Lecture (20+5 minutes)*

		Chairperson: S. Malhotra & Amrit Prakash
		IT-37; Prof. Raj Ganesh S. Pala **Catalysing Nuclear Reactions & Channelizing its energy**
		IT-10; Prof. Kothandam Krishnamoorthy **Rechargeable Batteries with Organic Polymers and Small Molecules**
		IT-19; Prof. S.T. Aruna **Indigenization of Ceramic Tapes and Substrates for Space Electronics and Electrochemical Device Applications**
		IT-36; Prof. A.K Satpati **Spectroelectrochemical investigations in Characterisation of $BiVO_4$ and Hematite interface**
		IT-34; Prof. Sandeep K C **Electrochemical Technologies for Hydrogen Economy**
11:35-11:45 hrs	:	**Tea** at *Lobby*
11:45–13:00 hrs	:	**Session 13 (Auditorium A)** *Invited Lecture (20+5 minutes)*
		Chairperson: K. Bhanja & S. Parida
		IT-51; Prof Sudhakar Prasad **Innovative Paper Electrodes for Clinical and Preclinical Diagnostics and Validation**
		IT-49; Prof. Sanghamitra Chatterjee **Effortless Devising and Theranostic Applications of Nanomaterial** **Modified Sensors: State of The Art**
		Prof. Stijn F. L. Mertens *Tutorial Lecture*
13:00 – 13:45 hrs	:	**Lunch at dining hall, DAE Convention Centre**
13:45– 16:00 hrs	:	**Session 14** **Poster Presentations: CP-169** to **CP-224** at *Poster Hall*
15:30-16:00 hrs		**Tea during poster session**
16:00 – 18:05 hrs	:	**Session 15 (Auditorium A)**

		Invited Lecture (20+5 minutes)
		Chairperson: R N Singh & A Awasthi
		IT-23; Prof. Rajesh Ganesan **Molten salt electromotive force method for thermodynamic measurements**
		IT-04; Prof. Chinmoy Bhattacharya **Effect of Dopants & Co-Catalyst in Enhancement of Photo electrochemical Applications for Microwave-assisted Synthesis of $BiVO_4$ Semiconductor**
		IT-40; Prof. Balaji P Mandal **Strategies to improve electrochemical performance of Li-S batteries**
		IT-08; Prof. Manisha Malviya **Unveiling enigmatic selenides for alkaline water splitting process**
		CP-211; Prof. R. K. Lenka **Interpretation of electrode reaction mechanism in High Temperature Steam Electrolysis cells by deconvolution of impedance spectra**
20:00 21:00 hrs	:	**Dinner at TSH, Anushaktinagar**
		January 25, 2025; Saturday
09:30 – 11:55 hrs	:	**Session 16 (Auditorium A)**
		Chairperson: G Sugilal & M L Mascarehnas
		Invited Lecture (20+5 minutes)
		IT-50; Prof. Tharamani C. Nagaiah **Designing greener energy conversion system for a sustainable future**
		Short talks (12+3 mins)
		IT-41; Dr. Jyothir Ganeshwar Reddy Ummadi **Advancing Electrochemical Sensing for Healthcare and Environmental Applications**
		IT-21; Dr Balaji B. Mulik

		Electrochemical and Catalytic Conversion CO_2 on Graphene Oxide hybrids
		IT-13; Dr. Jitendra Kumar **Application of Electrochemical and other biosensors in agricultural monitoring**
		CP-98; Dr. Anupriya Haridas **Tailoring Multi-electrolyte Additive-Mediated Electrode-Electrolyte Interphase for Stable Electrochemical Cycling of Lithium Iron Manganese Phosphate Cathodes**
		IT-46; Dr. Rahul Agarwal **Best Practices in the Evaluation of Electrochemical Kinetic Parameters for Reversible and Irreversible Redox Couples Utilizing Cyclic Voltammetry**
		IT-27; Dr. Rajini P Antony **Operando Spectro-Electrochemical Approach for Evaluating Electrochemical Interfaces Relevant to Industrial Electrolysers**
11:55– 12:10 hrs	:	**Tea** at *Lobby*
12:10 – 13:00 hrs	:	**Session 17 (Auditorium A)**
		Valedictory Function of EIHE 2025
13:00 – 13:45 hrs	:	**Lunch at dining hall, DAE Convention Centre**

Content Page

Article-1

Graphitic carbon nitride (g-C$_3$N$_4$) electrodes for energy conversion and storage technology

Sangeeta Ghosh[a], and Chinmoy Bhattacharya[a*]

a Department of Chemistry, Indian Institute of Engineering Science & Technology,(IIEST), Shibpur, Howrah – 711103, West Bengal, INDIA

⁎ Email: chinmoy@chem.iiests.ac.in; cbhattacharya.besus@gmail.com

Abstract: Graphitic carbon nitride (g-C$_3$N$_4$) has emerged as one of the most promising photocatalysts due to its metal-free nature, abundance of raw material, tunable band gap, suitable energy-band position, and thermal physical-chemical stability. The breakthrough research studies in recent years have mostly been concentrated on the engineering of the intrinsic and morphological properties of g-C$_3$N$_4$-based photocatalysts for artificial photosynthesis and environmental remediation. However, practical applications of g-C$_3$N$_4$-based electrodes and devices are still in the early stages of development owing to the difficulties in depositing high-quality and homogenous CN layer on substrates, its wide band gap, poor charge-separation efficiency, and low electronic conductivity. This review addresses the exploration of a broad spectrum of applications pertinent to g-C$_3$N$_4$-based electrodes. Although this paper is principally focused on photoelectrochemical water splitting, other emerging applications of g-C$_3$N$_4$ in solar cells and electrocatalysts are also discussed. The main challenges for CN incorporation into PEC cell are described, together with possible routes to overcome the standing limitations toward the integration of CN materials in PEC and other photoelectronic devices.

1. Introduction

Inexhaustible solar energy is considered as one promising alternative source to fulfill the increasing energy demands of human society owing to the surprisingly high consumption of finite fossil fuels [1–4]. Photocatalysis is an effective approach to harness the intermittent sunlight conversion into storable and transportable chemical fuels without emitting greenhouse

gases, for instance hydrogen gas derived from water splitting and carbon monoxide reduction into carbon-based fuels [5–11], which are practical artificial photosynthesis strategies to emulate the natural photosynthesis process and induce a predominant reliance on cleaner energy varieties to address the global energy crisis and environmental issues. However, one safety problem should not be ignored: when the water splitting reaction occurs on the surface of powdered semiconductors in a photocatalysis system, hydrogen and oxygen gases are generated in the same space, forming a potentially explosive mixed atmosphere. In view of this, it is advisable to produce hydrogen and oxygen gas in separate compartments that can be realized by utilizing photoelectrochemical (PEC) cells which was initially adopted by Fujishima and Honda in 1972 [12]. Additionally, using PEC devices is a more straightforward approach to achieve the solar-to-chemical energy goal, which just utilizes semiconductors to combine the electrocatalytic and light-absorbing functions [13]. In a semiconductor powder system, the process starts with the absorption of sunlight by the semiconductor materials in the photoanodes which can generate electron-hole pairs [14]. The electron is excited from the valence band (VB) to the conduction band (CB) to take part in the water reduction ($2H+ + 2e\_$ / H2), and the remaining hole in the VB will participate in the four-electron oxidation reactions ($2H2O /4H+ + O2 + 4e\_$) owing to the fact that the VB position should be more positive than the oxygen evolution potential [15]. It is evident that the water splitting process can be divided into three basic steps: (i) light absorption by semiconductors, (ii) the separation and transportation between electron and hole charge carriers, and (iii) the surface reactions [16]. However, in a PEC device [17], the electron will be transferred to a counter electrode by a conducting wire, and the water reduction reaction will occur at the counter electrode instead. It should be noted that at least one of the electrodes should contain semiconductor materials, and the photon energy in absorbed light must be greater than the bandgap energy (E_g) in the semiconductor materials. Three-electrode configuration combination [18] with an electrochemical workstation is generally adopted in PEC measurements to control the applied bias voltage and detection of photoresponsive current. The core of PEC devices is made of semiconductor materials with photocatalytic activity. Currently, substantial efforts have been devoted to the development of TiO_2 [19], α-Fe_2O_3 [20], $BiVO_4$ [21], ZnO [22] and many more types of photoanodes. However, for practical applications of PEC devices, it is desirable to develop much lower cost photoanodes with widely available components. In recent years, carbon nitride which is a sought-after alternative has attracted widespread attention with inestimable superiority owing to the merits of the abundant composition elements, good thermal stability,

non-toxicity, an appropriate bandgap (2.7 eV) (Fig. 2a), which is large enough to exceed the endothermic trait of the water splitting reaction, and no suffering from photo-corrosion during the water splitting process [23]. Moreover, because of not containing heavy metal ions, aged g-CN based photoanodes are very convenient to handle and dispose. In 2009, Wang et al. first proved that g-CN can be used as a metal-free photocatalyst for water splitting [24]. However, the key step in the application of g-CN in PEC devices is preparing high-quality g-CN films on conductive substrates to form g-CN photoanodes. Direct deposition of g-CN powder on substrates by using drop casting [25], spin coating [26], sol-gel [27] or vacuum filtration methods [28] cannot obtain eligible photoanodes owing to the weak adhesion between the g-CN powder and substrates. In 2010, Zhang et al. first introduced g-CN into PEC devices by depositing g-CN powder on conductive indium-doped titanium dioxide (ITO) glass substrates with only less than 1 $\mu A \ cm^{-2}$ photoresponsive current density [29]. Accordingly, this pioneering work indicated that it is imperative to develop facile approaches to fabricate high quality g-CN films which are suitable to be utilized in PEC devices as photoanodes. Moreover, besides water splitting, g-CN films also have promising widely target-specific applications that researchers have tried sporadically, such as light-emitting diodes (LEDs) [30-32], solar cells [33], electrocatalysis [34-35], and degradation [39-41]. The aim of this review is to attract the attention of many more researchers to devote themselves to the study of g-CN semiconductor which have promising potential to be a new academic hot spot in the future.

2. Basic frame work of g-C₃N₄:

The study of carbon nitride can be traced back to 1834, which was first reported by Berzelius and Liebig.[42] g-C3N4 can be fabricated by a direct pyrolysis of low-cost nitrogen-rich organic precursors, such as urea, thiourea, cyanamide, dicyanamide, melamine and so on. The main steps of the reaction pathways for various precursors with a series of polyaddition and polycondensation reactions to form g-C₃N₄, presented in Figure 1. The first four precursors can form melamine at appropriate temperatures; the melamine can polymerize into a dimer called melam at about 317°C and then rapidly react to form melem at around 390°C; the melem can further condense into one dimensional chains of amine-linked tris-s-triazine (heptazine) units called melon at 500°C, and the g-C₃N₄ structure is cross-linked via its tris-s-triazine units by trigonal nitrogen atoms polymerized completely at above 520°C. Furthermore, g-C₃N₄ will begin to gradually decompose at more than 600°C. All steps are accompanied by the evolution of NH₃. It is almost impossible for g-C₃N₄ to form a nitrogen-substituted graphene model

3

because of high instability.[43, 44] The recognized g-C$_3$N$_4$ framework of coplanar tris-s-triazine units composed of aromatic rings with alternative connections of carbon and nitrogen atoms was initially determined by Pauling and Sturdivant in 1937,[45] and this is the most stable allotrope of carbon nitride. However, we should note some facts; this structure is currently well-accepted and considered as the most stable configuration. It is very difficult to form this ideal structure totally due to the formation of the 1D chain called melon.

Two fundamental tectonic units for the formation of g-C$_3$N$_4$ allotropes are triazine C$_3$N$_3$ (melam) and tri-s-triazine/heptazine C$_6$N$_7$ (melem), with the latter having the most stable phase at ambient temperature. The excessive charge carrier recombination of g-C$_3$N$_4$, attributed to its aromatic pi system, leads to its high fluorescence. g-C$_3$N$_4$ with higher surface area via the elimination of its interplanar amino hydroxide bonding with an elevated band gap corresponding to its color change from dark yellow to light yellow. These transformations in optical properties occur due to the well-known quantum confinement effect, elevating the internal generated voltage and effectuating the transport of photogenerated electron/hole pairs. Since the exfoliation procedure merely affected the interplanar long range order bonding, the interlayer short range order bonding of aromatic heterocycles remained intact. C1s bonding that is comprised of two distinct peaks, namely sp^2 carbon–carbon bonding (C–C) or (C=C) and sp^{2}carbon atoms bonded to nitrogen (C–N=C). The N1s consists of four peaks, namely sp^2 hybridized carbon–nitrogen bonding (C–N=C), sp^3 tertiary nitrogen bonding N–(C)3 weak amino hydrogen bonded functional groups (C–N–H), and pi-excitations (Π to Π* transition).
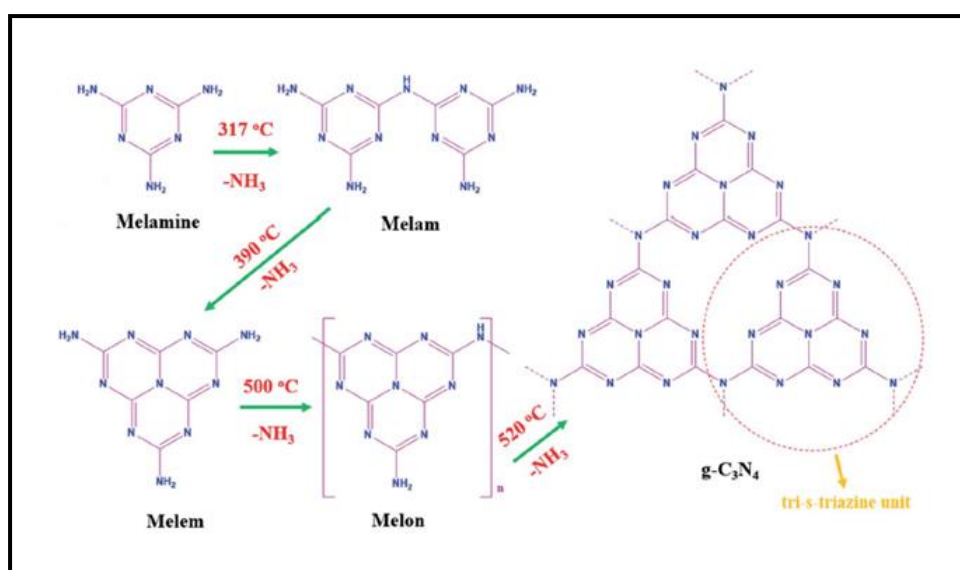
Figure 1: Reaction pathways for various precursors with a series of polyaddition and polycondensation into g-C_3N_4.

3. Mechanism of water splitting with g-C_3N_4:

Fundamental insights into the reaction mechanism for oxygen evolution, CO_2 reduction, nitrogen reduction, and oxygen reduction can pave the way for comprehending photo electrochemical devices. The reaction mechanism of g-C_3N_4 for photocatalytic water splitting was investigated by Ehrmaier et al. Hartree-Fock orbital of molecular heptazine demonstrated orbital that are exclusively localized for N and C atoms at the HOMO and LUMO, respectively. The VB of g-C_3N_4 was principally composed of N orbital while its CB was mainly comprised of C orbital (Figure 2). For molecular heptazine, upon HOMO/LUMO photo-excitation, the electron density is shifted from the N atoms to the C atoms, making the p orbital of N atoms highly electron deficient. Since the HOMO of heptazine is positioned at lower energy levels compared with the VB of liquid water, the electrons are transferred from the H atoms of hydrogen-bonded water molecules to the electron-deficient peripheral N atoms of heptazine. Consequently, the proton in water follows the electron transfer, culminating in the formation of a heterocyclic radical and OH radical in their ground states. Upon a second photo-excitation, two heterocyclic radicals can combine and produce molecular hydrogen. Substitution of heptazine with electron withdrawing groups can diminish the barrier of H atom transfer. Depletion of hydroxyl radicals in the acidic electrolyte decreases the VB of liquid water and diminishes the transfer of electrons to the HOMO of heptazine. This finding is also in harmony with other studies where g-C_3N_4 photoelectrodes achieved significantly higher photocurrent in alkaline environments compared with acidic ones.
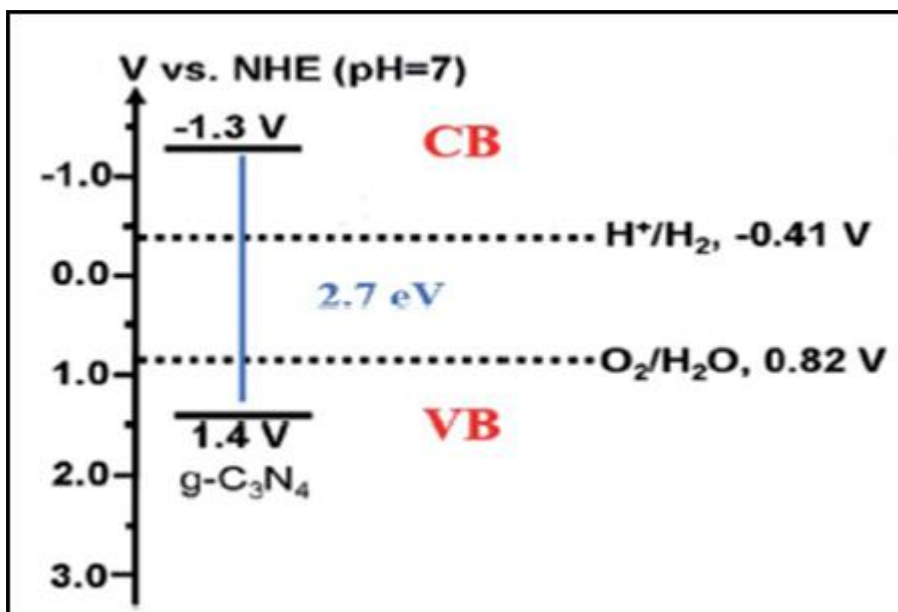
Figure 2: Electronic structure of g-C$_3$N$_4$

4. PEC water splitting and modification of g-C$_3$N$_4$:

CN materials are used as photocatalysts for both water splitting half-reactions (hydrogen and oxygen evolution reactions, HER and OER, respectively) [46] though they are mostly used for hydrogen production with various co-catalysts, dopants, and heteroatom modifications [47]. Oxygen evolution by CN materials is less common, as a result of the challenges imposed by the valence band (VB) position and the sluggish reaction kinetics. In this section, we describe the recent advances and the underlying photophysical processes involved in the successful operation of a PEC based on a photoanode composed of CN for water splitting. It is important to note that CN can also serve as the photoactive component of a photocathode [48-51]. At the end, we briefly discuss CN-based electrodes in other photodriven applications.

4.1. Light Absorption:

Light absorption is the first step in the PEC operation. Upon illumination, the photons are converted to electron–hole pairs [52]. The minimum possible band gap of a semiconductor (SC) for water splitting is 1.23 eV. However, because of both thermodynamic energy losses (0.3–0.4 eV) and the over-potential needed to overcome surface reaction kinetics (0.4–0.6 eV), an E_g of about 1.8 eV is realistic and optimal [53]. Typically, p–p* transitions in the conjugated aromatic system of CN result in $E_g \sim 2.7$ eV, that is, an absorption at λ<460 nm, which is not sufficient

6

for practical applications, owing to limited theoretical photocurrents. Thus, it is desirable to shift its absorbance toward longer wavelengths. Enhanced absorption of CN materials in the visible part of the spectrum has been obtained by the formation of p-conjugated polymers incorporating donor–acceptor structures [54-55], by copolymerization with different organic monomers [56-58], or by incorporation of different heteroatoms [59-61] and halogens [62]. The increased absorbance following the incorporation of iodine and sulfur, for example, is one of the reasons behind increased photocurrents. In general, the E_g of CN materials can be easily tuned by changing their C/N ratio or their spatial organization. However, the limited control over the deposition of CN powders onto electrodes hinders the capacity of applying the knowledge obtained from CN powders to PEC photoelectrodes. Niu et al. proved that by controlling the condensation temperature of CN precursors, nitrogen vacancies could be induced, resulting in additional absorption bands from 450 to 600 nm. At sufficiently high temperatures, the thermal annealing of CN films prepared by TVC induced the removal of N atoms from the triazine units, and theoretical calculations confirmed the formation of new C=C p-bonds upon N release. This modification of the energy levels combined with increased conductivity resulted in the doubling of the photocurrent density of annealed CN films. Tailored monomer design is another method for influencing the electronic properties of CN-films, thus tuning the optical absorption window so that a higher fraction of the solar spectrum is harvested. With the addition of a C-rich molecule in the supramolecular complex used as a precursor, a red-shift in the optical absorbance of the resulting CN films was observed, as a result of the replacement of some nitrogen atoms with carbon. This effect led to a two-fold photocurrent increase, from 3 to 6 mA cm^{-2}. Adding 2,6-diaminopyridine as a co-monomer while using the TVC method was also shown to increase the C content in CN films, which afforded films with an enhanced and red-shifted absorption. The introduction of sp^2 carbons within the structure resulted in a fourfold photocurrent increase, reaching an external quantum efficiency of 16% at 400 nm. Xu et al. showed that the introduction of an intermediate level near the VB leads to enhanced photocurrents due to enhanced absorption and better hole extraction properties.

4.2. Charge Transport in CN:

In water-splitting PECs, the oxidation (at the anode) and reduction (at the cathode) are performed simultaneously but are spatially separated. In the common photoanode setup, the electron–hole pair generated throughout the active layer must separate and migrate to their

appropriate positions. The hole oxidizes water at the surface (at the liquid junction), while the electron must travel to the conductive electrode and participate in the reduction reaction at the liquid junction on the surface of the cathode. While increasing the thickness of the active layer results in increased light absorption, this also results in higher recombination rates between electron and holes in the VB or surface states. This trade-off is crucial in the PEC performance and is limited by light absorption and charge extraction properties. Contrary to the case of graphene and other layered materials, Merschjann et al. [63] showed that in CN the charge transport occurs along channels perpendicular to the graphitic sheet and that the electrons and holes show high mobility, implying that perpendicular charge mobility should also be sufficient in a layered CN structure.

Currently, the CN-PEC efficiency is still low, owing to the fast recombination of photoexcited charges (Figure 3a), poor electron and hole diffusion, and the existence of defects, which lead to deep trap states and form a kinetic barrier for hole extraction to the electrolyte. To overcome these limitations, several photoanode configurations with theoretically enhanced performances have been proposed (Figure 3). An electron acceptor layer (EAL) was utilized (Figure 3a) to increase the ability of photoexcited charges to react according to the desired pathway [64]. Transient absorption spectroscopy (TAS) measurements show that the charge injection rate from CN into TiO_2 is in the nanosecond regime and three orders of magnitude faster than the back-recombination rate. However, it was found that the hole extraction rate is limiting the overall performance of the PEC [65]. The incorporation of nano-structured electron-transporting paths, such as nanowires and nanotubes, within the active layer decouples light absorption from charge-carrier migration. In this case, the recombination is further hindered by the EAL since the necessary electron diffusion lengths are shorter than the thickness of the absorbing CN layer. CN on the surface of TiO_2 nanorods resulted in 21-fold photocurrent increase relative to bare CN [66]. Similar trends were also found for TiO_2 nanotubes modified with CN [67], or phosphorous-doped CN, where the increased performance was ascribed to longer electron lifetimes in the active material [68]. CN on the surface of ZnO nanowires study, the CN layer acted as an efficient hole extraction layer rather than as an absorber. Carbon-based nanostructures such as reduced graphene oxide (rGO), carbon nanotubes (CNT), and others can also serve as electron conduction paths. Constructing a type II heterojunction between a semiconductor (SC) and CN (Figure 3b) has similar electronic advantages to those arising from interfacing CN with EAL, as well as an improved light collection if the second SC has a

narrower band gap to that of the CN. This was demonstrated when CN sheets were mixed with $BiVO_4$ nanoparticles (Eg ~ 2.53 eV), which resulted in a 10-fold photocurrent increase, as well as with other vanadates, and with hematite. The type II energy band alignment can be also achieved by depositing two or more CN layers with different band gaps. Tang and co-workers showed that the construction of a boron-doped CN/CN heterojunction can lead to a significant enhancement of the photocurrent thanks to improved charge separation and charge transfer within the electrode.

One of the major limitations of CN-PEC performance is the poor electronic conductivity of the CN layer. It leads to a high charge recombination rate and to a very low diffusion length. The latter limits the thickness of the active harvesting layer and therefore restricts light absorption. Increasing the amount of C=C bonds in the CN structure is one way to improve its conductivity. Recently, it was shown that C=C bonds can be introduced by selecting the appropriate monomer precursors. The new C=C bonds within the CN structure have synergetic positive effects, namely improved electron conductivity and red-shift of the absorption onset. Another method to circumvent the poor electron conductivity is the previously mentioned hybridization of CN with conductive materials that serve as conduction paths. In that case, the electrons are immediately transferred into the conductive layer, which acts as current collector. Very recently, we succeeded in synthesizing CN/rGO films on FTO from the thermal condensation of a supramolecular organized mixture of CN monomers with graphene oxide that was cast on FTO by a doctor blade coating process. Our results point out that the optimal layer thickness is 36 mm, that is, that electron can effectively diffuse this distance without recombining with holes. The long diffusion length resulted in only a small amount of recombination of photoexcited charges and improved light-harvesting properties, leading to a substantial photocurrent enhancement compared to the pristine one [69]. To improve light-harvesting properties and the charge separation of excited charges, a porous electrode structure can be used. The porous structure enables high loading of CN and direct contact with the electrolyte. In the case of dye sensitized-like structure, the electrons are being injected into the porous semiconductors and holes are extracted to the electrolyte. Therefore, the lifetime of excited charges is extended and the PEC displays a better photoactivity.
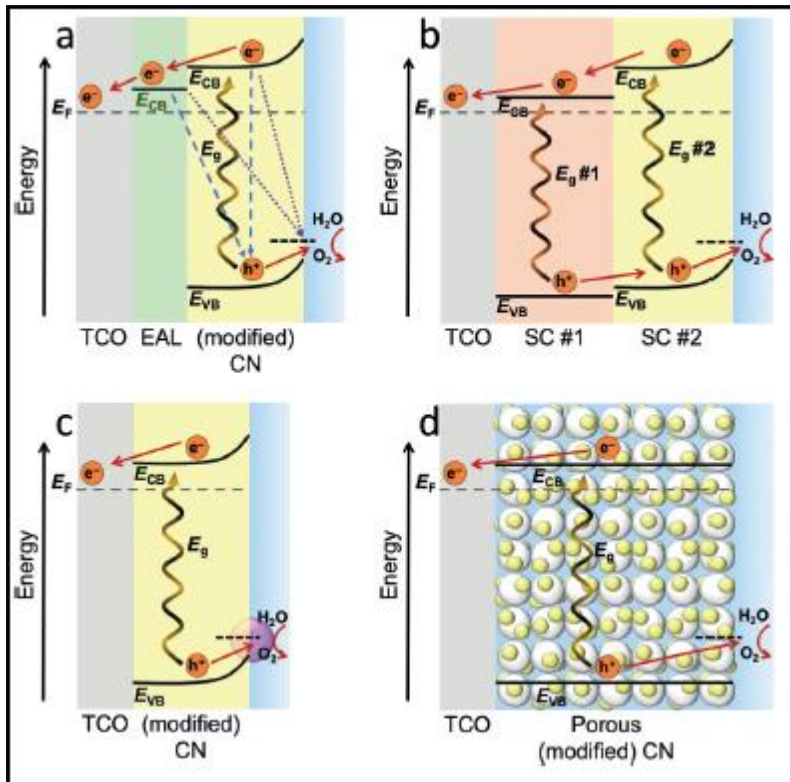
Figure 3. Advanced photoanode interfaces: a) an electron-accepting layer (EAL) between the transparent conductive electrode (TCO) and the CN. b) Type II heterojunction with two semiconductor (SC) materials. c) Co-catalyst at the CN-liquid junction interface. d) Porous CN layer.

4.3. Surface Reaction Kinetics:

In a photoanode, water oxidation on the SC surface is considered as the bottleneck. The introduction at the solid–liquid interface of a co-catalyst that can both act as a sink for holes from the CN and serve as the catalytic spot for oxygen evolution was proven to be a successful approach (Figure 3c). Transition metals and their compounds are the typical co-catalysts for CN. For example, Qiao et al. found that, thanks to the coordination of cobalt to the N atoms of CN, the Co-C$_3$N$_4$/CNT system resulted in improved electrocatalytic OER performance [70]. Zhang et al. inserted Co into the framework of CN via chemical interaction. The surface junction modification accelerates the photocatalytic OER kinetics, enhances light harvesting, and accelerates charge transfer [71]. Embedding Co^{2+} within CN doubled the photocurrent and lowered the water oxidation over potential of a PEC [72]. Ni-doped CN afforded much higher photocurrent compared to the pristine CN electrode, which is attributed to the superior catalytic

activity of Ni as well as increased light absorption. TAS measurements indicate that the holes are concentrated in the Ni co-catalyst, further facilitating the charge separation within the CN electrodes, and that holes were efficiently extracted by the electrolyte. The deposition of CoO_x onto the surface of CN is more efficient at facilitating OER than bulk doping in terms of increasing the number of active sites, lowering the over-potential, and accelerating the interface charge mobility [73]. Metal phosphides, such as CoP [74] and NiCoP [75], constitute another potential class of OER co-catalysts. To improve both charge transportation within the absorbing layer and sluggish OER reaction kinetics, Chen and coworkers developed a ternary hybrid gel composed of N deficient porous CN, N-doped rGO, and NiFe-layered double hydroxide (LDH). Hole scavengers are sacrificial materials that have suitable energy levels and fast oxidation kinetics, thus lower the over-potential. Na_2S, alcohols, and amines are some popular hole scavengers that lead to enhanced PEC performance.

4. Summary and outlook:

PEC devices for water oxidation have been intensively investigated in the past few decades. The balance between cost and performance is a decisive factor for commercial applications. Although metal containing semiconductors exhibit good PEC performance, the high cost owing to the raw materials or complicated fabrication process impedes the practical commercialization. Metal-free g-CN is a suitable candidate which has attracted much attention in the past several years. In this review, the basic knowledge on PEC cells is presented with new perspective on the structure of g-CN.

As a bulk material, CN can meet the requirements of a photoanode with suitable light-harvesting properties, stability under operational conditions, and appropriate energy band positions. However, in practice, there is still a long way to go before CN materials can become a real alternative to state-of-the-art semiconductors. To achieve a substantial progress in the implementation of CN materials and to obtain efficient photoelectric devices, several important issues should be resolved. Based on the above-mentioned considerations, a significant advancement of this topic requires addressing the following points:

(A) Decreasing the band gap of CN: This would result in increased light harvesting and photocurrent density. It can be achieved by optimizing the C/N ratio and the spatial organization of the N atoms in the final material and/or by doping with heteroatoms.

(B) Suppression of photoexcited charges recombination and efficient carrier separation and transportation: The conductivity of electrons can be improved by replacing some C=N with C=C bonds or by doping with heteroatoms/metals.

(C) Passivation of layer through defect formation: The chemistry of CN materials can lead to the formation of many defects below the CB. CB electrons may be trapped in these states and may eventually recombine with holes in the VB. In a layer, these defects may act as recombination centers that hinder the conductivity and the final performance. Therefore, the CN layer passivation along with better crystallinity will play an important role in the activity enhancement. This may be achieved by recrystallization on a substrate, and by careful design of synthetic procedure.

(D) Fast reaction kinetics at the CN/electrolyte interface and long-term stability: For most of the recently reported high performance PEC, the best configuration often comprises a semiconductor and OER co-catalysts (at the photoanode). However, as CN-PECs are still at the early stage of their development, only a few works reporting the use of co-catalysts with the CN layer have been published. There are several factors that should be considered when integrating a co-catalyst onto a CN layer. The first issue is the nature of the contact, which varies with different types of co-catalysts and alters the transport of charges across the CN/electrolyte interface. Furthermore, the electronic properties of the co-catalyst must match the VB structure of the CN for efficient hole transfer. Since most of the research thus far has focused on CN materials for reduction reactions (for example, hydrogen and CO_2 reduction), it has mainly dealt with electron transfer co-catalysts; only a few works regarding water oxidation co-catalysts have been reported. Despite this, an already wide range of electrocatalysts with high OER activity has emerged over the last years; thus, we believe that suitable co-catalysts can and will be found. To evaluate the performance of CN-PECs, their long-term stability should be studied. In this case, using both a co-catalyst and a protective layer is possible.

(E) Gaining a fundamental understanding about photoelectrochemical, charge-separation and transfer processes, and at a later stage their relationships with structural, chemical, and photophysical properties: The lack of basic knowledge regarding the CN layer properties impedes the ability to improve their PEC performance. Therefore, advanced spectroscopy methods such as transient absorption spectroscopy, time-resolved fluorescence measurements,

and time-resolved microwave conductivity etc. may be helpful to shed more light on the involved photoelectrochemical processes.

To summarize, although there are many obstacles hindering the use of carbon nitride materials in photoelectrochemical devices, we believe that their unique properties and broad chemistry will make it possible to overcome the current difficulties and limitations. Furthermore, developing tools for the synthesis of CN layers on substrates, together with advancements in the understanding of the photophysical and photoelectrochemical properties, may result in their exploitation in solar cells, light-emitting diodes, and sensors.

Acknowledgement:

References:

1. W. J. Ong, L. L. Tan, Y. H. Ng, S. T. Yong and S. P. Chai, Chem. Rev., 116, (2016) 7159-7329.

2. H. Wang, X. D. Zhang and Y. Xie, Mater. Today, 23 (2019) 72-86.

3. G. P. Dong, Y. H. Zhang, Q. W. Pan and J. R. Qiu, J. Photochem. Photobiol., C, 20, (2014) 33-50.

4. W. J. Jiang, W. J. Luo, J. Wang, M. Zhang and Y. F. Zhu, J. Photochem. Photobiol., C, 28, (2016) 87-115.

5. S. B. Wang, B. Y. Guan and X. W. D. Lou, J. Am. Chem. Soc., 140 (2018) 5037-5040.

6. S. Zhang, J. Liu, X. Dong, X. Jia, Z. Gao and Q. Gu, Sustainable Energy Fuels, 3, (2019) 2742-2752.

7. S. B. Wang, B. Y. Guan, X. Wang and X. W. D. Lou, J. Am. Chem. Soc., 140 (2018) 15145-15148.

8. S. B. Wang, B. Y. Guan, Y. Lu and X. W. Lou, J. Am. Chem. Soc., 139 (2017) 17305-17308.

9. A. Miyoshi, J. J. M. Vequizo, S. Nishioka, Y. Kato, M. Yamamoto, S. Yamashita, T. Yokoi, A. Iwase, S. Nozawa, A. Yamakata, T. Yoshida, K. Kimoto, A. Kudo and K. Maeda, Sustainable Energy Fuels, 2 (2018) 2025-2035.

10. S. Wang, Y. Wang, S. L. Zhang, S.-Q. Zang and X. W. Lou, Adv. Mater., 31 (2019) 1903404.

11. S. P. Adhikari, Z. D. Hood, V. Chen, K. L. More, K. Senevirathne and A. Lachgar, Sustainable Energy Fuels, 2 (2018) 2507-2515.

12. J. Q. Wen, J. Xie, X. B. Chen and X. Li, Appl. Surf. Sci., 391 (2017) 72-123.

13. K. Sivula and R. van de Krol, Nat. Rev. Mater., 1 (2016) 15010.

14. R. Abe, J. Photochem. Photobiol., C, 11 (2010) 179-209.

15. Y. B. Kuang, T. Yamada and K. Domen, Joule, 1 (2017) 290-305.

16. Y. Tachibana, L. Vayssieres and J. R. Durrant, Nat. Photonics, 6, (2012) 511-518.

17. J. Jian, G. S. Jiang, R. van de Krol, B. Q. Wei and H. Q. Wang, Nano Energy, , 51, (2018) 457-480.

18. M. Volokh, G. Peng, J. Barrio and M. Shalom, Angew. Chem., Int. Ed., 58 (2019) 6138-6151.

19. A. B. Barrientos, X. B. Li, S. Yick, A. F. Masters and T. Maschmeyer, Sustainable Energy Fuels, 2 (2018) 1463-1473.

20. J. F. Zhang and S. Eslava, Sustainable Energy Fuels, 3 (2019) 1351-1364.

21. S. Iguchi, Y. Miseki and K. Sayama, Sustainable Energy Fuels, 2 (2018) 155-162.

22. X. F. Long, F. Li, L. L. Gao, Y. P. Hu, H. G. Hu, J. Jin and J. T. Ma, ChemSusChem, 11, (2018) 4094-4101.

23. Y. Zheng, L. H. Lin, B. Wang and X. C. Wang, Angew. Chem., Int. Ed., 54 (2015) 12868-12884.

24. X. C. Wang, K. Maeda, A. Thomas, K. Takanabe, G. Xin, J. M. Carlsson, K. Domen and M. Antonietti, Nat. Mater., 8 (2009) 76-80.

25. S. Lou, Z. X. Zhou, Y. F. Shen, Z. S. Zhan, J. H. Wang, S. Q. Liu and Y. J. Zhang, ACS Appl. Mater. Interfaces, 8 (2016) 22287-22294.

26. J. Safaei, N. A. Mohamed, M. F. M. Noh, M. F. Soh, M. A. Riza, N. S. M. Mustakim, N. A. Ludin,

M. A. Ibrahim, W. N. R. W. Isahak and M. A. M. Teridi, J. Alloys Compd., 769, (2018) 130-135.

27. J. S. Zhang, M. W. Zhang, L. H. Lin and X. C. Wang, Angew. Chem., Int. Ed., 54 (2015) 6297-6301.

28. H. Miao, G. W. Zhang, X. Y. Hu, J. L. Mu, T. X. Han, J. Fan, C. J. Zhu, L. X. Song, J. T. Bai and X. Hou, J. Alloys Compd., 690 (2017) 669-676.

29. Y. J. Zhang and M. Antonietti, Chem. Asian J., 5 (2010) 1307-1311.

30. J. S. Xu, M. Shalom, F. Piersimoni, M. Antonietti, D. Neher and T. J. K. Brenner, Adv. Opt. Mater., 3 (2015) 913-917.

31. R. Y. Babkin, K. V. Lamonova, S. M. Orel, A. M. Prudnikov, Y. G. Pashkevich, O. V. Gornostaeva, O. G. Viagin, P. O. Maksimchuk and Y. V. Malyukin, J. Lumin., 186 (2017) 247-254.

32. Y. Xiao, M. S. Chen and M. L. Zhang, Chem Photo Chem, 3 (2019) 101-106.

33. J. S. Xu, T. J. K. Brenner, L. Chabanne, D. Neher, M. Antonietti and M. Shalom, J. Am. Chem. Soc., 136 (2014) 13486-13489.

34. M. Shalom, S. Gimenez, F. Schipper, I. Herraiz-Cardona, J. Bisquert and M. Antonietti, Angew. Chem., Int. Ed., 53 (2014) 3654-3658.

35. Y. Kikuchi, X. J. Chang, Y. Sakakibara, K. Y. Inoue, T. Matsue, T. Nozawa and S. Samukawa, Carbon, 93 (2015) 207-216.

36. Y. Y. Bu, Z. Y. Chen, J. Q. Yu and W. B. Li, Electrochim. Acta, 88 (2013) 294-300.

37. J. H. Thurston, N. M. Hunter and K. A. Cornell, RSC Adv., 6 (2016) 42240-42248.

38 J. H. Thurston, N. M. Hunter, L. J. Wayment and K. A. Cornell, J. Colloid Interface Sci.,505 (2017) 910-918.

39. L. Xu, H. N. Li, P. C. Yan, J. X. Xia, J. X. Qiu, Q. Xu, S. Q. Zhang, H. M. Li and S. Q. Yuan, J. Colloid Interface Sci., 483 (2016) 241-248.

40. Z. S. Zhang, S. L. Lin, X. G. Li, H. Li and W. Q. Cui, RSC Adv., 7 (2017) 56335-56343.

41. F. H. Jia, Y. Z. Zhang, W. J. Hu, M. Lv, C. C. Jia and J. Liu, Front. Mater., 6 (2019) 52.

42. X. C. Wang, S. Blechert and M. Antonietti, ACS Catal., 2 (2012) 1596-1606.

43. Z. M. Shi, A. Kutana and B. I. Yakobson, J. Phys. Chem. Lett., 6 (2015) 106-112.

44. S. G. Zhang, S. Tsuzuki, K. Ueno, K. Dokko and M. Watanabe, Angew. Chem., Int. Ed., 54 (2015) 1302-1306.

45. L. Pauling and J. H. Sturdivant, Proc. Natl. Acad. Sci. U. S. A., 1937, 23, 615-620.

46. G. Zhang, Z.-A. Lan, L. Lin, S. Lin, X. Wang, Chem. Sci., 7 (2016) 3062-3066.

47. S. Cao, J. Yu, J. Phys. Chem. Lett., 5 (2014) 2101-2107.

48. F. Yang, M. Lublow, S. Orthmann, C. Merschjann, T. Tyborski, M. Rusu, S. Kubala, A. Thomas, R. Arrigo, M. H-vecker, et al., ChemSusChem, 5 (2012) 1227-1232.

49. J. Wang, C. Zhang, Y. Shen, Z. Zhou, J. Yu, Y. Li, W. Wei, S. Liu, Y. Zhang, J. Mater. Chem. A , 3 (2015) 5126-5131.

50. Y. Y. Han, X. L. Lu, S. F. Tang, X. P. Yin, Z. W. Wei, T. B. Lu, Adv. Energy Mater., 8 (2018) 1702992.

51. M. Basu, Z. W. Zhang, C. J. Chen, T. H. Lu, S. F. Hu, R. S. Liu, ACS Appl. Mater. Interfaces 8 (2016) 26690-26696.

52. X. Chen, S. Shen, L. Guo, S. S. Mao, Chem. Rev., 110 (2010) 6503-6570.

53. A. B. Murphy, P. R. F. Barnes, L. K. Randeniya, I. C. Plumb, I. E. Grey, M. D. Horne, J. A. Glasscock, Int. J. Hydrogen Energy, 31 (2006) 1999-2017.

54. R. S. Sprick, J. X. Jiang, B. Bonillo, S. Ren, T. Ratvijitvech, P. Guiglion, M. A. Zwijnenburg, D. J. Adams, A. I. Cooper, J. Am. Chem. Soc., 137 (2015) 3265-3270.

55. G. Zhang, Z. A. Lan, X. Wang, Angew. Chem. Int. Ed., 55 (2016) 15712-15727;

56. A. B. Murphy, Angew. Chem., 128 (2016) 15940-15956.

57. J. Zhang, X. Chen, K. Takanabe, K. Maeda, K. Domen, J. D. Epping, X. Fu, M. Antonietti, X. Wang, Angew. Chem. Int. Ed. 49 (2010) 441-444

58. J. Zhang, G. Zhang, X. Chen, S. Lin, L. Mçhlmann, G. Dołęga, G. Lipner, M. Antonietti, S. Blechert, X. Wang, Angew. Chem. Int. Ed., 51 (2012) 3183-3187.

59. W. Ho, Z. Zhang, W. Lin, S. Huang, X. Zhang, X. Wang, Y. Huang, ACS Appl. Mater. Interfaces, 7 (2015) 5497-5505.

60. G. Liu, P. Niu, C. Sun, S. C. Smith, Z. Chen, G. Q. (Max) Lu, H. M. Cheng, J. Am. Chem. Soc., 132 (2010) 11642-11648.

61. S. C. Yan, Z. S. Li, Z. G. Zou, Langmuir, 26 (2010) 3894-3901.

62. M. Jourshabani, Z. Shariatinia, A. Badiei, Langmuir, 33 (2017) 7062-7078.

63. G. Zhang, M. Zhang, X. Ye, X. Qiu, S. Lin, X. Wang, Adv. Mater., 26 (2014) 805-809.

64. C. Merschjann, S. Tschierlei, T. Tyborski, K. Kailasam, S. Orthmann, D. Hollmann, T. Schedel Niedrig, A. Thomas, S. Lochbrunner, Adv. Mater., 27 (2015) 7993-7999.

65. T. J. Park, R. C. Pawar, S. Kang, C. S. Lee, RSC Adv., 6, (2016) 89944-89952.

66. J. Albero, E. M. Barea, J. Xu, I. Mora-Serl, H. Garcia, M. Shalom, Adv. Mater. Interfaces, 4 (2017) 1600265.

67. X. Fan, T. Wang, B. Gao, H. Gong, H. Xue, H. Guo, L. Song, W. Xia, X. Huang, J. He, Langmuir 32 (2016) 13322-13332.

68. X. Zhou, F. Peng, H. Wang, H. Yu, Y. Fang, Chem. Commun., 47 (2011) 10323.

69. G. Peng, M. Volokh, J. Tzadikov, J. Sun, M. Shalom, Adv. Energy Mater., 8, (2018) 1800566.

70. Y. Zheng, Y. Jiao, Y. Zhu, Q. Cai, A. Vasileff, L. H. Li, Y. Han, Y. Chen, S.-Z. Qiao, J. Am. Chem. Soc., 139 (2017) 3336-3339.

71. G. Zhang, C. Huang, X. Wang, Small, 11 (2015) 1215-1221.

72. Z. Chen, H. Wang, J. Xu, J. Liu, Chem. Asian J. 2018, 13, 1539-1543.

73. G. Zhang, S. Zang, L. Lin, Z.-A. Lan, G. Li, X. Wang, ACS Appl. Mater. Interfaces, 8 (2016) 2287-2296.

74. Z. Pan, Y. Zheng, F. Guo, P. Niu, X. Wang, ChemSusChem, 10 (2017) 87-90.

75. Z. Qin, Y. Chen, Z. Huang, J. Su, L. Guo, J. Mater. Chem. A, 5 (2017) 19025-19035.

Article-2

Improved Methylene Blue Adsorption on Biomass-Derived Carbon Quantum Dots/Nafion Composite for Electrochemical Applications

Jayaprakash Meena [a,b], Z. Waseem Basha [c], S. Muniraj [c], K. Santhakumar [b] and Annamalai Senthil Kumar [a,b*]*

[a] Nano and Bioelectrochemistry Research Laboratory, Carbon Dioxide and Green Technology Research Centre and Department of Chemistry, School of Advance Science, Vellore, Institute of Technology University, Vellore- 632 014[*], Tamil Nadu, India.

[b] Department of Chemistry, School of Advanced Sciences, Vellore Institute of Technology University, Vellore – 632 014, Tamil Nadu, India.

[c] P.G. & Research Department of Chemistry, RKM Vivekananda College (Autonomous), Mylapore, Chennai-600004, Tamil Nadu, India.

Corresponding author's email: askumarchem@yahoo.com (A. Senthil Kumar)

Abstract

Methylene blue (MB) is a versatile electrochemical redox system with applications in chemical sensors, electrocatalysis, biosensors, and electrochemical immunosensors. Developing stable, redox-active, chemically modified electrodes remains a challenging research task. In this study, we demonstrate the highly efficient immobilization and redox functionality of MB on a biomass-derived carbon quantum dot (CQD)/cation-exchanging per-fluoropolymer, Nafion®-composite modified glassy carbon electrode, referred to as GCE/Nf-CQD@MB, for electrochemical application. The CQDs were synthesized using an eco-friendly, one-step ultrasonication method with the *Vasambu* herbal plant (*Acorus calamus*). The CQDs were characterized through various physicochemical techniques, revealing that they

occupy the ~5 nm hydrophilic channels of the Nafion membrane via cooperative interactions involving π-π stacking and ionic bonding. Control electrochemical experiments using CQDs and Nafion for MB adsorption showed weak or negligible redox responses. However, the chemically modified electrode, GCE/Nf-CQD@MB, exhibited an excellent surface-confined redox peak at a standard electrode potential ($E^\circ = 0.3$ V vs. Ag/AgCl) in a pH 7 phosphate buffer solution. As a proof of concept, we explored the voltammetric pH sensing capabilities of this electrode.

Keywords: Methylene blue; Nafion; Biomass-carbon quantum dots; Surface-confined redox-behavior; Synergic effect; pH sensor

1. Introduction

Methylene blue (MB) is a synthetic dye that has been widely used for centuries to color cotton, silk, and wool textiles [1,2]. The excessive discharge of MB from industries into aquatic environments poses a significant environmental threat [3]. Chronic exposure to MB and its derivatives in humans has been linked to mutagenic [4], allergenic [5], and carcinogenic effects [6]. Despite its environmental concerns, MB also has a long history of clinical applications (at low dosages), particularly in medicine and microbiology [7]. Its unique properties make it a valuable tool for various diagnostic and therapeutic procedures. Some examples include: (i) Malaria diagnosis: MB is used to stain blood smears, allowing for the identification of malaria parasites. The dye binds to the DNA and RNA of these parasites, making them visible under a microscope [8], (ii) Methemoglobinemia treatment: MB can reduce methaemoglobin, an abnormal form of haemoglobin that cannot carry oxygen, back to normal haemoglobin. This is essential for treating methemoglobinemia, a condition characterized by a significant amount of oxidized haemoglobin [9], (iii) Antiseptic and disinfectant: MB has been used to treat minor skin infections, wounds, and urinary tract infections (UTIs) [10], (iv) Neurological disorders:

Studies have explored the potential of MB in treating Parkinson's disease [11], although further research is needed. It has been suggested that MB might improve mitochondrial function and reduce oxidative stress [12], (iv) Algal bloom control: MB has been used to inhibit the growth of certain algae species in water bodies [13] and (v) Food industry: MB is sometimes used as a food coloring agent and preservative [14]. In addition to its biomedical applications, MB's excellent proton-coupled electron-transfer activity makes it a valuable mediator for oxidation and reduction reactions [15–17]. It has also been used as an enzyme cofactor in bioelectrocatalytic [18–20] and bioelectrochemical immunosensors [21,22] and pH sensor [23–26]. Developing effective MB adsorption systems for real-time applications is a challenging research task. This study presents a vasambu-herbal plant (Acorus calamus)-derived biomass carbon quantum dots (CQD) material/perfluoro cation exchanging polymeric membrane (Nafion) chemically modified electrode (Nf-CQD@MB) as an efficient adsorbent for MB. Its electron-transfer characteristics were evaluated using cyclic voltammetry (CV), and sensitive voltammetric pH sensor was demonstrated as a model system for real-time applications.

For the adsorption of methylene blue (MB), various adsorbents have been reported in the literature, including silica [27], clay [28], zeolite [29], carbon nanomaterials (such as carbon nanotubes [30,31] graphite [32], graphene [33], graphene oxide [21,34]), and biomass-derived carbons [13,35,36]. While these materials are effective for bulk adsorption applications, extending their use to electrochemical applications can be challenging due to electrode fouling [37]. Electrode fouling is a significant issue in MB-based chemically modified electrodes. For example, MB adsorbed on unmodified glassy carbon electrodes (GCE/MB$_{ads}$) and oxygen-functionalized single-walled carbon nanotubes (GCE/Nf-CQD@MB$_{ads}$) exhibited approximately 30% fouling after only twenty continuous cycles in cyclic voltammetry experiments at a scan rate of 100 mV/s [38,39]. To stabilize MB on electrodes, it is advisable

to use pristine graphitic structures with a high concentration of basal planes rather than edge planes. In this regard, reduced graphene layers linked to MB have been reported for preparing stable MB-chemically modified electrodes [34,39]. Ionic interactions between MB and cation-exchanging perfluoro polymer membranes, such as Nafion, have also been explored [39,40]. Interestingly, in this work, a low-cost and environmentally friendly biomass carbon quantum dots/Nafion composite modified glassy carbon electrode, designated as GCE/Nf-CQD, have demonstrated excellent adsorption and stable electrochemical responses for MB in pH 7 phosphate buffer solutions (GCE/Nf-CQD@MB). The synergistic mechanism for enhanced MB adsorption in these systems involves both π-π interactions on the graphitic surface and cation-exchange interactions with the sulfonic sites of Nafion. As a model system, this work demonstrated the application of voltammetric pH sensing.

A person's physiological, biochemical, and medicinal conditions can be significantly impacted by their pH level. For instance, the presence of bacterial colonies and enzymes causes the pH at chronic wound sites to shift from slightly acidic (pH 5.5) for healthy skin to basic (pH 7.0–8.5) for damaged skin [41]. Similarly, in food preparation, the pH level indicates the germination or inactivation of bacterial spores, protein denaturation, gelification, and the development and death of microorganisms. Potentiometric pH probes like glass electrodes are still the gold standard, but their precision is limited since it can be challenging to discriminate between intended pH changes and probable drifts or errors (up to 0.02 pH units every day). Numerous electrochemical pH sensors based on voltammetric, amperometric, and potentiometric methods have been published in this regard [42,43]. Among these, a potentiometric pH sensor with a bulb-tip glass electrode diameter of 1–12 mm has been utilized a lot because of its commercial availability, quick response time, sensitivity, and selectivity. Indeed, its suitability for some applications is limited by issues with its delicate nature, alkaline

mistakes, instability, and probable drift [44,45]. As an alternative, pH-sensitive redox probes have been reported, such as quinone functionalized graphitic edge-planes based voltammetric pH-sensing method, hydroquinone (HQ) [46,47]] and anthraquinone (AQ) [48,49]phenanthroline-quinone [50] and methylene blue dye [23-26] etc. In this connection design and development of simple, sensitive and stable redox-active molecular species immobilized electrode is a challenging task. In this work, a GCE/Nf-CQD@MB showed highly selective pH sensing in the real samples. As a proof of concept, selective Voltammetric pH sensing was demonstrated with seven different real samples.

2. Experimental section

2.1. Reagents and materials

5% Nafion and methylene blue were purchased from Sigma-Aldrich (USA). All other chemicals used in this study were reagent-grade and ACS-certified. Standard stock solutions of Na_2HPO_4 and NaH_2PO_4 were combined and adjusted to pH values ranging from 2 to 12 using 0.1 M of H_3PO_4 and NaOH. All solutions were deoxygenated with N_2 gas for approximately 15 minutes prior to each electrochemical experiment.

2.2 Apparatus

The solution pH was measured using a DKK-TOA HM-41X pH meter (Japan). The meter was standardized with standard pH buffers of 4.0, 7.0, and 9.0. Cyclic voltammetry experiments were conducted using a CHI 440B Electrochemical Workstation (USA). A three-electrode system was employed, consisting of a glassy carbon electrode (GCE; 3mm diameter) as the working electrode, an Ag/AgCl (3 M KCl) reference electrode, and a Platinum (2mm diameter) counter electrode. The 10mL cell was purged with N_2 gas. The synthesized carbon quantum dots (CQDs) were characterized using various analytical techniques. Raman spectroscopy was performed using a Renishaw Invia instrument (Israel) with a 785 nm laser.

FT-IR analysis was carried out on a JASCO 4100 instrument (Japan). Transmission electron microscopy (TEM) images were acquired using the FEITECNAI-G2 20 Twin instrument. For TEM analysis, an aqueous suspension of CQDs and Nf-CQDs were dropped onto a Cu grid. UV/Vis spectroscopy was performed using a Jasco V-670 spectrometer (Japan), and XRD analysis was conducted using a Bruker D8 Advanced diffractometer (Germany).

2.3 Preparation of CQD

About 200 g of fresh vasambu (*Acorus calamus*) stem was bought from the local market, cut into nearly uniform pieces, cleaned with hot, double-distilled water to get rid of foreign material like soil, pathogens, and dried naturally in the sun for 10 to 15 days before being powdered using the graining technique (Figure 1A). About 4 g of the vasambu powder was dispersed in 100 ml of double-distilled water and ultrasonically treated (40 KHz) for 8 hours. A dark yellow-brown colloidal solution obtained was subjected to centrifuging for 30 minutes at 10,000 RPM to remove unreactive and heavy larger-scale particles, followed by filtering using a 0.22 μm cellulose membrane filter. The resultant clear yellow-brown aqueous solution (CQDs) was collected and evaluated for further characterization and electrochemical pH sensor.

2.4 Modification of GCE/Nf-CQD@MB

Initially, the GCE surface was mechanically cleaned using 1 μm alumina powder, followed by washing with ethanol and water, and then electrochemically by performing ten cycles of CV in pH 7 phosphate-buffered solution (PBS) within a potential range of -0.8 to 0.6 V versus Ag/AgCl at a scan rate of 0.05 V s^{-1}. GCE/Nf-CQD was prepared by drop-casting 5 μL of an Nf-CQD suspension onto a pretreated GCE surface and drying at room temperature for 5 ± 1 minutes. The Nf-CQD suspension was prepared by mixing equal volumes of 1% Nafion and prepared CQD solutions and sonicating for 1 hour. GCE/Nf-CQD@MB was

fabricated by performing 20 continuous cycles of CV in a 1 mM MB solution in pH 7 PBS within a potential range of -0.8 to 0.6 V versus Ag/AgCl at a scan rate of 0.05 V s⁻¹. After modification, the electrode was gently washed and placed in a plain pH 7 PBS solution. Subsequent CV analysis showed no change in peak current or peak potential, indicating the stability of the modified electrode, which was designated as GCE/Nf-CQD@MB as shown in Scheme 1.
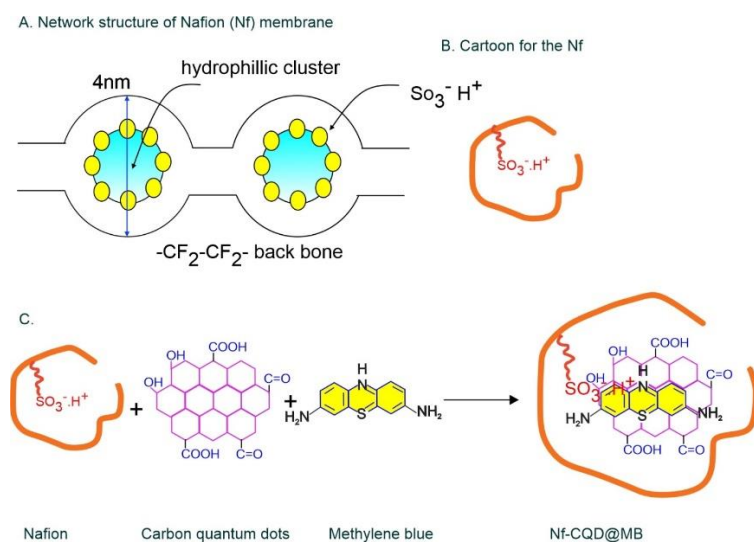
Scheme 1. (A) Illustration for the Nafion® network structure and (B) is cartoon. (C) Schematic reaction for the combination of Nafion (Nf), carbon quantum dots (CQD) and methylene blue (NB) as Nf-CQD@MB composite system.

2.5 Real sample analysis

The crude samples of 10 ml each of spinach juice (#1), tomato juice (#2), banana pulp (#3), baking soda (#4), and egg white (#5) were examined for pH analysis.

3. Results and discussion

3.1 Structural characterization of CQDs

The CQDs were subjected to UV-Vis spectroscopic analysis. As depicted in Figure 1B, the sample exhibited two characteristic absorption peaks at λ_{max} = 240 nm and 290 nm,

indicative of the aromatic ring structure transition of π-π* and the C=O electronic transition of n-π*, respectively. In contrast, the control-vasambu powder failed to show defined absorption bands, as shown in Figure 1B, curve b. This preliminary observation suggests the formation of a sp^2 carbon-rich graphitic nanomaterial [16]. The functional groups of CQDs were investigated using FT-IR spectroscopy, which revealed a series of IR peaks corresponding to various functional groups, including -OH and -NH (3600-3100 cm^{-1}), -CN (2100 cm^{-1}), -C=O (1630 cm^{-1}), COO- (1520 and 1450 cm^{-1}), C-O-C (1210 & 1150 cm^{-1}), C-N, C-S, C-O (930 cm^{-1}), and =CH (700-600 cm^{-1}) (Figure 1C) [51,52]. Raman spectroscopy of CQDs was employed to elucidate their graphitic nature, amorphous character, distortion, and defects (Figure 1D). CQDs displayed two prominent peaks at approximately 1330 cm^{-1} and 1585 cm^{-1}, characteristic of the disorder (D) band and crystalline (G) bands of carbonaceous structures, respectively. This suggests that the prepared CQDs possess both sp^3 and sp^2 carbon units, albeit in varying proportions. A relatively higher graphitic-defect density was observed in CQDs, as evidenced by the intensity ratio of the D and G bands (I_D/I_G) of 1.87 [52,53]. These findings indicate that CQDs possess a unique graphitic structure with C–O functional groups. XRD analysis was conducted to further assess the graphitic structure and amorphous nature of CQDs. The XRD pattern of CQDs exhibited a broad peak at 20.89° and a relatively sharp peak at 40.5°, corresponding to the (002) and (101) planes of reduced graphene oxide, respectively. The XRD diffractogram results suggest that CQDs consist of polyaromatic C domains containing heteroatoms such as oxygen, nitrogen, and sulfur, surrounded by an amorphous carbon network with varying degrees of graphitization (Figure 1F) [51,52]. TEM analysis was performed on CQDs to corroborate the presence of the graphitic structure, amorphous nature, and particle size. The TEM image presented in Figure 2A illustrates the uniform dispersion of CQDs, which typically have sizes ranging from 2 to 10 nm. These particles exhibit a quasi-spherical shape and do not aggregate. To further understand the distribution details of CQD in

the Nafion membrane, an equal ratio of synthesized CQD and 1% Nafion membrane was mixed

and sonicated for 30 minutes, and the composite films were subjected to TEM analysis. Figures

2B-C depict the TEM images of Nf-CQD in the range
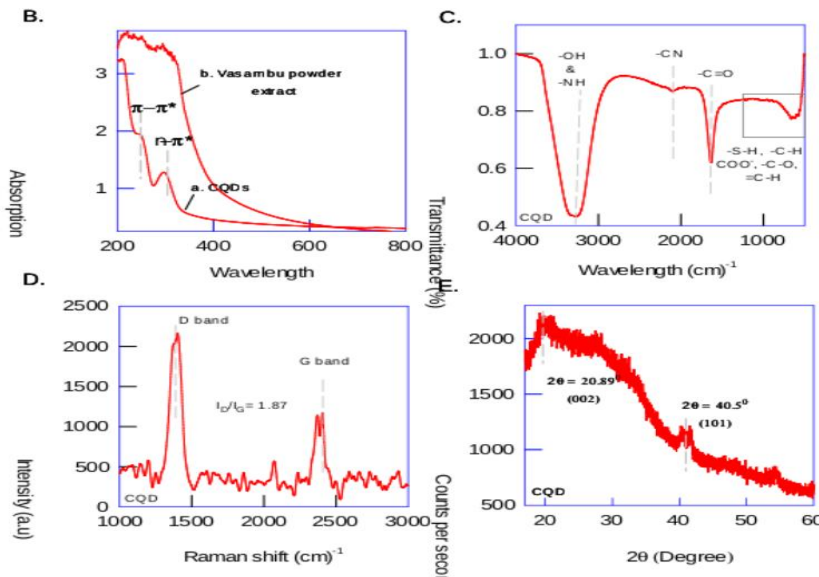
Figure 1. (A) Schematic illustration for the Synthesis of Biomass-CQD from vasambu powder by one-step ultrasonication method. (B) UV-Vis, (C) FT-IR, (D) Raman and (E) XRD response of prepared CQD.

of 5 to 10 nm, where some agglomerated CQD particles in the Nafion membrane can be clearly

seen. The enlarged view (Figure 2C) shows a uniform dispersion of tiny dot-like structures and

well-adsorbed CQD particles in the Nafion membrane, resembling a filler-like molecular

arrangement in the Nafion membrane composite system. There is partial

interaction/immobilization of CQD monolayers on the surface of the Nafion membrane in the

composite system [54]. It is noteworthy that the Nafion membrane has three different channels:

a highly hydrophobic network composed of -CF_2-CF_2- linkages, hydrophilic sulfonic acid

chains, and sulfonic acid groups forming channels with protonated water, approximately 5 nm

in size [55][56]. Based on the TEM results, it is clear that the CQD was trapped in the

hydrophilic channels. The selected area electron diffraction (SAED) pattern of CQDs,

confirmed the amorphous nature of the material (Supporting Information Figure S1). Additionally, the CQDs particles displayed distinct fringes with an interplanar distance of 0.22 nm, corresponding to the surface's (100) graphite plane and the elemental analysis of prepared CQDs were confirmed by EDAX, and it shows the presence of carbon (29.4%), Nitrogen (8.1%), Oxygen (61.5%) and Sulphur (0.8%) as shown in supplementary Figure 1S (A-C) [54].
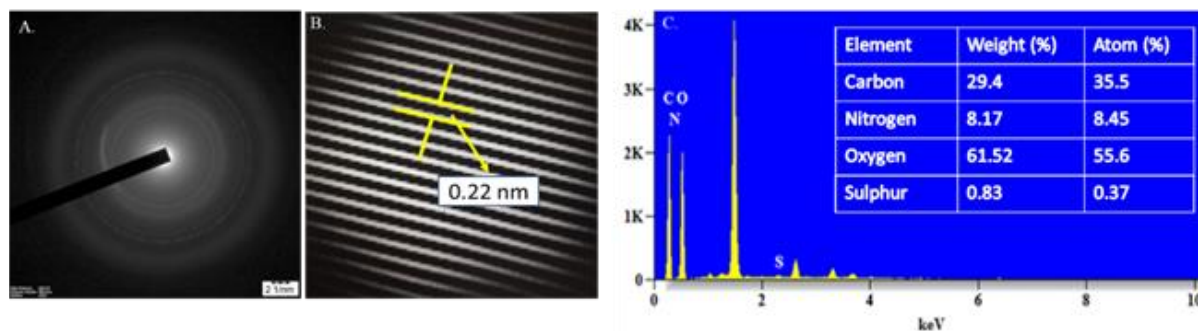
Figure S1. (A) SEAD pattern (B) Fringes and (C) EDAX of the CQDs.
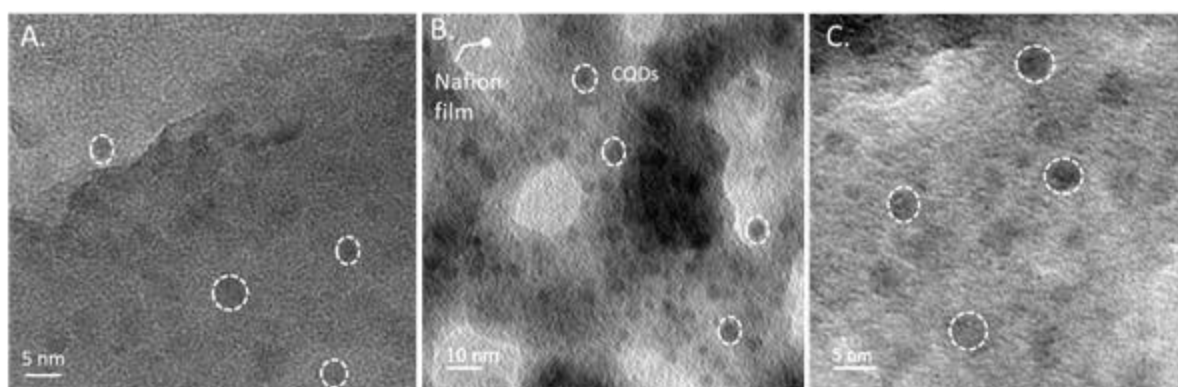
Figure 2. TEM images of (A) CQD, (B and C) Nf-CQD.

3.2 Electrochemical properties of GCE/Nf-CQD@MB

Initial experiments were carried out using a GCE/MB in a pH 7 PBS solution. As shown in Figure 3A, Curve a, a featureless voltage-voltammetric response in a potential window test, -0.8 to 0.6 V vs Ag/AgCl was observed. This observation indicated that the MB is not electrically connected with the GCE surface. Further, when GCE/MB was replaced by

GCE/Nf@MB (Figure 3A; curve b), a feeble redox peak at the apparent standard electrode potential, $E^{o'}$ (E_{pa} + E_{pc}/2) =0.31V vs Ag/AgCl was noticed. These results show the cationic exchange sites of Nafion are small enough to make a loading of MB and for the electrochemical behavior. Interestingly, when the modified GCE/Nf-MB was coupled with the CQD, the GCE/Nf-CQD@MB, a well-defined and quasi-reversible redox peak was observed (figure 3A; curve c). Following the experiment, when the modified electrode was washed with water and replaced in pH 7 PBS, redox-peak was retained without any surface fouling issues. The calculated surface excess of the modified electrode is about 10 times higher than the surface excess calculated with GCE/MB and GCE/Nf@MB cases. The relative standard deviation (RSD) between the redox peak current signals of the first and twentieth CV cycles was 2.1%. This observation denotes the appreciable stability of the MB-chemically modified electrode. It is conceivable that the π−π interaction between the conjugated π-electrons of the aromatic molecules and the sp^2 sites of carbon quantum dots, along with the ionic interaction between the positively charged MB and the negatively charged sulfonic acid groups of Nafion, cooperatively contributes to the enhanced loading and stabilization of MB on the Nf-CQD matrix in this work.

The effect of Nafion loading was studied to optimize the redox behavior of GCE/Nf-CQD@MB. As shown in Figures 3B-C, various concentrations of Nafion, such as 0.1%, 0.5%, 1%, 2%, and 5%, were prepared by dilution with ethanol. Among all, 1% Nafion demonstrated a well-defined and higher current redox peak response, which was more favorable compared to other concentrations. It is plausible that 1% Nafion-CQD provides the best loading to achieve the cooperative effect of MB immobilization. Lower or higher concentrations of Nafion may

result in either CQD or Nafion dominating, leading to poor MB adsorption and stabilization.
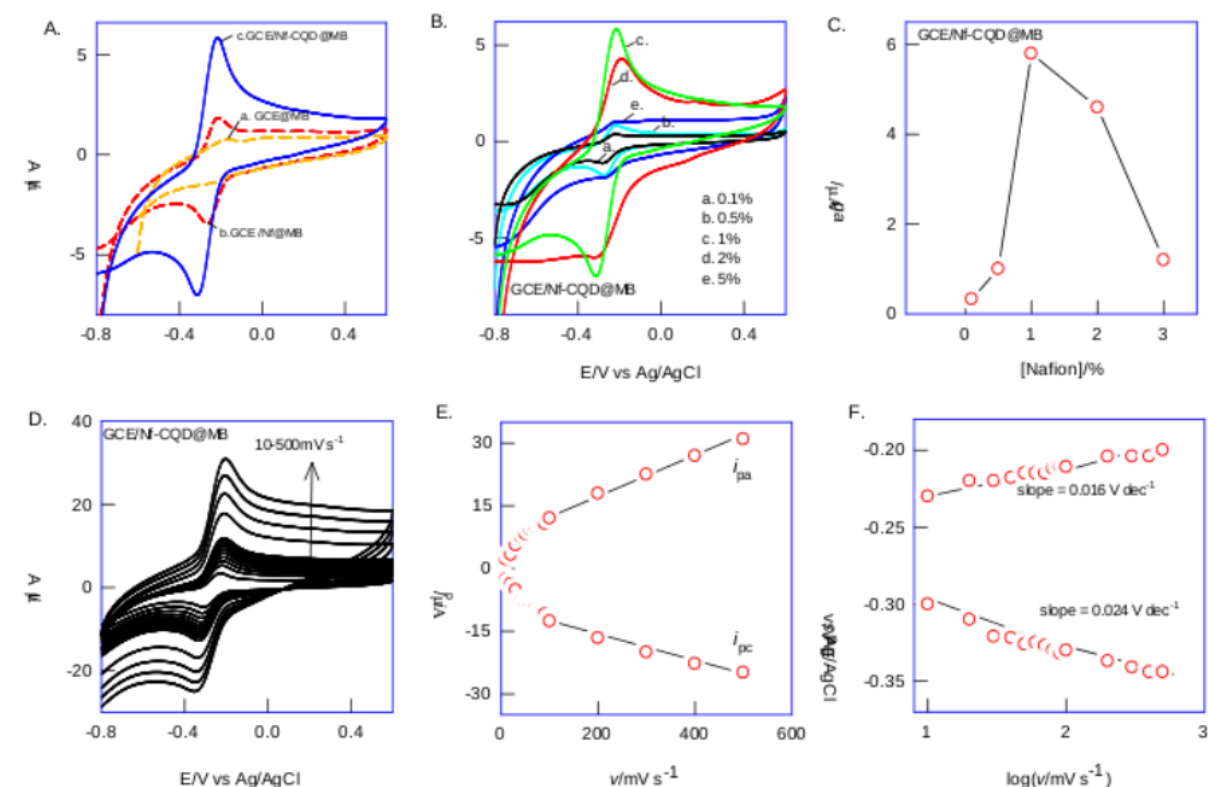
Figure 3. (A) CV response of (a)GCE@MB (b) GCE/Nf@MB and (c) GCE/Nf-CQD@MB in pH 7 PBS at 10 mV s⁻¹ (B) GCE/Nf-CQD@MB at various concentrations of Nafion (0.1, 0.5, 1, 2, and 3%) in pH 7 PBS at 10 mV s⁻¹ (C) The calibration plot of Nafion concentration vs i_{pa} **(D)** Effect of scan rate of GCE/Nf-CQD@MB in a blank pH 7 PBS. Plot of (D) i_p vs v *(F) E_p vs log(v/mV s⁻¹).*

To comprehend the electron-transfer characteristic, GCE/Nf-CQD@MB was exposed to a CV scan rate effect in pH 7 PBS. A consistent rise in the anodic (i_{pa}) and cathodic (i_{pc}) peak currents against the scan rate was observed, as can be shown in Figure 3D. The adsorption-controlled electron-transfer characteristic of the redox system is indicated by a linear line plotting the values of i_{pa} and i_{pc} against the scan rate of the redox peaks, which start at the origin (Figure 3E). The electron-transfer coefficient (α) and heterogeneous electron-transfer rate constant (k_s) were computed using the following equations in the context of the Laviron model method ($\Delta Ep > 200/n$) [57]:

$$SL_a/SL_c = \alpha/1-\alpha \qquad\qquad\qquad -(1)$$

$$\log(k_s) = \alpha\log(1-\alpha) + (1-\alpha)\log\alpha - \log[(RT/\{nF(v)\})] - \alpha(1-\alpha)nF\Delta E_p/2.3RT \qquad -(2)$$

where SL_a and SL_c are the anodic and cathodic slopes of a linear plot, respectively, E_{pa} vs $\log v$, v is a scan rate (80 mV s^{-1}); $n\Delta E_p$ is a peak-to-peak separation of the redox peak (200 mV); n is the number of electrons per stoichiometric redox step; F is the Faraday (96,500C/mol) constant, and other symbols have its significance. Figure 3F shows the plot of E_{pa} and E_{pc} vs $\log v$ for the GCE/Nf-CQD@MB showing SL_a and SL_b values, 160 and 240 mVdec^{-1}, respectively. Based on equation-(1), the calculated α value is 0.42. Applying the value in equation (2), the corresponding k_s value is calculated as 0.402 s^{-1}.

3.3 Voltammetric pH sensor of GCE/Nf-CQD@MB

The GCE/Nf-CQD@MB was subjected to voltammetric pH sensing applications. The DPV response was recorded under optimized conditions: pulse width, pulse period, and step potential were set to 0.06 mV, 0.5 s, and 4 mV, respectively. Using 0.1M H_3PO_4 and NaOH, various pH solutions ranging from 2 to 12 were prepared for the DPV studies of the GCE/Nf-CQD@MB electrode. As shown in Figure 4A, a regular shift in DPV peak potential with pH was observed. In Figure 4B, the peak potential (E_p) of DPV is plotted against pH. The slope of this graph was -58±2 mV/pH, which is close to the ideal Nernstian value of -60 mV/pH for a pH-responsive electrode. This suggests that an equal number of protons and electrons were involved in the redox process, as indicated by the Nernstian-type relationship shown in the figures. Notably, the slope of -58±1 mV/pH indicates that this device holds promise as a biocompatible and eco-friendly voltammetric pH sensor. The modified electrode was found to be stable for 4 weeks at room temperature (25°C), with a change in peak current value of 4.2%.
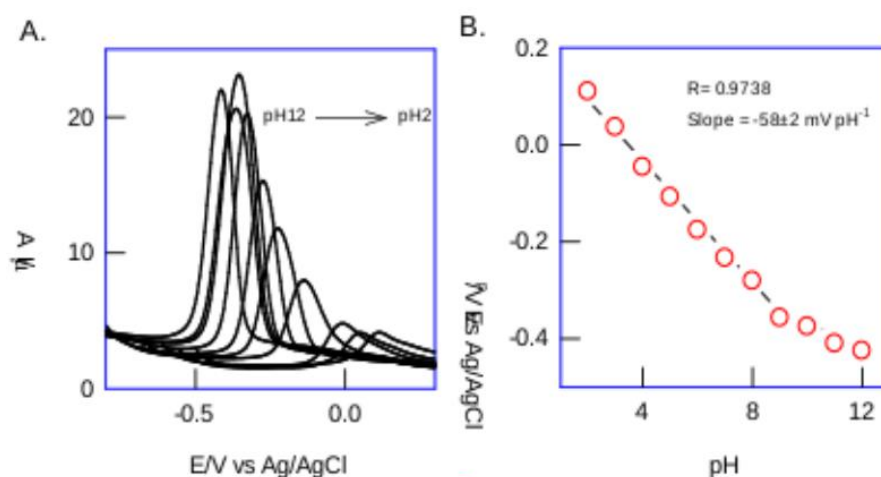
Figure 4. (A) DPV responses of GCE/Nf-CQD@MB under different solution pHs (2-12) and (B) Plot of E_p vs pH obtained from DPV data. *conditions:* Pulse width- 0.06 s; Pulse height- 0.05 V; potential step- 0.04 V.

3.4 Real sample analysis

As a proof of concept for voltammetric pH sensing, the GCE/Nf-CQD@MB electrode was subjected to real sample pH analysis of several food samples (10 mL), including spinach juice (#1), tomato juice (#2), banana pulp (#3), baking soda (#4), and egg white (#5) (Figure 5A-E). In a parallel experiment, the conventional pH measurement method was used to measure the pH of the solutions. The real sample analysis data is displayed in Table 1, along with error values from this test, which used a standard pH sensor setup. It is interesting to note that the results from our modified GCE/Nf-CQD@MB electrode pH sensor method show less than 2.5% error when compared with the traditional glass electrode method. These results demonstrate an excellent opportunity for the rapid development of a voltammetric pH sensor system utilizing low-cost biomass carbon quantum dots and methylene blue (MB), supported by a dilute Nafion membrane.

Figure 5. DPV responses of GCE/Nf-CQD@MB with various real samples (A-E) examined for pH measurements. #1-spinach juice, #2-tomato juice, #3-banana pulp, #4-baking soda, #5-egg white.

Table 1. Voltammetric pH analysis of various real samples using GCE/Nf-CQD@MB and conventional pH meter.
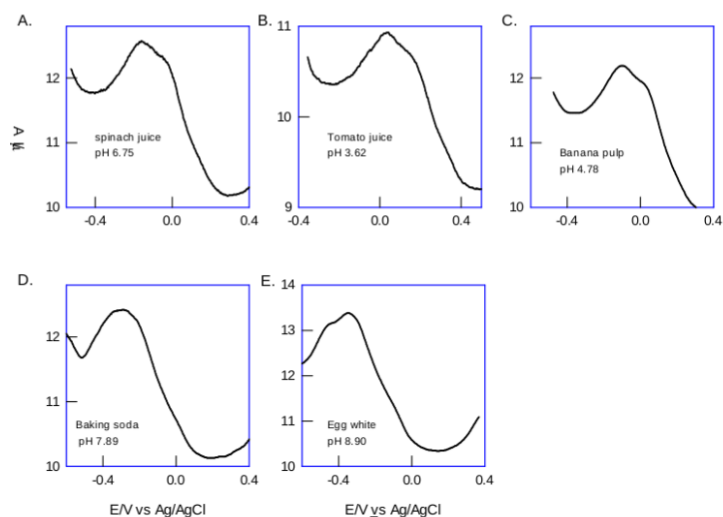
Samples	Conventional pH meter	GCE/Nf-CQD@MB	Error (%)
1. Egg white	9.01	8.90	1.2
2. Baking soda	8.03	7.89	1.7
3. Spinach juice	6.81	6.75	1.0
4. Banana pulp	4.69	4.78	1.9
5. Tomato juice	3.71	3.6	2.5

4. Conclusion

A biomass-based carbon quantum dots (CQDs) material was prepared using an Indian herbal plant, Vasambu powder, through a one-step ultrasonication process in an aqueous solution. The synthesized CQDs were characterized physicochemically using TEM, XRD, UV-VIS, Raman, and FTIR spectroscopy. A novel chemically modified electrode, combining a cationic exchange perfluoro polymer, Nafion, and CQDs, was developed as an efficient platform for enhanced immobilization of Methylene Blue (MB) on the electrode surface (Nf-CQD@MB). Under optimal conditions, the GCE/Nf-CQD@MB exhibited a persistent and well-defined redox peak at an apparent electrode potential ($E^{o'}$) of 0.31 V against Ag/AgCl. Control CV experiments using MB-loaded GCE and GCE/Nf showed either no or poor redox response. Mechanistic insights from scan rate studies revealed that the redox peak is regulated

31

by adsorption and follows proton-coupled electron transfer kinetics. Additionally, HRTEM analysis of the Nf-CQD composite showed that the CQD particulates were embedded in the 5 nm hydrophilic channels of the Nafion membrane via π-π and ionic interactions. Pulse voltammetry was employed to study the dynamics of the redox peak's proton-coupled electron transfer against solution pH. A plot of peak potential versus solution pH showed a slope value of -58 ± 2 mV/pH, confirming a Nernstian response involving equal numbers of protons and electrons in the electrochemical reaction. In practical applications, this method demonstrated accurate and precise voltammetric pH sensing in samples such as egg white, tomato juice, banana pulp, spinach juice, and baking soda, yielding results comparable to those obtained using a traditional pH meter. This study introduces a unique surface-confined, chemically modified electrode approach for voltammetric pH sensors, effectively assessing the electron-transfer functionality of Methylene Blue.

Declaration of Competing Interest

We wish to confirm that there are no known conflicts of interest associated with this publication and there has been no significant.

CRediT authorship contribution statement

Jayaprakash Meena: Investigation, Formal analysis, Resources, Formal analysis, Methodology, Validation, Data curation, Writing-original draft, Visualization; **Z. Waseem Basha**: Investigation, Formal analysis, Resources, Methodology, Validation, Resources, preparation of CQD; **S. Muniraj**: Conceptualization, Visualization, Supervision; **K.Santhakumar**: Conceptualization, Visualization, Supervision; **Annamalai Senthil Kumar:** Conceptualization, Methodology, Writing - original draft, Writing - review & editing, Visualization, Supervision, Project administration, Funding acquisition.

Supporting Information

SEAD, TEM fringers, and EDAX of prepared CQDs.

References

[1]   P.O. Oladoye, T.O. Ajiboye, E.O. Omotola, O.J. Oyewola, Methylene blue dye: Toxicity and potential elimination technology from wastewater, Results Eng. 16 (2022). https://doi.org/10.1016/j.rineng.2022.100678.

[2]   R. Al-Tohamy, S.S. Ali, F. Li, K.M. Okasha, Y.A.G. Mahmoud, T. Elsamahy, H. Jiao, Y. Fu, J. Sun, A critical review on the treatment of dye-containing wastewater: Ecotoxicological and health concerns of textile dyes and possible remediation approaches for environmental safety, Ecotoxicol Environ Saf 231 (2022). https://doi.org/10.1016/j.ecoenv.2021.113160.

[3]   S. Dutta, S. Adhikary, S. Bhattacharya, D. Roy, S. Chatterjee, A. Chakraborty, D. Banerjee, A. Ganguly, S. Nanda, P. Rajak, Contamination of textile dyes in aquatic environment: Adverse impacts on aquatic ecosystem and human health, and its management using bioremediation, J Environ Manage 353 (2024) 120103. https://doi.org/https://doi.org/10.1016/j.jenvman.2024.120103.

[4]   T. J. McBride , J.E. Schneider, R.A. Flyod, L.A. Loed, Mutations induced by methylene blue plus light in single-stranded M13mp2, Proc. Natl. Acad. Sci. 89 (1992) 6866-6870.

[5]   M. Akazawa, Y.-H. Wu, W.-M. Liu, Allergy-like reactions to methylene blue following laparoscopic chromopertubation: A systematic review of the literature, Eur J Obstet Gynecol Reprod Biol. 238 (2019) 58–62. https://doi.org/https://doi.org/10.1016/j.ejogrb.2019.03.019.

[6]   M. Copisarow, Is Methylene-Blue Anti-Carcinogenic?, Science 78 (1933) 212. https://doi.org/10.1126/science.78.2019.212.a.

[7]   P.R. Ginimuge, S.D. Jyothi, Methylene Blue: Revisited, J Anaesthesiol Clin Pharmacol 26 (2010) 517-520.

[8]   G. Lu, M. Nagbanshi, N. Goldau, M. Mendes Jorge, P. Meissner, A. Jahn, F.P. Mockenhaupt, O. Müller, Efficacy and safety of methylene blue in the treatment of malaria: A systematic review, BMC Med 16 (2018). https://doi.org/10.1186/s12916-018-1045-3.

[9]   A.J. Matisoff, M.K. Panni, Methylene Blue Treatment for Methemoglobinemia and Subsequent Dramatic Bispectral Index Reduction, Anesthesiology 105 (2006) 228. https://doi.org/10.1097/00000542-200607000-00043.

[10]   X. Shen, L. Dong, X. He, C. Zhao, W. Zhang, X. Li, Y. Lu, Treatment of infected wounds with methylene blue photodynamic therapy: An effective and safe treatment method,

Photodiagnosis Photodyn Ther 32 (2020) 102051. https://doi.org/https://doi.org/10.1016/j.pdpdt.2020.102051.

[11] E.S. Smith, M.E. Clark, G.A. Hardy, D.J. Kraan, E. Biondo, F. Gonzalez-Lima, L.K. Cormack, M. Monfils, H.J. Lee, Daily consumption of methylene blue reduces attentional deficits and dopamine reduction in a 6-OHDA model of Parkinson's disease, Neuroscience 359 (2017) 8–16. https://doi.org/https://doi.org/10.1016/j.neuroscience.2017.07.001.

[12] Z. Mei Xiong, M. O'Donovan, L. Sun, J. Young Choi, M. Ren, K. Cao, Anti-Aging Potentials of Methylene Blue for Human Skin Longevity, Sci Rep 7 (2017). https://doi.org/10.1038/s41598-017-02419-3.

[13] R. Maurya, T. Ghosh, C. Paliwal, A. Shrivastav, K. Chokshi, I. Pancha, A. Ghosh, S. Mishra, Biosorption of methylene blue by de-oiled algal biomass: Equilibrium, kinetics and artificial neural network modelling, PLoS One 9 (2014). https://doi.org/10.1371/journal.pone.0109545.

[14] A.H. Mijinyawa, G. Durga, A. Mishra, A sustainable process for adsorptive removal of methylene blue onto a food grade mucilage: kinetics, thermodynamics, and equilibrium evaluation, Int J Phytoremediation 21 (2019) 1122–1129. https://doi.org/10.1080/15226514.2019.1606785.

[15] L.E. Korshoj, A.J. Zaitouna, R.Y. Lai, Methylene blue-mediated electrocatalytic detection of hexavalent chromium, Anal Chem 87 (2015) 2560–2564. https://doi.org/10.1021/acs.analchem.5b00197.

[16] A.A. Ensafi, Determination of Ascorbic Acid by Electrocatalytic Voltammetry with Methylene Blue, Anal Lett 36 (2003) 591–604. https://doi.org/10.1081/AL-120018250.

[17] J. Ma, H. Wu, Y. Zhu, Electrochemical behavior of hydrogen peroxide sensor based on new methylene blue as mediator, Frontiers of Chemistry in China 2 (2007) 326–330. https://doi.org/10.1007/s11458-007-0061-1.

[18] M. Puiu, O.M. Istrate, V. Mirceski, C. Bala, Ultrasensitive Detection of Hydrogen Peroxide Using Methylene Blue Grafted on Molecular Wires as Nanozyme with Catalase-like Activity, Anal Chem 95 (2023) 16185–16193. https://doi.org/10.1021/acs.analchem.3c02919.

[19] M. Christwardana, D. Frattini, G. Accardo, S.P. Yoon, Y. Kwon, Effects of methylene blue and methyl red mediators on performance of yeast based microbial fuel cells adopting polyethylenimine coated carbon felt as anode, J Power Sources 396 (2018) 1–11. https://doi.org/https://doi.org/10.1016/j.jpowsour.2018.06.005.

[20] S. Bu, K. Wang, Z. Li, C. Wang, Z. Hao, W. Liu, J. Wan, An electrochemical biosensor based on methylene blue-loaded nanocomposites as signal-amplifying tags to detect pathogenic bacteria, Analyst 145 (2020) 4328–4334. https://doi.org/10.1039/d0an00470g.

[21] A. Natarajan, K.S.S. Devi, S. Raja, A. Senthil Kumar, An Elegant Analysis of White Spot Syndrome Virus Using a Graphene Oxide/Methylene Blue based Electrochemical Immunosensor Platform, Sci Rep 7 (2017). https://doi.org/10.1038/srep46169.

[22] G. Dutta, S. Nagarajan, L.J. Lapidus, P.B. Lillehoj, Enzyme-free electrochemical immunosensor based on methylene blue and the electro-oxidation of hydrazine on Pt nanoparticles, Biosens Bioelectron 92 (2017) 372–377. https://doi.org/https://doi.org/10.1016/j.bios.2016.10.094.

[23] D.S. Raimundo, G.S. Cechelero, A. Acosta, F.R. Fernandez, W.J. Salcedo, Macroporous Silicon Structure Functionalized by Methylene Blue to pH Measurements Application, ECS Trans 9 (2007) 579–586. https://doi.org/10.1149/1.2766932.

[24] B. J-C Deboux, E. Lewis, P.J. Scully, R. Edwards, A Novel Technique for Optical Fiber pH Sensing Based on Methylene Blue Adsorption, J Lightwave Tech 13 (1995) 1407-1414.

[25] E. González-Fernández, M. Staderini, J.R.K. Marland, M.E. Gray, A. Uçar, C. Dunare, E.O. Blair, P. Sullivan, A. Tsiamis, S.N. Greenhalgh, R. Gregson, R.E. Clutton, S. Smith, J.G. Terry, D.J. Argyle, A.J. Walton, A.R. Mount, M. Bradley, A.F. Murray, In vivo application of an implantable tri-anchored methylene blue-based electrochemical pH sensor, Biosens Bioelectron 197 (2022). https://doi.org/10.1016/j.bios.2021.113728.

[26] Young-Hee Jeon, Jae-Joong Kwon, Byoung-Ho Lee, Study on pH Sensor using Methylene Blue Adsorption and A Long-Period Optical Fiber Grating Pair, J optical Soc. Korea 10 (2006) 28-32..

[27] X. Guo, Z. Zhao, X. Gao, Y. Dong, H. Fu, X. Zhang, Study on the adsorption performance of modified high silica fly ash for methylene blue, RSC Adv 14 (2024) 21342–21354. https://doi.org/10.1039/d4ra04017a.

[28] F. Pishdadi-Aghdarreh, R. Norouzbeigi, E. Velayi, Simultaneous adsorption of methylene blue cationic dye and paraquat herbicide on activated lightweight expanded clay aggregate (LECA) as a sustainable and recyclable adsorbent, Appl Clay Sci 256 (2024) 107432. https://doi.org/https://doi.org/10.1016/j.clay.2024.107432.

[29] H. Hadda Aya, N. Djamel, A. Samira, M. Otero, M. Ali Khan, Optimizing methylene blue adsorption conditions on hydrothermally synthesized NaX zeolite through a full two-level factorial design, RSC Adv 14 (2024) 23816–23827. https://doi.org/10.1039/d4ra04483e.

[30] J. Fito, M. Abewaa, A. Mengistu, K. Angassa, A.D. Ambaye, W. Moyo, T. Nkambule, Adsorption of methylene blue from textile industrial wastewater using activated carbon developed from Rumex abyssinicus plant, Sci Rep 13 (2023). https://doi.org/10.1038/s41598-023-32341-w.

[31] Y. Huan, G. Wang, C. Li, G. Li, Acrylic acid grafted-multi-walled carbon nanotubes and their high-efficiency adsorption of methylene blue, J Mater Sci 55 (2020) 4656–4670. https://doi.org/10.1007/s10853-019-04167-3.

[32] C.Y. Mah, N.N. Azhar, V.L. Wong, Y.L. Chen, S.A.M. Yagoub, S. Sen Teo, S.F. Su, S.P. Yeap, Loose and Encased Graphite for Methylene Blue Adsorption: Process Optimization and Principal Component Analysis, Chem Eng Technol 47 (2024) 474–484. https://doi.org/10.1002/ceat.202300246.

[33] A. Nouri, W.L. Ang, E. Mahmoudi, S.F. Chua, A.W. Mohammad, A. Benamor, M.M. Ba-Abbad, C.P. Leo, Decoration of polylactic acid on graphene oxide for efficient adsorption of methylene blue and tetracycline, Chemosphere 322 (2023) 138219. https://doi.org/https://doi.org/10.1016/j.chemosphere.2023.138219.

[34] D. Zhang, X. Ouyang, L. Li, B. Dai, Y. Zhang, Real-time amperometric monitoring of cellular hydrogen peroxide based on electrodeposited reduced graphene oxide incorporating adsorption of electroactive methylene blue hybrid composites, Journal of Electroanalytical Chemistry 780 (2016) 60–67. https://doi.org/https://doi.org/10.1016/j.jelechem.2016.09.005.

[35] I.U. Bakara, M.D. Nurhafizah, N. Abdullah, O.O. Akinnawo, A. Ul-Hamid, Investigation of kinetics and thermodynamics of methylene blue dye adsorption using activated carbon derived from bamboo biomass, Inorg Chem Commun 166 (2024) 112609. https://doi.org/https://doi.org/10.1016/j.inoche.2024.112609.

[36] Z. Waseem Basha, S. Muniraj, A. Senthil Kumar, Neem biomass derived carbon quantum dots synthesized via one step ultrasonification method for ecofriendly methylene blue dye removal, Sci Rep 14 (2024). https://doi.org/10.1038/s41598-024-59483-9.

[37] S. Dutta, B. Gupta, S.K. Srivastava, A.K. Gupta, Recent advances on the removal of dyes from wastewater using various adsorbents: A critical review, Mater Adv 2 (2021) 4497–4531. https://doi.org/10.1039/d1ma00354b.

[38] Y. Yan, M. Zhang, K. Gong, L. Su, Z. Guo, L. Mao, Adsorption of methylene blue dye onto carbon nanotubes: A route to an electrochemically functional nanostructure and its layer-by-layer assembled nanocomposite, Chemistry of Materials 17 (2005) 3457–3463. https://doi.org/10.1021/cm0504182.

[39] Z. Lu, S. Dong, Preparation and Electrochemical Behaviour of a Methylene Blue-modified Electrode based on a Nafion Polymer Film, J. Chem. Soc., Faraday Trans. 84 (1988) 2979-2986.

[40] V. Ganesan, S. Abraham John, R. Ramaraj, Multielectrochromic properties of methylene blue and phenosafranine dyes incorporated into Nafion® film, J. Electroanal Chem 502 (2001) 167–173. https://doi.org/https://doi.org/10.1016/S0022-0728(01)00354-0.

[41] M.T. Ghoneim, A. Nguyen, N. Dereje, J. Huang, G.C. Moore, P.J. Murzynowski, C. Dagdeviren, Recent Progress in Electrochemical pH-Sensing Materials and Configurations for Biomedical Applications, Chem Rev 119 (2019) 5248–5297. https://doi.org/10.1021/acs.chemrev.8b00655.

[42] S. Sinha, T. Pal, A comprehensive review of FET-based pH sensors: materials, fabrication technologies, and modeling, Electrochemical Science Advances 2 (2022). https://doi.org/10.1002/elsa.202100147.

[43] P. Kraikaew, S. Jeanneret, Y. Soda, T. Cherubini, E. Bakker, Ultrasensitive Seawater pH Measurement by Capacitive Readout of Potentiometric Sensors, ACS Appl Mater Interfaces (2020). https://doi.org/10.1021/acssensors.0c00031.

[44] L. Manjakkal, D. Szwagierczak, R. Dahiya, Metal oxides based electrochemical pH sensors: Current progress and future perspectives, Prog Mater Sci 109 (2020). https://doi.org/10.1016/j.pmatsci.2019.100635.

[45] Y. Qin, H.J. Kwon, M.M.R. Howlader, M.J. Deen, Microfabricated electrochemical pH and free chlorine sensors for water quality monitoring: Recent advances and research challenges, RSC Adv 5 (2015) 69086–69109. https://doi.org/10.1039/c5ra11291e.

[46] M. Gandhi, D. Rajagopal, A. Senthil Kumar, In situ electro-organic synthesis of hydroquinone using anisole on MWCNT/Nafion modified electrode surface and its heterogeneous electrocatalytic reduction of toxic Cr(vi) species, RSC Adv 11 (2021) 4062–4076. https://doi.org/10.1039/d0ra10370e.

[47] S. Sundaram, S.K. Annamalai, Selective immobilization of hydroquinone on carbon nanotube modified electrode via phenol electro-oxidation method and its hydrazine electro-catalysis and

Escherichia coli antibacterial activity, Electrochim Acta 62 (2012) 207–217. https://doi.org/10.1016/j.electacta.2011.12.044.

[48] A.S. Kumar, P. Swetha, Simple adsorption of anthraquinone on carbon nanotube modified electrode and its efficient electrochemical behaviors, Colloids Surf A Physicochem Eng Asp 384 (2011) 597–604. https://doi.org/10.1016/j.colsurfa.2011.05.010.

[49] T. Rębiś, A. Sobczak, M. Wierzchowski, A. Frankiewicz, A. Teżyk, G. Milczarek, An approach for electrochemical functionalization of carbon nanotubes/1-amino-9,10-anthraquinone electrode with catechol derivatives for the development of NADH sensors, Electrochim Acta 260 (2018) 703–715. https://doi.org/10.1016/j.electacta.2017.12.022.

[50] P. Gayathri, A. Senthil Kumar, Electrochemical behavior of the 1,10-phenanthroline ligand on a multiwalled carbon nanotube surface and its relevant electrochemistry for selective recognition of copper ion and hydrogen peroxide sensing, Langmuir 30 (2014) 10513–10521. https://doi.org/10.1021/la502651w.

[51] B. Luo, H. Yang, B. Zhou, S.M. Ahmed, Y. Zhang, H. Liu, X. Liu, Y. He, S. Xia, Facile Synthesis of Luffa Sponge Activated Carbon Fiber Based Carbon Quantum Dots with Green Fluorescence and Their Application in Cr(VI) Determination, ACS Omega 5 (2020) 5540–5547. https://doi.org/10.1021/acsomega.0c00195.

[52] Y. Li, Y. Zhao, H. Cheng, Y. Hu, G. Shi, L. Dai, L. Qu, Nitrogen-doped graphene quantum dots with oxygen-rich functional groups, J Am Chem Soc 134 (2012) 15–18. https://doi.org/10.1021/ja206030c.

[53] R. Genc, M.O. Alas, E. Harputlu, S. Repp, N. Kremer, M. Castellano, S.G. Colak, K. Ocakoglu, E. Erdem, High-Capacitance Hybrid Supercapacitor Based on Multi-Colored Fluorescent Carbon-Dots, Sci Rep 7 (2017). https://doi.org/10.1038/s41598-017-11347-1.

[54] D. Arthisree, W. Madhuri, N. Saravanan, B. Dinesh, S. Saikrithika, A.S. Kumar, A ternary polymer nanocomposite film composed of green-synthesized graphene quantum dots, polyaniline, polyvinyl butyral and poly(3,4-ethylenedioxythiophene) polystyrene sulfonate for supercapacitor application, J Energy Storage 35 (2021). https://doi.org/10.1016/j.est.2021.102333.

[55] J.M. Zen, A.S. Kumar, A mimicking enzyme analogue for chemical sensors, Acc Chem Res 34 (2001) 772–780. https://doi.org/10.1021/ar000073n.

[56] A.S. Kumar, T. Tanase, M. Iida, In situ nanostructure formation of (μ-hydroxo)bis(μ-carboxylato) diruthenium units in nafion membrane and its utilization for selective reduction of nitrosonium ion in aqueous medium, Langmuir 23 (2007) 391–394. https://doi.org/10.1021/la0623578.

[57] E. Laviron, General expression of the linear potential sweep voltammogram in the case of diffusionless electrochemical systems. J. Electroanal. Chem. Interfacial Electrochem. 101 (1979) 19-28.

Article-3

Cobalt di-selenide sustained polymerized melamine paraformaldehyde resin: An effective electrocatalyst for alkaline water oxidation

Manisha Malviya[*], Rishabh Mishra and Vivek Chaubey

Department of Chemistry, Indian Institute of Technology, Varanasi-221005, India.

*Email: manisha.apc@iitbhu.ac.in

Abstract:

Metal selenides have demonstrated diverse outcomes in water splitting. Cobalt di-selenide is notable for its performance in the oxygen evolution reaction (OER). This study presents $CoSe_2$, pMF-R, and $CoSe_2$@pMF-R nanostructures where $CoSe_2$ was synthesized on pMF-R. The formation of cobalt-nitrogen bonds enhances charge transfer between the glassy carbon electrode and $CoSe_2$ active sites. The $CoSe_2$@pMF-R catalyst exhibits a low onset potential of 1.56 V and superior electrochemical activity of 10 $mAcm^{-2}$ at 1.608 V Vs. RHE. The unique compositional and structural features of the $CoSe_2$@pMF-R composite contribute to its exceptional electrochemical performance.

Graphical abstract:

CoSe₂@p-MF-R

1. Introduction:

Research on the oxygen evolution reaction (OER) has intensified due to its essential role in water electrolyzers and rechargeable metal-air batteries. Consequently, there is a pressing need for the rational design and thorough investigation of novel electrode materials to achieve improved electrocatalyst performance [1-5]. The OER and hydrogen evolution reaction (HER) represent the two half-reactions integral to the water splitting process. Noble metal oxides such as RuO_2 and IrO_2 are recognized as highly effective OER electrocatalysts, yet their scarcity and expense limit their broader application. Thus, it is imperative to explore affordable and readily available OER electrocatalysts while maintaining catalytic efficiency. Recently, cobalt-based oxides and chalcogenides have garnered significant attention for their low water oxidation overpotentials and remarkable stability [6].

The synergistic electrochemical coupling of various components has been shown to enhance electrocatalytic performance through the integration of selenides with secondary active species. Selenium vacancies on the $CoSe_2$ surface facilitate the peroxidation of Co

sites, promoting hydroxide ion adsorption and subsequent Co-OOH oxyhydroxide formation [7-9]. The incorporation of transition metal selenides with conductive carbon nanomaterials such as carbon nanotubes (CNTs) and graphene represent a promising strategy to enhance electroconductivity [10-14]. Modifying the spin density and charge of adjacent carbon atoms can significantly improve the electrochemical properties of carbon-based nanomaterials for electrocatalysis and energy storage [15, 16].

Graphene is recognized as a suitable functional material that provides essential support for electrocatalysts due to its high surface area, outstanding electroconductivity, and excellent mechanical strength. Recently, Zhou et al. introduced a polymeric carbon nitride (PCN) nanosheet-based electrocatalyst for water splitting, which efficiently catalyzes the reverse reaction while minimizing energy consumption due to the proximity of surface electrons and holes. These advantageous characteristics have redirected research focus toward polymeric nitrogen-enriched materials [17, 18, 19]. Previous studies have demonstrated the effectiveness of combining transition metal selenides with porous nanomaterials for OER, as the pores can endure high mechanical stress and facilitate short diffusion lengths during charge-discharge cycles [20-22].

2. **Experimental section:** Preparation of pMF-R via thermal modification at 200º C for 2 hrs then 400 for 2 hrs in an amount (1:3) of melamine and formaldehyde, and left inside the furnace until it adopted the room temperature, this temperature modification results as polymeric form of melamine formaldehyde resin [23] and shown in Scheme-1. For preparation of $CoSe_2$, 59.6 mg of $CoCl_2.6H_2O$, 119.2 mg of Se powder, and 60 mg CTAB were dissolved in 60 mL of distilled water under ultrasonic operation for 2 hours. Subsequently, 8 mL of $N_2H_4.2H_2O$ was dropped in the above solution and transferred to a Teflon-lined autoclave and kept at 140° C in an oven for 24 hrs. After filtering and washing

with distilled water, the product was dried at 50 $^{\circ}$C for 12 hours. Eventually, the product was further calcined in N_2 atmosphere at 400 $^{\circ}$C for 2 hours. As presented in scheme 2, the preparation of $CoSe_2$@pMF-R followed the similar procedure as $CoSe_2$, and only 60 mg of pMF-R added during the autoclave process at 140° for 24 hrs.

3. Characterizations:

The crystalline and amorphous nature of the synthesised samples were examined by powder X-ray diffraction (XRD) on a Rigaku Smart Lab 9 kW powder type with a wavelength of 1.514 A° . A Raman α-300, AFM SNOM spectrometer was used for recording Raman spectra. The X-ray photoelectron spectroscopy (XPS) characterization was conducted by a K-alpha (XPS) system. The morphologies and microstructures of samples were identified by field emission-scanning electron microscopy, (FE-SEM) with the Nova Nano-SEM 450 [FE-SEM] and HR-TEM with the Thermo Fisher Technai 20 G^2. BET surface area and pore size were analysed by Bellsorp Max II & Belcat-II. CHI (608C) instrument setup was used for electrochemical studies.
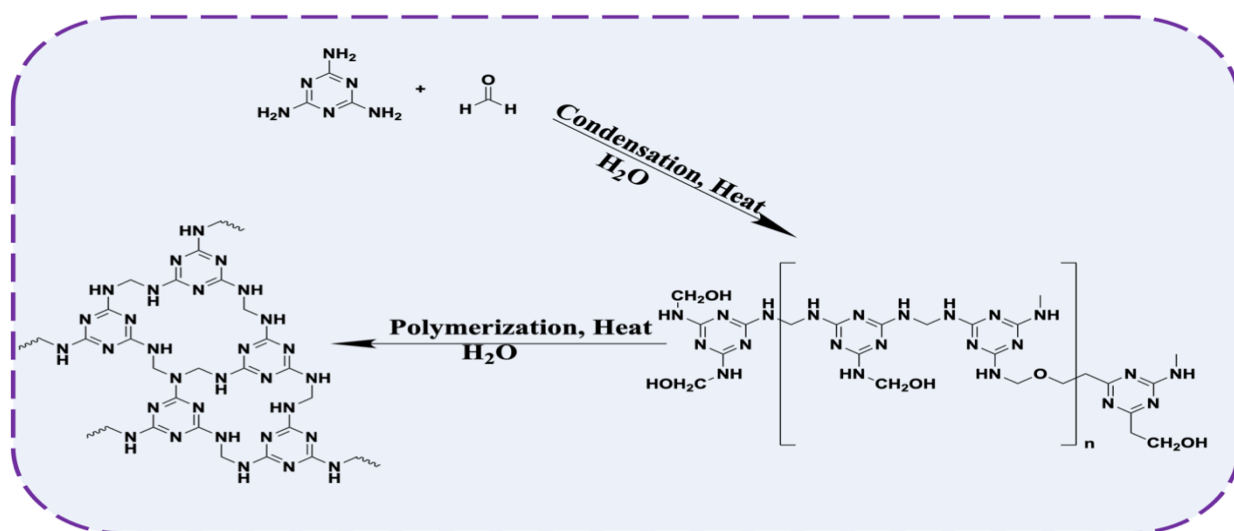
Scheme. 1. Reaction mechanism of pMF-R.
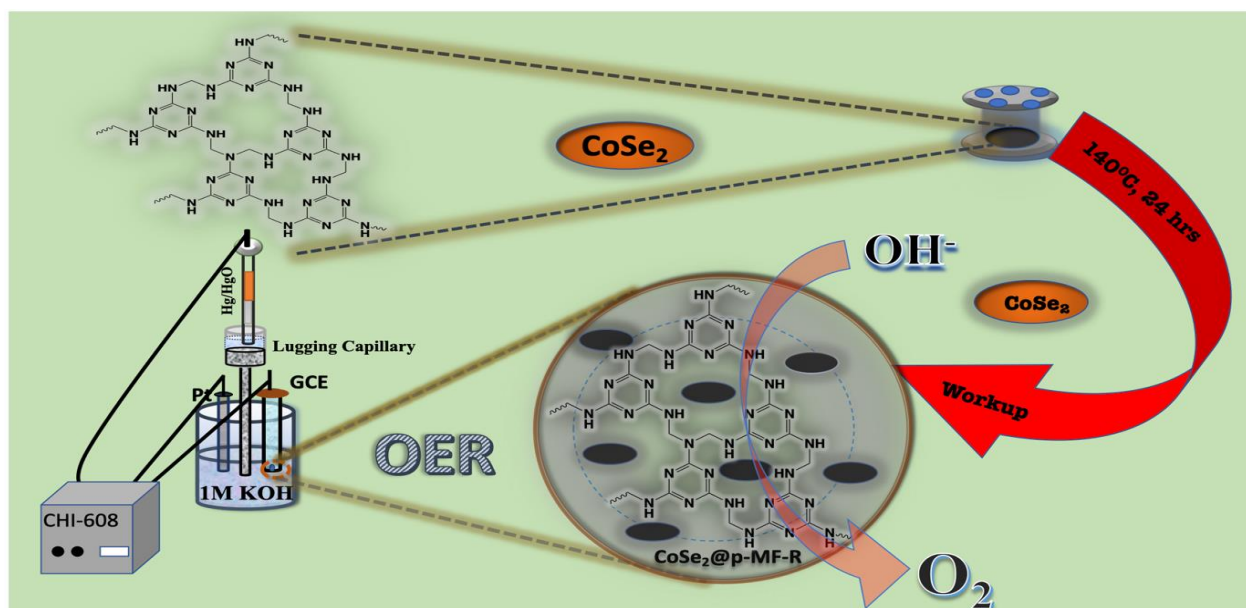
Scheme. 2. Schematically illustration for synthesis of CoSe$_2$@pMF-R.

4. Experimental setup for electrochemical studies:

The electrochemical properties of all samples were examined on a CHI 608C, in which a glassy carbon electrode (GC) (0.07 cm^2) was used as the working electrode, a Hg/HgO electrode (E$^\circ$ = 0.098 V vs NHE) as the reference electrode, and a platinum foil (~7 cm^2) as the counter electrode. The electrocatalytic activity for OER was carried out in 1 M KOH electrolyte. Using Nafion (5 wt%) in 495 µL of ethanol, a catalyst ink was prepared. A sonicated ink having electrocatalyst loading (3.28 mg/cm^2) was dropped onto the pre-polished GC electrode and dried. All electrochemical data was instrumentally iR-corrected and further to reduce the solution resistance (iR drop) between the working electrode and the cell solution, the reference electrode was connected to the cell solution via the Luggin capillary (the KCl/ agar–agar salt bridge). Cyclic voltammetry (CV) was carried out in 1 M KOH in potential range of -0.02 V– 1.9 V vs RHE at different scan rates (5 mV/s to 120 mV/s). Tafel polarization curves were obtained at room temperature at 0.5 mV/s. The electrochemical impedance study (EIS) or Nyquist plots were carried out in a frequency range of 1 mHz to 1 MHz at a certain dc-potential

1.43V vs RHE. All measured potentials were calibrated and converted to the reversible hydrogen electrode using equation ($E_{(RHE)} = E_{(Hg/HgO)} + E^°_{(Hg/HgO)} + 0.0591 \times pH$), where $E_{(Hg/HgO)}$ is the observed potential vs. Hg/HgO, pH for the 1 M KOH electrolyte found to be 13.8, and $E^°_{(Hg/HgO)}$ is 0.098 V for Hg/HgO.

5. Result and Discussion:

5.1. Physicochemical Characterization:

5.1.1. pXRD:

The synthesis of pMF-R, $CoSe_2$ and $CoSe_2$@pMF-R was confirmed by their powder-XRD data. Fig. 1(a) shows the broad amorphous peak corresponds to the polymeric pMF-R peak at $2\theta =$ 26.8, is representing plane (002). The XRD of the synthesised $CoSe_2$@pMF-R in Fig. 1(a) composite shows a diffraction pattern comparable to that of pure $CoSe_2$ (PDF#**53-0449**). The XRD peaks obtained at $2\theta = $ 24.50, 30.57, 35.20, 42.86, 44.34, 46.23, 52.45, 56.32, 63.31, and 65.75 correspond to the $CoSe_2$ facets (110), (101), (111), (210), (121), (220), (002), (031), (310) and (122) [24].
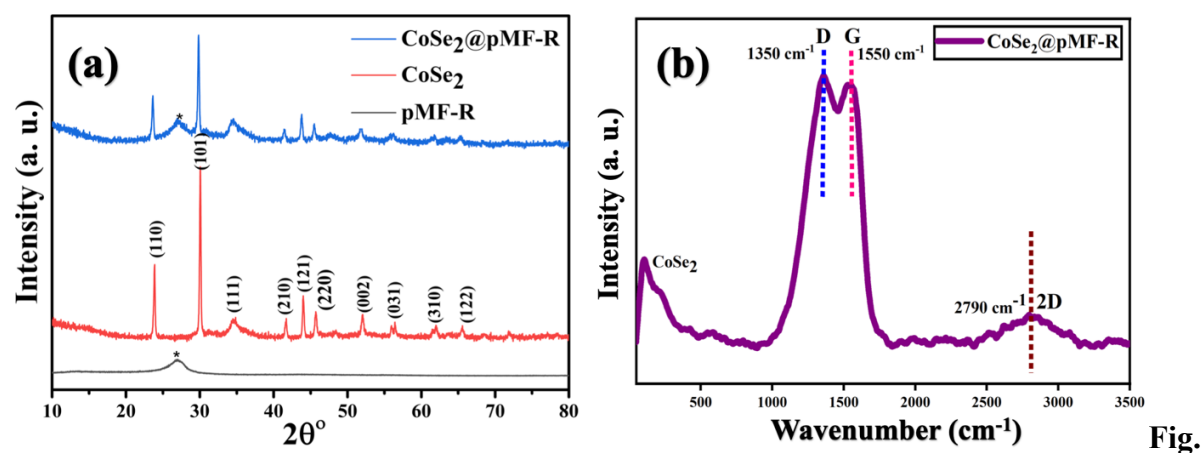
1(a) XRD pattern of pMF-R (*), $CoSe_2$ **(PDF#53-0449)**, $CoSe_2$@pMF-R particles; **(b)** Raman spectra of $CoSe_2$@pMF-R, and corresponding **D** (1350cm^{-1}), **G** (1550cm^{-1}), **2D** (2790cm^{-1}) peaks; peak at 170 cm^{-1} represents the presence of $CoSe_2$.

5.1.2. Raman Spectrum: The Raman spectrum of $CoSe_2@pMF$-R is depicted in Fig. 1(c). The (I_D/I_G) = 1.14 of $CoSe_2@pMF$-R, which is showing defects for carbon (*i.e.* pMF-R) in $CoSe_2@pMF$-R. The two most common peaks in Raman spectra are the D-band (amorphous) at a frequency of 1350 cm^{-1}, which originates from elastic scattering defects of amorphous lattices (blue line), and the G-band (1550 cm^{-1}), which results as single-phonon emission from tangential vibrational mode of graphitic domains define $CoSe_2@pMF$-R crystalline nature [25]. Due to the width of its D-band, pMF-R has a significant level of interstitial disorder. Additionally, a weak G-band signal points to the existence of graphitic nanodomains. Regarding pMF-R, the strength of the D-band indicates that the amorphous network is more as compared to crystalline carbon layers and graphitic domain edges [26, 27]. This occurs simultaneously with the 2D-broadened peak (2790 cm^{-1}), which is expected to be the result of some defect contribution. In $CoSe_2@pMF$-R composite there is a peak (171 cm^{-1}) of $CoSe_2$ that indicates the presence of $CoSe_2$ [28, 29].

5.1.3. FE-SEM: The morphology of $CoSe_2@pMF$-R was identified by FE-SEM at different magnifications. At micro level, $CoSe_2@pMF$-R was observed the particles with rough surface like morphology with irregular distribution throughout the surface as shown in Fig. 2(a). However, at nanoscale magnification, Fig. 2(b) (an enlarged view of Fig. 2(a)) shows flakes of $CoSe_2$ in polymeric network of pMF-R. This special structure facilitates the transfer of electrons during oxygen evolution. Simultaneously, the structure provides a wide active surface area, which will provide more active sites for OER [30].
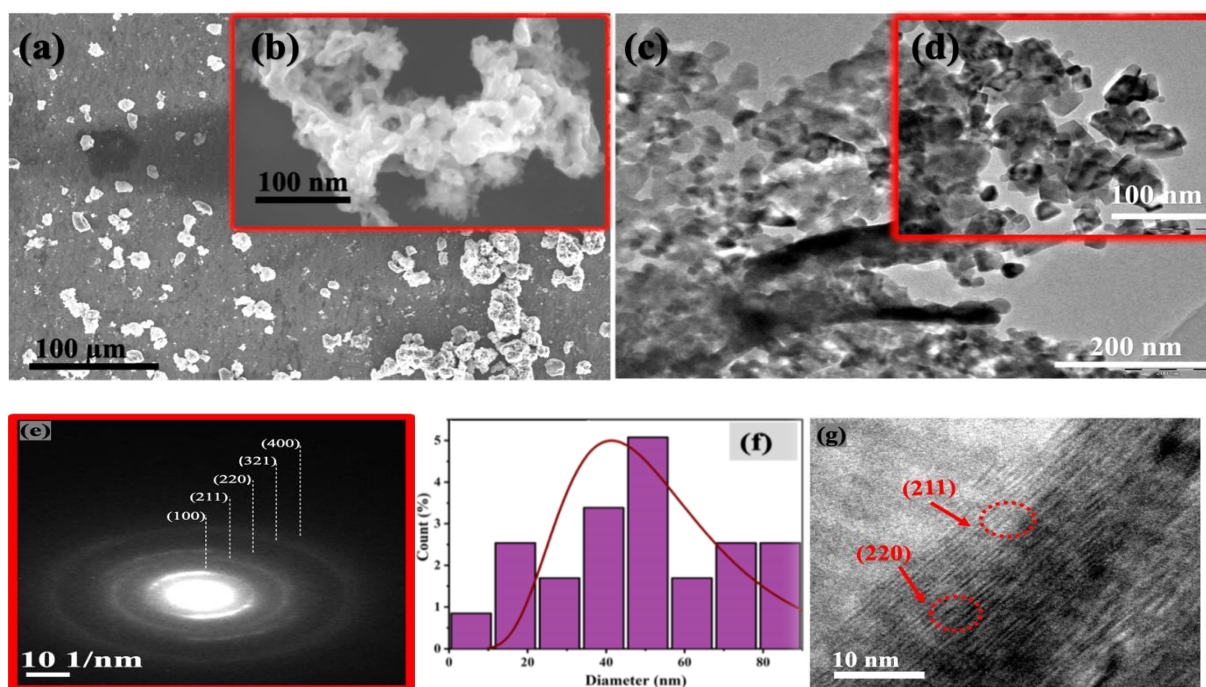
Fig. 2. FE-SEM and TEM images, **(a)** CoSe$_2$@pMF-R FE-SEM image at low resolution; **(b)** CoSe$_2$ grafted on the surface of pMF-R; **(c)** TEM image CoSe$_2$@pMF-R (200 nm); **(d)** CoSe$_2$ randomly distributed on the surface of pMF-R (100 nm); **(e)** SAED pattern analysis; **(f)** Average Particles size; **(g)** HR-TEM image of CoSe$_2$ nanoparticle, exhibits lattice fringes (10 nm) and defects.

5.1.4. TEM: Fig. 2(c) and (d) shows corresponding TEM at different magnifications. Similarly, Fig. 2(e) showed SAED patterns, which are showing amorphous as well as crystalline nature and showing corresponding planes. Some particles are integrated in the layered architecture, can be seen in Fig. 2(c). The particles with an average size of 43 nm are shown in Fig. 2(f). It is reasonable to assume that the method may successfully prevent particle aggregation and limit CoSe$_2$ particle size, resulting in a significant electrochemical surface area of CoSe$_2$@pMF-R. Particularly, the hetero-interfaces have a greater number of faults and disorders, which will result in more readily accessible active sites. Additionally, the hetero-structures have the ability to modify the d-band centre, which is essential for improving OER performance [31]. The identifiable lattice fringe at 0.24 nm corresponds to (211) plane of CoSe$_2$, Fig. 1(g) [32, 33].

5.1.5. XPS: The catalyst was investigated using X-ray photon spectroscopy (XPS) for coordination environment and chemical state. To analyse the elements, present in CoSe$_2$@pMF-R composite survey has done, as it can be seen in Fig. 3(a), Co, Se, C, O, and N elements were identified; hence, the survey peaks are showing complete information on the existence of different types of elements present in composites in different forms and at distinct binding energy positions. The oxidation states and coordination environment of catalyst are the parameters that determine the electrocatalyst's activity in terms of alkaline water electrolysis. The binding states corresponds to spin-orbit coupling for Co 2p$_{3/2}$ and Co 2p$_{1/2}$ were revealed by spectral analysis of the Co 2p spectra in Fig. 3(b), at 779.1 and 795.08 eV, respectively. Both the peak of Co 2p (Co 2p$_{3/2}$ and Co 2p$_{1/2}$) were ahead, split into two different binding energy at 779.1 and 781.1 eV, respectively, exhibiting the Co-Se and Co-O bonds, and at 785.68 eV a satellite peak was observed for Co 2p [34]. The Co2p$_{1/2}$ peak was ahead at 795.08 eV and split into two separate peaks at 794.58 eV and 795.78 eV due to spin-orbit coupled phenomena, which provided the Co-N and Co^{2+} peaks, respectively [35]. At 803.75 eV, a small, solitary peak was found, that was oxidised cobalt owing to air oxidation [36, 37], The XPS spectrum of Se 3d in CoSe$_2$@pMF-R was given in (Fig. 3c), here the major peak was obtained at 59.2 eV, which corresponds to Se 3d$_{3/2}$ [38]. Other peaks at 58.8 eV and 60.4 eV define the Se-C [39, 40], bond formation and surface oxidation of selenium [41], and the peak at 58.8 eV confirms the presence of the CoSe$_2$@pMF-R composite. Fig. 3(d), demonstrates the first XPS spectra of carbon in CoSe$_2$@pMF-R resin, which shows three distinct peaks of carbon attached to N and carbon itself at different binding energies. The broad peak at 284.2 eV corresponds to the C-C bond peak in CoSe$_2$@pMF-R composite, which is further split into two distinct peaks at 284.2 and 284.7 eV, which correspond to the C-C and C-N peaks in the composite. The small peak shown at 285.6 describes the C=N peak in CoSe$_2$@pMF-R composite [42]. Because of the presence of different aromatic moieties in the precursor used to make the CoSe$_2$@pMF-R

composite, a peak at 291.28 was observed, which corresponded to a satellite peak [43]. Now in CoSe$_2$@pMF-R, there is a single broad peak of N-1s shown in Fig. 3(e) at 399.6 eV that has been deconvoluted into three distinct peaks separately, in which the peaks at 399.5, 399.7, and 398.4 eV define the bond formation of the Co-N bond, the pyridinic type bond (C=N-C), and the C-NH-C bond formation, respectively [44, 45, 46]. The peak at 399.5 gives information on the formation of the CoSe$_2$@pMF-R composite by giving the Co-N bond in the XPS spectrum separately.

5.1.6. BET: The synthesized CoSe$_2$@pMF-R having increased surface area is also a reason of increased electrocatalytic activity. Initially, the surface area of pMF-R was found to be 1.4 m^2 g^{-1} and for CoSe$_2$ 7.1 m^2 g^{-1}. After the formation of composite it increased up to 21.8 m^2 g^{-1} as shown in Fig. 3(f).
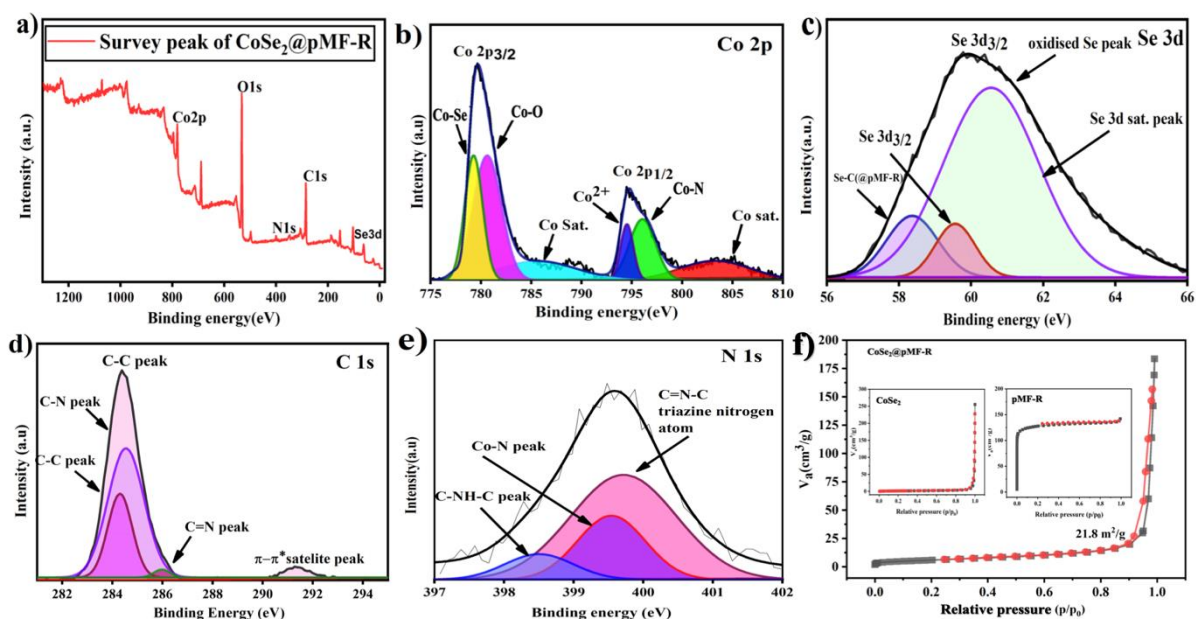
Fig. 3 (a) XPS Survey peak of CoSe$_2$@pMF-R and high resolution spectra in; **(b)** Co 2p; **(c)** Se 3d; **(d)** C 1s; **(e)** N 1s. **(f)** BET plot of CoSe$_2$@pMF-R, In Inset CoSe$_2$, pMF-R has represented.

5.6. Electrocatalytic studies:

Prior to electrochemical studies of fresh electrocatalysts, viz., $CoSe_2$, pMF-R and $CoSe_2$@pMF-R, an OCP was observed in 1 M KOH. Thereafter, 10 cyclic voltammograms at 20 mVs^{-1} were recorded in potential range of -0.02 V to 1.98 V vs RHE in order to stabilise the electrochemical system. The nature of CV of all electrocatalysts were almost similar for $CoSe_2$ and $CoSe_2$@pMF-R and it has been seen in other $Co(OH)_2$ and CoO_x films and it has been attributed to an irreversible oxidation of $Co(OH)_2$ to Co-OOH [47]. The oxygen evolution reaction in $CoSe_2$@pMF-R begins at a lower over potential of 1.56 V (vs. RHE), whereas the OER in a $CoSe_2$ and PMF-R begins at a slightly higher potential of 1.62 V (vs. RHE) and 1.7 V (vs. RHE) respectively, which is indicating the composite's better efficiency towards electrochemical processes. Both chalcogenides coated electrodes showed better OER current, when compared to pMF-R electrode. Similarly, from CV Fig. 4(a) it is noted that the $CoSe_2$@pMF-R composite found to have 1.608 V vs RHE at 10 mA/cm^2 as represented in which is quite high current density. Fig. 4(a) in inset, a plot between current density Vs (scan rate)$^{1/2}$ found to be linear and confirmed that the reaction at electrode/electrolyte interface is diffusion controlled. On the other hand, the ECSA is a reflection of electrocatalytically active sites and different catalyst's ECSA values were approximated based on the cyclic voltammograms in the non-faradaic potential windows. As shown in Fig. 4(b), $CoSe_2$@pMF-R possess high C_{dl} value of 3.0335 mF cm^{-2}. The reported C_{dl} for ideal flat GC electrode is ($\sim$ 60 µF cm^{-2}) [48]. So, for R_f (Roughness Factor) $= \frac{C_{dl}}{60} \times 1000$; and from this ECSA can be calculated as, ECSA $= (R_f \times S)$; S=0.07 cm^2 corresponds to electrode geometrical area. Table.1 asserted calculated data of C_{dl}, R_f and ECSA for $CoSe_2$@pMF-R, $CoSe_2$ and pMF-R. Result showed that composite electrocatalyst has significantly high electrochemically active surface area roughness factor as well as C_{dl} values. Furthermore, AC impedance measurements has

been also carried out and Nyquist plots of $CoSe_2$, pMF-R and $CoSe_2$@pMF-R were recorded in a wide range of frequency, 0.01 Hz to 100 kHz, at different potentials viz., before onset potential, at onset potential and during oxygen evolution reaction. Nyquist plots (Fig. 4(c)) of all electrocatalysts have characteristic typical curve with at least two time constants, corresponding to high (100 kHz to ~17.4 kHz), and low (8.07 Hz-0.01Hz) frequencies, a semicircle was observed at high frequency region corresponding to the charge transfer reaction at electrocatalyst/electrolyte interface. This is followed by capacitive behaviour of electrode at low frequency region. We observed three time constants in case of $CoSe_2$@pMF-R viz., semi-circle in high frequency region, finite Warburg region (11.8 mHz – 45.4 mHz), wherein $\frac{|Zim|}{|Zreal|}$ value is almost unity, and with decreased frequency the value increased from unity, thereafter at lower frequency region the impedance response appears to be of capacitive nature (as CPE value, frequency power n approaches to 1). In order to approximate the experimental impedance data with the ideal or distributed impedance elements, an equivalent circuit R(QR)W(QR) has been proposed for the composite electrode $CoSe_2$@pMF-R as shown in Fig. 4(d).

49
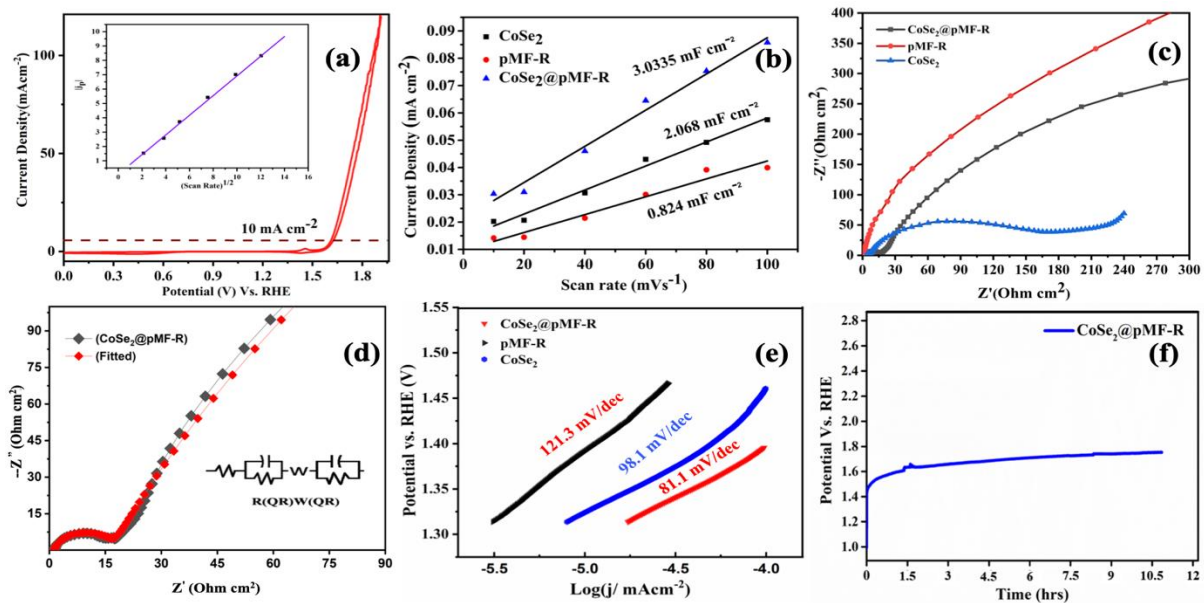
Fig.4 (a) 10 mA cm^{-2} reached at 1.608 V, In inset corresponding diffusion control plot at different scan rates; **(b)** C$_{dl}$ plot for CoSe$_2$@pMF-R, pMF-R, CoSe$_2$; **(c)** Nyquist EIS plot of CoSe$_2$, pMF-R and CoSe$_2$@pMF-R; **(d)** Fitted Nyquist plots of CoSe$_2$@pMF-R at 1.56 V vs RHE showing circuit fitting it with parameters R(QR)W(QR)**; (e)** Tafel slope of CoSe$_2$, pMF-R and CoSe$_2$@pMF-R **(f)** Chronopotentiometry test for 12 hrs at constant current 10 mA cm^{-2}**.**

On the other hand for pMF-R electrode, we have observed a finite length Warburg diffusion element at low frequencies followed by constant-phase element (CPE) (replaced by double layer capacitance when frequency power approaches to 1 attributed to a porous composite electrode/electrolyte interface. Nyquist plots of pMF-R found to fitted with equivalent circuit R(Q(RW)) and we have observed characteristic finite Warburg region (255 mHz - 66.4 mHz) in series with CPE. It is a common feature in case of an ion intercalation into inorganic/polymer host matrix [49, 50]. However, in case of CoSe$_2$, equivalent circuit CR(QR)(QR) does not showed any Warburg region and thus evident non-porous electrode material.

5.6.1. Electrocatalytic activity:

The iR-corrected comparative anodic Tafel polarization curves of CoSe$_2$, pMF-R and CoSe$_2$@pMF-R on GC at a scan rate of 0.2 mVs^{-1} in 1 M KOH at 25 °C have been shown in Fig. 4(e), . Out of all, CoSe$_2$@pMF-R shows a better electrocatalytic activity, in the potential region up to (1.25 - 1.55 V vs. RHE). The observed value of the Tafel slope of CoSe$_2$@pMF-R is 81.1 mV dec^{-1} and follow electrochemical mechanistic paths in the lower potential region, which is close to (2.303RT/2F). On the contrary, CoSe$_2$ and pMF-R have high Tafel slope values viz., 98.1 mV dec^{-1} and 121.3 mV dec^{-1} , respectively, in the lower potential region. It is noteworthy that the Tafel slope values obtained in the present study with CoSe$_2$@pMF-R are similar to those found in the literature [51]. In order to evaluate stability of the CoSe$_2$@pMF-R electrocatalysts in 1 M KOH, it was examined under static current of 10 mA cm^{-2} for 15

hours and the potential nearly found steady (98 %) throughout experiment and shown in Fig. 4(f). The electrocatalytic activity was estimated from the polarisation curve in terms of the current density at overpotential (η) 640 mV. 'η' is the anodic overpotential, which is also known as the formal overpotential and is determined by the relation $\eta = E^{\square} - E^{\square}_{O2/OH^-}$, where, E and ($E_{O2/OH^-} = 0.303$ V vs. Hg/HgO) are the applied potentials across the electrocatalyst 1 M KOH interface and the theoretical equilibrium Nernst potential in 1 M KOH at 25 °C, respectively. The observed electrocatalytic activity of the CoSe$_2$@pMF-R at 10 mA cm^2 is compared with the literature as given in bar graph Fig. 5(a), 5(b), (CoSe$_2$ based previously reported electrocatalyst composite materials) and found to be on par with most of the synthesized CoSe$_2$-based electrocatalysts.
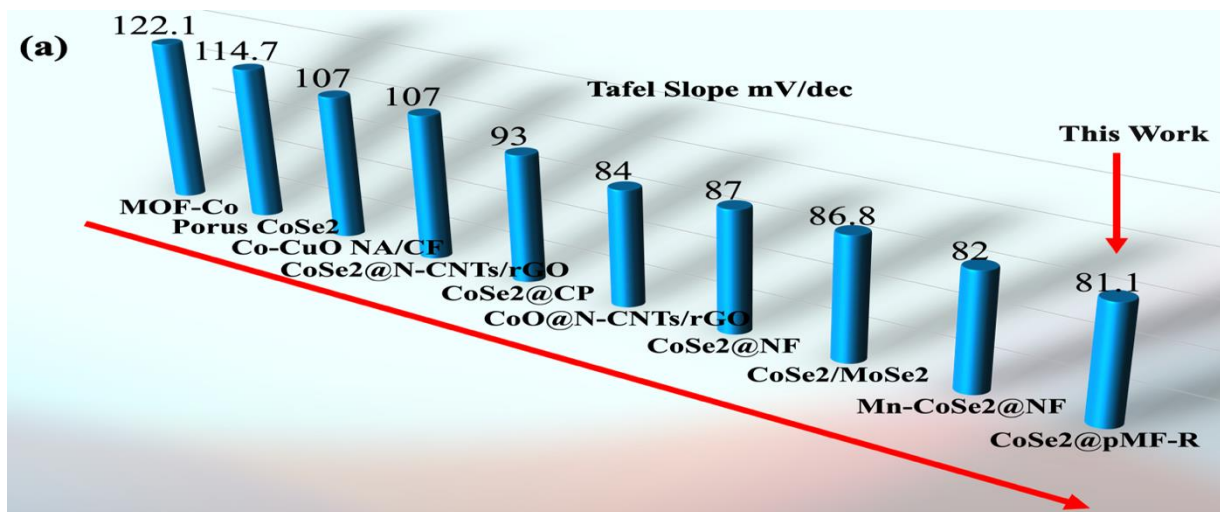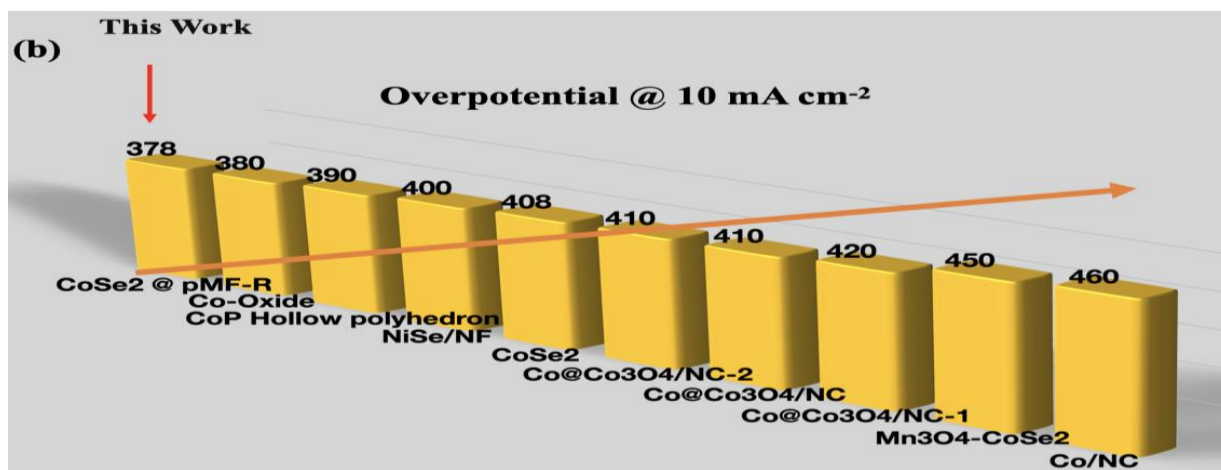
Fig. 5 Comparison bar graph of **(a)** Tafel slope [52 - 57]**; (b)** Overpotential [58 - 62], of different previously reported cobalt and selenium based electrocatalyst.

This demonstrates that the activity observed is attributable to the composite of $CoSe_2$ and polymerised melamine formaldehyde resin (pMF-R) backbone. As it is evident from data that mere $CoSe_2$ and pMF-R have high Tafel slope values but together their synergistic effect facilitates facile electron transfer and provides more active sites for OER [63-65]. Further, the increase in the electrocatalytic property of composite might be due to the presence of graphitic domain of pMF-R (confirmed from Raman Data), pyridinic N, bonding of Co-N and Se-C (confirmed from XPS data) [66, 67].

Conclusion:

We have synthesized $CoSe_2$ nanoparticles, pMF-R and novel $CoSe_2$@pMF-R composite, and later characterized by XRD, Raman, XPS, BET, FE-SEM, HRTEM and result confirmed synthesis of all prepared electrocatalysts and found to be in agreement with its electrocatalytic activity. The electrochemical characterization viz., cyclic voltammetry, Tafel polarization and electrochemical Impedance spectroscopy of all electrocatalysts showed that out of all, composite electrocatalyst exhibited excellent electrocatalytic properties towards OER. The electron transfer that occurs in this hybrid structure increases the density of electronic state of

cobalt ions by moving electrons from pMF-R to CoSe₂. The bonding between Cobalt ions and intermediate species during oxygen evolution would be enhanced by optimizing the electronic structure management of metallic Se-Co phase. Furthermore, the presence of pMF-R greatly boosts the conductivity of cobalt di-selenide and encourages charge transfer

Reference:

1. N.-T. Suen, S.-F. Hung, Q. Quan, N. Zhang, Y.-J. Xu, H.-M. Chen, Electrocatalysis for the oxygen evolution reaction: Recent development and future perspectives, Electrochim. Acta 46 (2017) 337–365, https://doi.org/10.1039/c6cs00328a.
2. **Yang, X.**, **Zhao, Z.**, **Yu, X.**, & **Feng, L.** (2019). Electrochemical hydrogen evolution reaction boosted by constructing Ru nanoparticles assembled as a shell over semimetal Te nanorod surfaces in acid electrolyte. *Chemical Communications*, **55**, 2096-2099. https://doi.org/10.1039/C8CC09993F
3. **L. Zhong, Y. Bao, X. Yu, L. Feng**, An Fe-doped NiTe bulk crystal as a robust catalyst for the electrochemical oxygen evolution reaction, *Chem. Commun.* **55** (2019) 9507–9510. https://doi.org/10.1039/C9CC04429A
4. **H. Huang, A. Cho, S. Kim, H. Jun, A. Lee, J.W. Han**, Structural design of amorphous CoMoPx with abundant active sites and synergistic catalysis effect for effective water splitting, *Adv. Funct. Mater.* **30** (2020) 2003889. https://doi.org/10.1002/adfm.202003889
5. **A.Wang, L. Cheng, X. Shen, X. Chen, W. Zhu, W. Zhao, C. Lv**, Porphyrin coordination polymer/Co1−xS composite electrocatalyst for efficient oxygen evolution reaction, *Chem. Eng. J.* **387** (2020) 125975. https://doi.org/10.1016/j.cej.2020.125975
6. **A. Bist, B. Pant, G.P. Ojha, J. Acharya, M. Park, P.S. Saud**, Novel Materials in Perovskite Solar Cells: Efficiency, Stability, and Future Perspectives, *Nanomaterials* **13** (2023) 1724. https://doi.org/10.3390/nano13111724
7. **Y. Zhu, Q. Lin, Y. Zhong, H.A. Tahini, Z. Shao, H. Wang**, Metal oxide-based materials as an emerging family of hydrogen evolution electrocatalysts, *Energy Environ. Sci.* **13** (2020) 3361–3392. https://doi.org/10.1039/D0EE02485F
8. **A. J. Huang, S. Wang, J. Nie, C. Huang, X. Zhang, B. Wang, J. Tang, C. Du, Z. Liu, J. Chen**, Active site and intermediate modulation of 3D CoSe2 nanosheet array

on Ni foam by Mo doping for high-efficiency overall water splitting in alkaline media, *Chem. Eng. J.* **402** (2020) 128055. https://doi.org/10.1016/j.cej.2020.128055

9. **J. Li, G. Liu, B. Liu, Z. Min, D. Qian, J. Jiang, J. Li**, Fe-doped CoSe2 nanoparticles encapsulated in N-doped bamboo-like carbon nanotubes as an efficient electrocatalyst for oxygen evolution reaction, *Electrochim. Acta* **264** (2018) 390–398. https://doi.org/10.1016/j.electacta.2018.01.211

10. **S. Chen, J.-L. Mi, P. Zhang, Y.-H. Feng, Y.-C. Yong, W.-D. Shi**, Control synthesis of nickel selenides and their multiwalled carbon nanotubes composites as electrocatalysts for enhanced water oxidation, *J. Phys. Chem. C* **122** (2018) 26096–26104. https://doi.org/10.1021/acs.jpcc.8b09259

11. **A. Nadeema, P.S. Walko, R.N. Devi, S. Kurungot**, Alkaline water electrolysis by NiZn-double hydroxide-derived porous nickel selenide-nitrogen-doped graphene composite, *ACS Appl. Energy Mater.* **1** (2018) 4742–4753. https://doi.org/10.1021/acsaem.8b01081

12. **D. Selvakumar, G. Murugadoss, A. Alsalme, A.M. Alkathiri, R. Jayavel**, Heteroatom doped reduced graphene oxide paper for large area perovskite solar cells, *Sol. Energy* **163** (2018) 552–561. https://doi.org/10.1016/j.solener.2018.01.084

13. **S. Chen, J.-L. Mi, P. Zhang, Y.-H. Feng, Y.-C. Yong, W.-D. Shi**, Control synthesis of nickel selenides and their multiwalled carbon nanotubes composites as electrocatalysts for enhanced water oxidation, *J. Phys. Chem. C* **122** (2018) 26096–26104. https://doi.org/10.1021/acs.jpcc.8b09259

14. **G. Wei, K. Du, X. Zhao, J. Wang, W. Yan, C. An, C. An**, Cable-like carbon nanotubes decorated metal-organic framework derived ultrathin CoSe2/CNTs nanosheets for electrocatalytic overall water splitting, *Chin. Chem. Lett.* **31** (2020) 1723–1726. https://doi.org/10.1016/j.cclet.2020.02.029

15. **Q. Zhou, Y. Guo, Z. Ye, Y. Fu, Y. Guo, Y. Zhu**, Carbon nitride photocatalyst with internal electric field induced photogenerated carriers spatial enrichment for enhanced photocatalytic water splitting, *Mater. Today* **58** (2022) 93–100. https://doi.org/10.1016/j.mattod.2022.06.009

16. **R. Zhao, Z. Liang, R. Zou, Q. Xu**, Metal-organic frameworks for batteries, *Joule* **2** (2018) 2235–2259. https://doi.org/10.1016/j.joule.2018.09.019

17. **D. Xu, X. Long, J. Xiao, Z. Zhang, G. Liu, H. Tong, Z. Liu, N. Li, D. Qian, J. Li, J. Liu**, Rationally constructing CoO and CoSe2 hybrid with CNTs-graphene for impressively enhanced oxygen evolution and DFT calculations, *Chem. Eng. J.* **425** (2021) 129982. https://doi.org/10.1016/j.cej.2021.129982

18. **Z. Li, W. Niu, L. Zhou, Y. Yang**, Phosphorus and aluminum codoped porous NiO nanosheets as highly efficient electrocatalysts for overall water splitting, *ACS Energy Lett.* **3** (2018) 629–635. https://doi.org/10.1021/acsenergylett.8b00174

19. **Yanshuo Jin, Haotian Wang, Junjie Li, Xin Yue, Yujie Han, Pei Kang Shen, Yi Cui**, Porous MoO2 nanosheets as non-noble bifunctional electrocatalysts for overall water splitting, *Adv. Mater.* **28** (2016) 3785–3790. https://doi.org/10.1002/adma.201506314

20. **Seung-Keun Park, Jin Koo Kim, Yun Chan Kang**, Excellent sodium-ion storage performances of CoSe2 nanoparticles embedded within N-doped porous graphitic carbon nanocube/carbon nanotube composite, *Chem. Eng. J.* **328** (2017) 556–563. https://doi.org/10.1016/j.cej.2017.07.079

21. **Jiabao Li, Dong Yan, Ting Lu, Yefeng Yao, Likun Pan**, An advanced CoSe embedded within porous carbon polyhedra hybrid for high performance lithium-ion and sodium-ion batteries, *Chem. Eng. J.* **325** (2017) 14–23. https://doi.org/10.1016/j.cej.2017.05.046

22. **Ali Dorieh, Mohammad Farajollah Pour, Sogand Ghafari Movahed, Antonio Pizzi, Peyman Pouresmaeel Selakjani, Mohammad Valizadeh Kiamahalleh, Hamid Hatefnia, Mohammad Hassan Shahavi, Roozbeh Aghaei**, A review of recent progress in melamine-formaldehyde resin based nanocomposites as coating materials, *Prog. Org. Coat.* **170** (2022) 106768. https://doi.org/10.1016/j.porgcoat.2022.106768

23. **M.C.D. Cooray, X. Zhang, Y. Zhang, S.J. Langford, A.M. Bond, J. Zhang**, Cobalt selenide nanoflake decorated reduced graphene oxide nanocomposite for efficient glucose electro-oxidation in alkaline medium, *J. Mater. Chem. A* **5** (2017) 19289–19296. https://doi.org/10.1039/c7ta04742h

24. **X. Huang, S. Bai, Z. Liu, T. Hasunuma, A. Kondo, S.-H. Ho**, Fermentation of pigment-extracted microalgal residue using yeast cell-surface display: direct high-density ethanol production with competitive life cycle impacts, *Green Chem.* **21** (2019) 7026–7037. https://doi.org/10.1039/C9GC02634G

25. **Y. Lin, L. Yang, Y. Zhang, H. Jiang, Z. Xiao, C. Wu, G. Zhang, J. Jiang**, Defective Carbon–CoP Nanoparticles Hybrids with Interfacial Charges Polarization for Efficient Bifunctional Oxygen Electrocatalysis, *Adv. Energy Mater.* **8** (2018) 1703623. https://doi.org/10.1002/aenm.201703623

26. **A. S. R. Bati, L. Yu, M. Batmunkh, J. G. Shapter**, Synthesis, purification, properties and characterization of sorted single-walled carbon nanotubes, *Nanoscale* **10** (2018) 21633–21675. https://doi.org/10.1039/C8NR07379A

27. M.S. Dresselhaus, G. Dresselhaus, R. Saito, A. Jorio, Raman spectroscopy of carbon nanotubes, Phys. Rep. **409** (2005) 47–99. https://doi.org/10.1016/j.physrep.2004.10.006.

28. Sajjad Hussain, Kamran Akbar, Dhanasekaran Vikraman, Hailiang Liu, Seung-Hyun Chun, Jongwan Jung, $WS_2/CoSe_2$ heterostructure: A designed structure as catalysts for enhanced hydrogen evolution performance, *J. Ind. Eng. Chem.* **64** (2018) 90–99. https://doi.org/10.1016/j.jiec.2018.04.025.

29. Jing Yang, Chunde Wang, Huanxin Ju, Yuan Sun, Shiqi Xing, Junfa Zhu, Qing Yang, Integrated quasiplane heteronanostructures of $MoSe_2/Bi_2Se_3$ hexagonal nanosheets: Synergetic electrocatalytic water splitting and enhanced supercapacitor performance, *Adv. Funct. Mater.* **28** (2018) 1703864. https://doi.org/10.1002/adfm.201703864.

30. Zhiguo Niu, Ce Qiu, Jing Jiang, Lunhong Ai, Hierarchical CoP–FeP branched heterostructures for highly efficient electrocatalytic water splitting, *ACS Sustainable Chem. Eng.* **7** (2019) 2335–2342. https://doi.org/10.1021/acssuschemeng.8b05089.

31. Menglei Yuan, Sobia Dipazir, Meng Wang, Yu Sun, Denglei Gao, Yiling Bai, Min Zhang, Peilong Lu, Hongyan He, Xiangyang Zhu, Shuwei Li, Zhanjun Liu, Zhaopeng Luo, Guangjin Zhang, Polyoxometalate-assisted formation of $CoSe/MoSe_2$ heterostructures with enhanced oxygen evolution activity, *J. Mater. Chem. A* **7** (2019) 7943–7954. https://doi.org/10.1039/C8TA11976G.

32. Xiaobin Liu, Yongchang Liu, Li-Zhen Fan, MOF-derived $CoSe_2$ microspheres with hollow interiors as high-performance electrocatalysts for the enhanced oxygen evolution reaction, *J. Mater. Chem. A* **5** (2017) 17320–17325. https://doi.org/10.1039/c7ta04662f.

33. Manisha Das, Ashmita Biswas, Zubair Bashir Khan, Ramendra Sundar Dey, Tuning the electronic structure of cobalt selenide on copper foam by introducing a Ni buffer layer for highly efficient electrochemical water splitting, *Inorg. Chem.* **61** (2022) 13218–13225. https://doi.org/10.1021/acs.inorgchem.2c02325.

34. Hengyi Li, Dong Gao, Xuan Cheng, Simple microwave preparation of high activity Se-rich $CoSe_2$/C for oxygen reduction reaction, *Electrochim. Acta* **141** (2014) 229–235. https://doi.org/10.1016/j.electacta.2014.06.065.

35. Yong Zhao, Lei Jiang, Hollow micro/nanomaterials with multilevel interior structures, *Adv. Mater.* **21** (2009) 3621–3638. https://doi.org/10.1002/adma.200803645.

36. Qianqian Huang, Jiayin Zhang, Zhengyu He, Penghui Shi, Xin Qin, Weifeng Yao, Direct fabrication of lamellar self-supporting Co_3O_4/N/C peroxymonosulfate activation catalysts for effective aniline degradation, *Chem. Eng. J.* **313** (2017) 724–733. https://doi.org/10.1016/j.cej.2016.11.002.

37. Chao Wang, Chuanhui Zhang, Wenchao Hua, Yanglong Guo, Guanzhong Lu, Sonia Gil, Anne Giroir-Fendler, Catalytic oxidation of vinyl chloride emissions over Co-Ce composite oxide catalysts, *Chem. Eng. J.* **314** (2017) 308–316. https://doi.org/10.1016/j.cej.2017.01.007.

38. H. van der Heide, R. Hemmel, C.F. van Bruggen, C. Haas, X-ray photoelectron spectra of 3d transition metal pyrites, *J. Solid State Chem.* **33** (1980) 17–25. https://doi.org/10.1016/0022-4596(80)90543-5.

39. Dong Suk Han, Bill Batchelor, Ahmed Abdel-Wahab, XPS analysis of sorption of selenium(IV) and selenium(VI) to mackinawite (FeS), *Environ. Prog. Sustain. Energy* **31** (2012) 71–79. https://doi.org/10.1002/ep.10609.

40. Manisha Das, Ashmita Biswas, Zubair Bashir Khan, Ramendra Sundar Dey, Tuning the electronic structure of cobalt selenide on copper foam by introducing a Ni buffer layer for highly efficient electrochemical water splitting, *Inorg. Chem.* **61** (2022) 13218–13225. https://doi.org/10.1021/acs.inorgchem.2c02325.

41. Yuxi Li, Na Luo, Wenshuang Zhang, Qingmin Hu, Xiaohong Wang, Yang Chen, Zhixuan Cheng, Jiaqiang Xu, Rational design and *in situ* growth of SnO_2/CMF composites: insightful understanding of the formaldehyde gas sensing mechanism and enhanced gas sensing properties, *J. Mater. Chem. C* **8** (2020) 8908–8917. https://doi.org/10.1039/D0TC01650K.

42. Yurui Xue, Zicheng Zuo, Yongjun Li, Huibiao Liu, Yuliang Li, Graphdiyne-supported $NiCo_2S_4$ nanowires: a highly active and stable 3D bifunctional electrode material, *Small* **13** (2017) 1700936. https://doi.org/10.1002/smll.201700936.

43. Jing Wang, Huiqing Liu, Lei Wang, Hongling Zhang, Haishan Luo, Yang Gao, Apparent permeability for gas transport in nanopores of organic shale reservoirs including multiple effects, *Int. J. Coal Geol.* **152** (2015) 21–30. https://doi.org/10.1016/j.coal.2015.10.004.

44. Huanhuan Zhou, Sheng Xu, Haiping Su, Mei Wang, Wenming Qiao, Licheng Ling, Donghui Long, Facile preparation and ultra-microporous structure of melamine–resorcinol–formaldehyde polymeric microspheres, *Chem. Commun.* **49** (2013) 4220–4222. https://doi.org/10.1039/C3CC41109E.

45. Herbert A. Weakliem, Optical spectra of Ni^{2+}, Co^{2+}, and Cu^{2+} in tetrahedral sites in crystals, *J. Chem. Phys.* **36** (1962) 2117–2140. https://doi.org/10.1063/1.1732840.

46. Michaela S. Burke, Matthew G. Kast, Lena Trotochaud, Adam M. Smith, Shannon W. Boettcher, Cobalt–iron (oxy)hydroxide oxygen evolution electrocatalysts: the role of structure and composition on activity, stability, and mechanism, *J. Am. Chem. Soc.* **137** (2015) 3638–3648. https://doi.org/10.1021/jacs.5b00281.

47. R.N. Singh, M. Malviya, Anindita, A.S.K. Sinha, P. Chartier, Polypyrrole and $La_{1-x}Sr_xMnO_3$ ($0 \leq x \leq 0.4$) composite electrodes for electroreduction of oxygen in alkaline medium, *Electrochim. Acta* **52** (2007) 4264–4273. https://doi.org/10.1016/j.electacta.2006.12.004.

48. M.D. Levi, D. Aurbach, Impedance of a single intercalation particle and of non-homogeneous, multilayered porous composite electrodes for Li-ion batteries, *J. Phys. Chem. B* **108** (2004) 11693–11703. https://doi.org/10.1021/jp0486402.

49. Hong Cao, Hailong Li, Linhao Liu, Kangning Xue, Xinkai Niu, Juan Hou, Long Chen, Salt-templated nanoarchitectonics of $CoSe_2$-NC nanosheets as an efficient bifunctional oxygen electrocatalyst for water splitting, *Int. J. Mol. Sci.* **23** (2022) 5239. https://doi.org/10.3390/ijms23095239.

50. Denis Antipin, Marcel Risch, Calculation of the Tafel slope and reaction order of the oxygen evolution reaction between pH 12 and pH 14 for the adsorbate mechanism, *Electrochem. Sci. Adv.* **2** (2022) e2100213. https://doi.org/10.1002/elsa.202100213.

51. Tian Chen, Songzhan Li, Jian Wen, Pengbin Gui, Guojia Fang, Metal–organic framework template derived porous $CoSe_2$ nanosheet arrays for energy conversion and storage, *ACS Appl. Mater. Interfaces* **9** (2017) 35927–35935. https://doi.org/10.1021/acsami.7b12403.

52. Xiaoli Xiong, Chao You, Zhiang Liu, Abdullah M. Asiri, Xuping Sun, Co-doped CuO nanoarray: an efficient oxygen evolution reaction electrocatalyst with enhanced activity, *ACS Sustainable Chem. Eng.* **6** (2018) 2883–2887. https://doi.org/10.1021/acssuschemeng.7b03752.

53. Deyao Xu, Xuanda Long, Juanxiu Xiao, Zhiliang Zhang, Guiyu Liu, Haixia Tong, Zeng Liu, Neng Li, Dong Qian, Junhua Li, Jinlong Liu, Rationally constructing CoO and $CoSe_2$ hybrid with CNTs-graphene for impressively enhanced oxygen evolution and DFT calculations, *Chem. Eng. J.* **421** (2021) 129982. https://doi.org/10.1016/j.cej.2021.129982.

54. Guijuan Wei, Zhuhan Xu, Xixia Zhao, Shoujuan Wang, Fangong Kong, Changhua An, N-doped $CoSe_2$ nanomeshes as highly efficient bifunctional electrocatalysts for water splitting, *J. Alloys Compd.* **883** (2021) 162328. https://doi.org/10.1016/j.jallcom.2021.162328.

55. Binbin Wei, Pengcheng Yao, Guisheng Tang, Zhengbing Qi, Wenshen Hu, Jinqing Hong, Cuixue Chen, Zhoucheng Wang, Mn-doped $CoSe_2$ nanosheets as high-efficiency catalysts for the oxygen evolution reaction, *Dalton Trans.* **48** (2019) 16178–16184. https://doi.org/10.1039/C9DT03108A.

56. Lu Xia, Jianjun Ou, Kuokuo Li, Hui Guo, Zhengmao Hu, Ting Bai, Jingping Zhao, Kun Xia, Fengyu Zhang, Genome-wide association analysis of autism identified multiple loci that have been reported as strong signals for neuropsychiatric disorders, *Autism Res.* **12** (2019) 1875–1886. https://doi.org/10.1002/aur.2229.

57. Arshad Aijaz, Justus Masa, Christoph Rösler, Wei Xia, Philipp Weide, Alexander J. R. Botz, Roland A. Fischer, $Co@Co_3O_4$ encapsulated in carbon nanotube-grafted nitrogen-doped carbon polyhedra as an advanced bifunctional oxygen electrode, *Angew. Chem. Int. Ed.* **55** (2016) 4087–4091. https://doi.org/10.1002/anie.201509382.

58. Min-Rui Gao, Yun-Fei Xu, Jun Jiang, Ya-Rong Zheng, Shu-Hong Yu, Water oxidation electrocatalyzed by an efficient $Mn_3O_4/CoSe_2$ nanocomposite, *J. Am. Chem. Soc.* **134** (2012) 2930–2933. https://doi.org/10.1021/ja211526y.

59. Chun Tang, Ningyan Cheng, Zonghua Pu, Wei Xing, Xuping Sun, NiSe nanowire film supported on nickel foam: an efficient and stable 3D bifunctional electrode for full water splitting, *Angew. Chem. Int. Ed.* **54** (2015) 9351–9355. https://doi.org/10.1002/anie.201503407.

60. Yuan Pan, Kaian Sun, Shoujie Liu, Xing Cao, Konglin Wu, Weng-Chon Cheong, Zheng Chen, Yu Wang, Yang Li, Yunqi Liu, Dingsheng Wang, Qing Peng, Chen Chen, Yadong Li, Core–shell ZIF-8@ZIF-67-derived CoP nanoparticle-embedded N-doped carbon

nanotube hollow polyhedron for efficient overall water splitting, *J. Am. Chem. Soc.* **140** (2018) 2610–2618. https://doi.org/10.1021/jacs.7b12420.

61. Zhong-Jie Jiang, Zhongqing Jiang, Interaction-induced high catalytic activities of CoO nanoparticles grown on nitrogen-doped hollow graphene microspheres for oxygen reduction and evolution reactions, *Sci. Rep.* **6** (2016) 27081. https://doi.org/10.1038/srep27081.

62. A. S. Chaddha, N. K. Singh, M. Malviya, A. Sharma, Birnessite-clay mineral couple in the rock varnish: a nature's electrocatalyst, *Sustain. Energy Fuels* **6** (2022) 2922–2930. https://doi.org/10.1039/D2SE00185C.

63. K. Kokila, N. Elavarasan, V. Sujatha, Diospyros Montana leaf extract-mediated synthesis of selenium nanoparticles and their biological applications, *New J. Chem.* **41** (2017) 7481–7490. https://doi.org/10.1039/c7nj01124e.

64. **Yagi, S.**, Yamada, I., Tsukasaki, H., Seno, A., Murakami, M., Fujii, H., Chen, H., Umezawa, N., Abe, H., Nishiyama, N., Mori, S., Covalency-reinforced oxygen evolution reaction catalyst. *Nat. Commun.* **6** (2015) 8249.

65. **Rossmeisl, J.**, Qu, Z.-W., Zhu, H., Kroes, G.-J., Nørskov, J.K., Electrolysis of water on oxide surfaces. *J. Electroanal. Chem.* **607** (2007) 83–89. https://doi.org/10.1016/j.jelechem.2006.11.008.

66. **Wahl, S.**, El-Refaei, S.M., Amsalem, P., Buzanich, A.G., Koch, N., Pinna, N., Operando diffuse reflectance UV-vis spectroelectrochemistry for investigating oxygen evolution electrocatalysts. *Catal. Sci. Technol.* **10** (2020) 727–734. https://doi.org/10.1039/C9CY02329A.

Article-4

Synergistic effect of iron oxide nanoparticles and single walled carbon nanotubes interface as a sensing platform for sulfasalazine electro oxidation

Suyash Mane and Sanghamitra Chatterjee[1]

Department of Chemistry, Institute of Chemical Technology, Matunga, Mumbai 400019, India

Abstract

The significance of sulfasalazine (SSZ) as a therapeutic agent has garnered paramount research interest in the design and fabrication of a viable sensor for the detection of SSZ. Herein, we demonstrate a new strategy for the sensitive determination of SSZ employing single walled carbon nanotubes decorated with Fe_3O_4 nanoparticles sensing platform for the first time. The synthesized Fe_3O_4 nanoparticles and the surface morphology of the developed sensor were investigated by exerting various analytical techniques. The optimization of operational parameters was effectuated. The developed sensor exhibited pronounced electrocatalytic activity for the electro oxidation of SSZ in the dynamic detection range of 25 nM – 1.5 µM manifesting noteworthy high sensitivity and phenomenal low detection limit of 18.6 µA µM^{-1} and 1.6 nM respectively. Apparent specificity in the presence of interferents along with remarkable stability and reproducibility were attained by the sensor. The prominence of the developed methodology was emphasized by the determination of SSZ in pharmaceutical formulations. Furthermore, the applicability of the developed electrode was established by utilizing it effectually for the first time to quantify SSZ in serum sample of patients undergoing pharmacological treatment for rheumatoid arthritis.

[*]Corresponding author. Tel.: +91-22-33611144

Email address: sk.chatterjee@ictmumbai.edu.in (S. Chatterjee)

1. Introduction

Rheumatoid arthritis (RA) which is a chronic autoimmune disease affecting the joints has transpired into a discernible concern affecting the global health since decades [1, 2]. Dorothy Hodgkin who was a pioneer in X-ray crystallography and was awarded in 1964 with Nobel Prize in chemistry had crippled hands and feet due to lifelong RA. Christiaan Barnard, known for performing first human to human heart transplant had to end his surgical career because of RA. Billy Bowden, the famous cricket umpire from New Zealand had the popularly known "crooked finger of doom" signal due to his suffering from RA. In order to circumvent the effects of RA, sulfasalazine (SSZ) is considered as a first line treatment which is on the World Health Organization's list of necessary medicines [3, 4]. SSZ which is an anti-inflammatory drug belongs to the aminosalicylate category and is widely prescribed for the cure of bowel disease [5, 6]. It is also effective in the treatment of ulcerative colitis and Crohn's disease [7-9]. SSZ is adequately administered for cancer treatment as it inhibits the cysteine transporter to induce apoptosis [10, 11]. The activity of SSZ is due to the combination of mesalazine and sulfapyridine, which are linked together by an azo bond in the moiety [12]. The exact mechanism of action of SSZ in the physiology is still an enigma [13]. However, the chronic use of SSZ exhibits some painful and adverse side effects such as rash, hypersensitivity, drowsiness, arthralgia, nephrotoxicity, lymphadenopathy, liver failure and eosinophilia. It deliberately causes semen abnormality and inferior testosterone production in men resulting to infertility [14-17]. Hence, the quantitation of SSZ in different matrices has become indispensable which necessitates the employment of a sensitive analytical technique.

Literature survey reveals that various conventional analytical techniques have been used previously for SSZ detection but limitations such as onerous extraction route, exorbitant

cost of instrumentation, necessity of trained technicians and immoderate operational cost are associated with them [18-21]. Currently, electroanalytical techniques which are fast, facile, selective, sensitive and cost effective are prevalent. Few attempts have been made in the past for SSZ determination by electroanalytical techniques, but the sensors utilized exhibited high limits of detection, narrow analytical range and low sensitivity [22-25]. Thus, in the current investigation a nano hybrid material of single walled carbon nanotubes (SWNTs) and Fe_3O_4 nanoparticles along with nafion have been exploited for the first time for SSZ determination. SWNT is one of the most propitious candidates for the modification of sensors due to its potential features such as high electrical conductivity, remarkable electron transport capacity, significantly large surface area and excellent mechanical strength [26-30]. Fe_3O_4 on the other hand, manifests strong adsorption ability, high abundance, low mass transfer resistance, biocompatibility, low toxicity and phenomenal magnetic and electrochemical properties [31-34]. The escalating utilization of metal nanoparticles along with carbon nanomaterial based electrochemical sensors has attracted cardinal attention due to their wide range of biomedical applications including magnetic resonance imaging, DNA separation, targeted drug delivery and various sensing platforms [35-38].

Herein, the synergetic features of SWNTs and Fe_3O_4 have been effectuated to form the nanocomposite with enriched properties. The developed nano hybrid material in which Fe_3O_4 acts as an ideal nano-carrier evinces large surface to volume ratio, enhanced electrical conductivity, lowest limit of detection, highest sensitivity and faster electron transfer kinetics. The pragmatic application of the developed sensor was corroborated by the assay of pharmaceutical formulations. The reliability was further comprehended by the selective detection of SSZ in real sample matrix of patient serum for the first time implementing square wave voltammetry (SWV). Augmentation in the quantitation of SSZ will commence the inception of improved drug combinations for RA.

2. Experimental

2.1 Chemicals and Reagents

Standard sulfasalazine sample, SWNTs (purity >99.5%) and nafion were procured from Sigma Aldrich and used as received. Ferrous sulfate heptahydrate ($FeSO_4 \cdot 7H_2O$), urea, glucose (GLU), paracetamol (PC), ferric chloride hexahydrate ($FeCl_3 \cdot 6H_2O$), potassium ferricyanide [$K_3Fe(CN)_6$] and NaOH flakes were obtained from S.D. Fine Chemical Ltd. (Mumbai, India). The NaH_2PO_4, Na_2HPO_4, uric acid (UA), xanthine (XN), ascorbic acid (AA), dopamine (DA) and ethanol were obtained from Merck company (Mumbai, India). 1 M phosphate buffer solution (PBS) with the pH of 7.2 was used as a supporting electrolyte for all voltammetric measurements. The SSZ containing tablets were purchased from a local pharmacy (Mumbai, India).

2.2 Instrumentation

High resolution - transmission electron microscopy (HR-TEM) images were acquired using a FEI, Tecnai G2, F30 transmission electron microscope at an accelerating voltage of 300 kV (Georgia, U.S.A). The field emission gun scanning electron microscopy (FEG-SEM) images and the energy dispersive X-ray (EDX) spectra were obtained from Tescan MIRA 3 model, Oxford instrument (Czech Republic, Europe). Voltammetric measurements were carried out using Metrohm system of Autolab (PGSTAT 302N) voltammetric analyzer and interface running on GPES 4.9 software. The electrochemical cell assembled was a glass cell containing a standard three-electrode system. The GCE (3.0 mm diameter) serving as a working substrate, a platinum wire as the auxiliary electrode and an Ag/AgCl (3.0 M KCl) used as the reference electrode. The potentials were recorded at an ambient temperature of 27 ± 2 ºC and detailed with respect to the reference electrode. The crystal structure of synthesized material was characterized using X-ray powder diffraction (XRD) instrument (6100, Shimadzu, India).

Fourier transform infrared (FT-IR) absorption spectra was obtained on Shimadzu-8400 instrument (India).

2.3 Procedure

The stock solution of SSZ was prepared by dissolving adequate quantity of the compound in few drops of 1 N NaOH to facilitate dissolution, then diluted with double distilled water up to the mark. The optimized experimental parameters employed for SWV were square wave frequency (*f*): 15 Hz, potential step (E): 4 mV, square wave amplitude (E$_{sw}$): 25 mV, initial E: 400 mV and final E: 1200 mV. The bubbling of high-purity nitrogen gas through test solutions were done for $10 - 15$ min to minimize the intervention of oxygen before recording cyclic voltammograms (CV). The patient serum sample and normal serum samples were obtained from J. J. Hospital, Mumbai, India. The blood samples were centrifuged following which the supernatant blood acquired was taken for the investigation of SSZ. Tablets were accurately weighed and crushed to a fine powder followed by dissolution in 1 N NaOH and dilution with double distilled water up to the mark.

2.4 Synthesis of Fe$_3$O$_4$ nanoparticles

For the preparation of Fe$_3$O$_4$ nanoparticles, FeCl$_3$·6H$_2$O (5.4 g) and urea (3.6 g) were initially dissolved in water (200 mL) followed by heating at 90ºC in inert conditions for 2 h under constant stirring. FeSO$_4$·7H$_2$O (2.8 g) was added to the resultant reaction mixture after cooling it to the room temperature. Finally, workup of reaction was carried out by dropwise addition of 0.1 N NaOH until pH 10 to obtain dark black colored solution. The resulting hydroxides were subjected to ultra-sonication in the sealed flask for 30 min. After ageing for 6 h, the precipitate was washed multiple times with double distilled water and collected using magnet subsequently followed by drying in oven at 80 ºC.

2.5 Fabrication of glassy carbon electrode

The modification of the bare electrode was effectuated only after the surface was cautiously polished with 0.3 micron alumina powder employing micro-cloth pads. Subsequently, it was washed extensively with double distilled water until a mirror like surface was attained. The sensor was fabricated by mixing 0.5 mg mL^{-1} suspension of SWNTs in N, N-dimethylformamide with 1 mg mL^{-1} of Fe_3O_4 nanoparticles homogenized in ethanol with 1% nafion. Followed by ultra-sonication of the dispersion for 30 min, a known volume (10 µL) was eventually dropped on the pretreated GCE surface and allowed to dry at room temperature. The electrode thus fabricated was denoted as Fe_3O_4/SWNTs/Naf/GCE and was ready for use.

3. Results and discussion

3.1 Characterization of Fe_3O_4

Fig. 1A illustrates the FT-IR spectrum of synthesized Fe_3O_4 nanoparticles. The peaks at 3400 and 1627 cm^{-1}, are allocated to symmetrical and asymmetrical modes of –OH bonds attached to the surface iron atoms. While the significant absorption peak at 579 cm^{-1} is ascribed to the stretching vibration mode of Fe–O bond in bulk Fe_3O_4 sample [39]. The crystal structure of synthesized Fe_3O_4 powder was characterized by XRD pattern demonstrated in Fig. 1B. It shows diffraction peaks at 2θ values of 30.31, 35.67, 43.34, 53.68, 57.22 and 62.85, which have been indexed with (220), (311), (400), (422), (511) and (440) crystal planes of Fe_3O_4. The analyzed diffraction peaks were matched well with the standard XRD pattern (JCPDS No. 65-3107) which declared the crystallographic structure of Fe_3O_4 [40]. Furthermore, no additional phases or Fe_2O_3 were found, suggesting the high purity of the sample with a spinel structure.

3.2 Characterization of developed sensor

The surface morphology of Fe_3O_4/SWNTs/Naf/GCE was characterized by FEG-SEM image as depicted in Fig. 2A. It vividly indicates that the nanosized Fe_3O_4 are well dispersed and surrounded by SWNTs and nafion composite, which enhances facile charge transfer. The EDX spectrum demonstrated in Fig. 2B represents peaks for the presence of Fe, C, and O which

manifests the successful loading of Fe_3O_4 on SWNTs. The TEM image (Fig. 2C), revealed the well-dispersed Fe_3O_4 nanoparticles having average diameter of 30 nm with uniform distribution on the SWNTs surface. The HR-TEM image displays uniform lattice fringes across the entire Fe_3O_4 single crystal as showcased in Fig. 2D. The selected area electron diffraction (SAED) pattern presented in Fig. 2E was in good agreement with XRD analysis which validate the purity of the material. These results patently demonstrated that Fe_3O_4 and SWNTs were effectively and uniformly fabricated on the bare GCE.
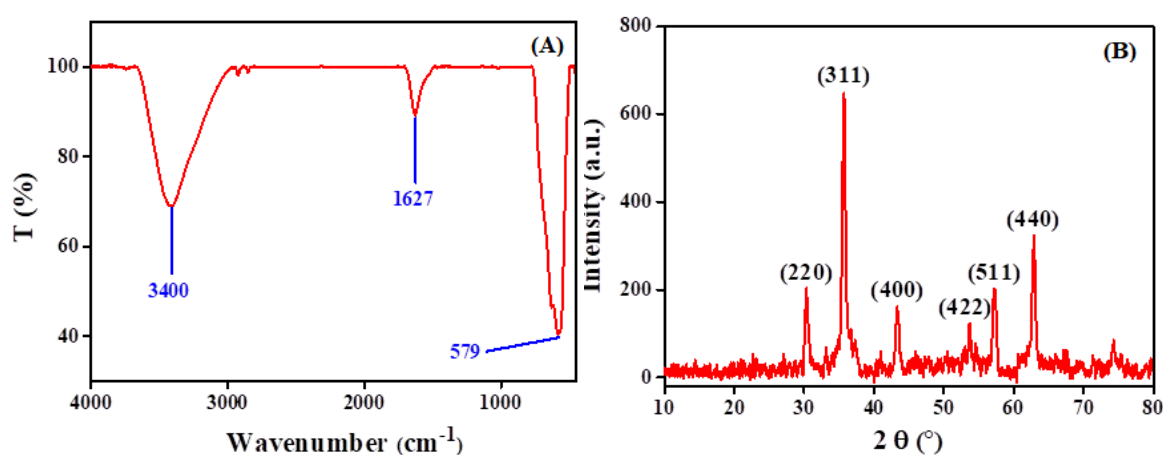
Fig. 1 (A) FT-IR spectrum and **(B)** XRD patterns of Fe_3O_4 nanoparticles.

3.3 Determination of electroactive surface area

The electroactive surface area of the bare GCE and Fe_3O_4/SWNTs/Naf/GCE was determined by utilizing chronocoulometry technique for which 5 mM $K_3Fe(CN)_6$ solution in 0.1 M KCl as a supporting electrolyte was utilized. The integrated Cottrell equation was applied:

$$Q = 2nFAcD^{1/2} t^{1/2} \pi^{-1/2} + Q_{dl} + nFA\Gamma_0$$

where n is the number of electrons transferred (n = 1), A is the electroactive surface area of the sensor in cm^2 and F is the Faraday constant D is the diffusion coefficient of $K_3Fe(CN)_6$ solution (7.6×10^{-6} cm^2s^{-1}); c is the substrate concentration (M), Q_{dl} is the

capacitive charge and $nFA\Gamma_0$ is the charge from the reduction of adsorbed species. The electroactive surface area of bare GCE and Fe_3O_4/SWNTs/Naf/GCE was estimated by using the slope value of Q versus $t^{1/2}$ linear plot. The linear relationship between Q and $t^{1/2}$ obtained from two different chronocoulograms, exhibited slope of 30 $\mu C\ s^{-1/2}$ and 273.6 $\mu C\ s^{-1/2}$ corresponding to bare and modified GCE respectively. The comparison of electroactive surface area at bare (0.020 cm^2) and modified GCE (0.182 cm^2) revealed that the functional working area of the Fe_3O_4/SWNTs/Naf modified GCE is 9.1 times greater than that of the bare GCE. Thus, the substantial upsurge in the electroactive surface area leads to an augmentation in the electrochemical active sites at bare GCE.
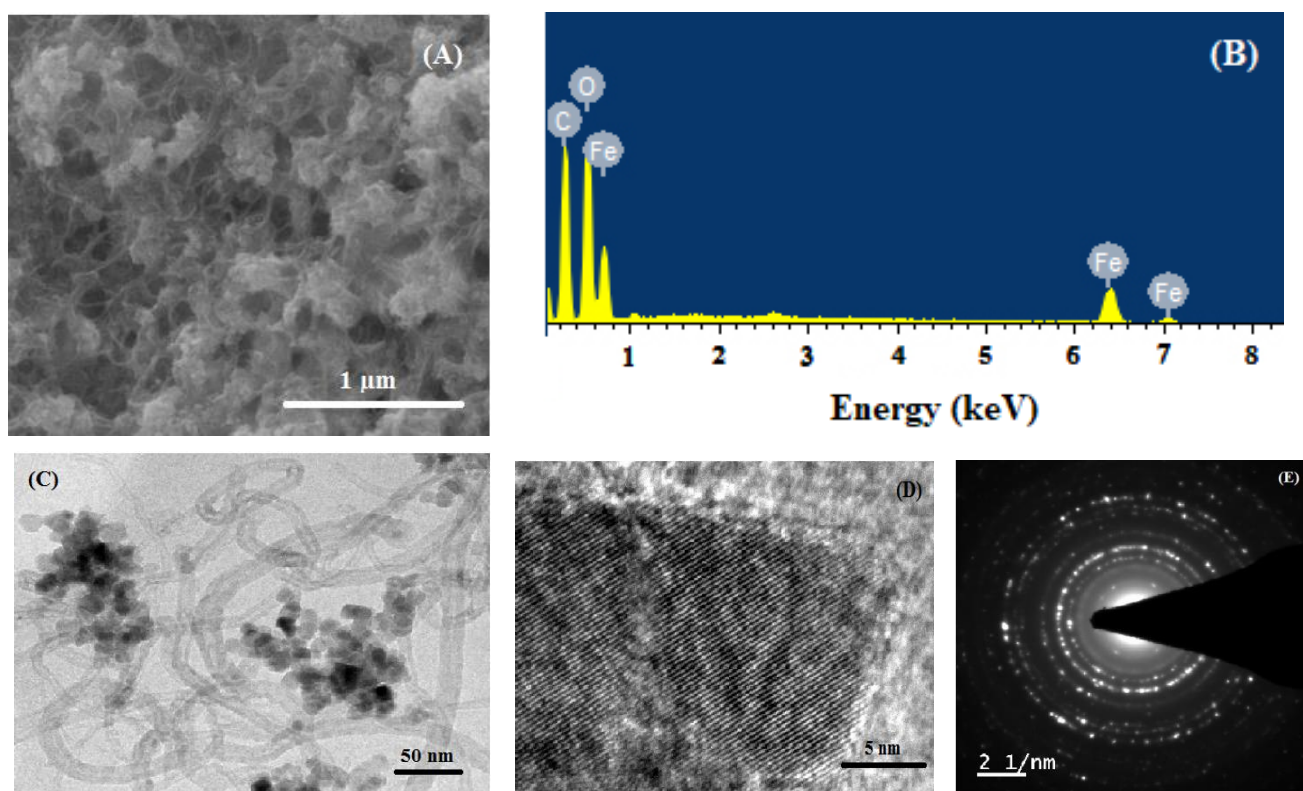
Fig. 2 (A) FEG-SEM image **(B)** EDX spectrum **(C)** TEM image **(D)** HR-TEM image and **(E)** SAED pattern of Fe_3O_4/SWNTs/Naf composite.

3.4 Electrochemical characterization

In electrochemical impedance spectroscopy (EIS) the $[Fe(CN)_6]^{-3/-4}$ system has been used as a redox probe which provided valuable information about the electrode – electrolyte

interface properties during the modification process. In a typical Nyquist plot, the semicircle diameter corresponds to the electron transfer resistance, and the linear segment represents the diffusion-limited process. Fig. 3A illustrates Nyquist plots for bare GCE, Fe_3O_4/GCE, SWNTs/GCE and Fe_3O_4/SWNTs/Naf/GCE in 5 mM $[Fe(CN)_6]^{-3/-4}$ containing 0.1 M KCl. A semicircle with considerable diameter was noticed for bare GCE thereby implying poor interfacial electron transfer. The modification of GCE with Fe_3O_4 and SWNTs respectively revealed the reduction in the diameter of semicircle indicating an enhancement in the rate of electron transfer of $[Fe(CN)_6]^{-3/-4}$. While smallest semicircle diameter was observed for the developed sensor due to the highest conductivity. The EIS results clearly imply that the synergistic effect of SWNTs and Fe_3O_4 significantly increased the electron transfer rate consequently escalating the conductivity of Fe_3O_4/SWNTs/Naf/GCE.

3.5 Electro-oxidation of sulfasalazine

3.5.1 Cyclic voltammetry

The voltammetric response of 500 nM SSZ at bare GCE and Fe_3O_4/SWNTs/Naf/GCE was investigated by utilizing cyclic voltammetry. Fig. 3B exhibits the CVs of SSZ recorded at scan rate of 25 mV s^{-1} depicting an irreversible oxidation peak at bare and modified GCE. An inconspicuous peak was noted at the bare electrode at ~1081 mV while the oxidation peak distinctly shifted to ~978 mV with ~7.6 times amelioration in peak current at Fe_3O_4/SWNTs/Naf/GCE. The notable shift in the oxidation peak potential along with escalation in peak current evidently indicates that Fe_3O_4/SWNTs/Naf/GCE provides a large surface area for the interaction of SSZ. A feasible electrochemical reaction mechanism of SSZ is represented in Scheme 1 wherein SSZ gives rise to phenoxy radical which eventually reacts with water molecule in an irreversible manner to produce a diketo product.
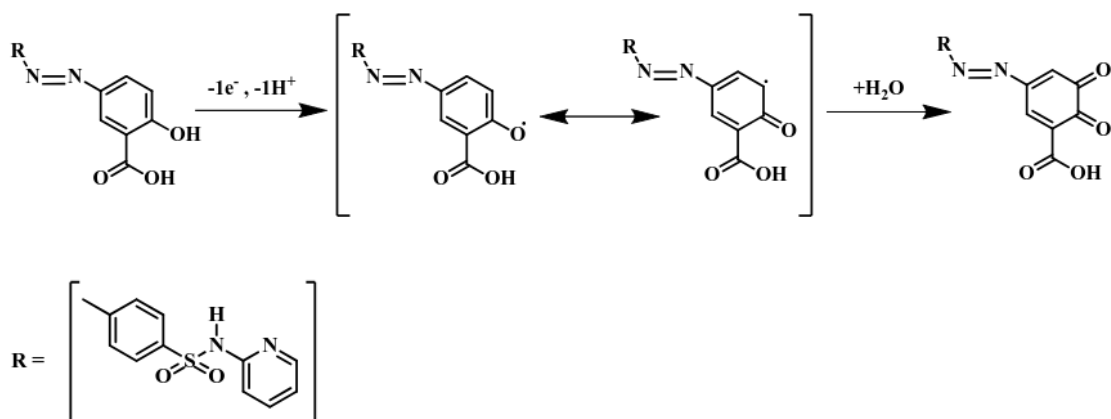
Scheme 1: Electrochemical reaction mechanism of sulfasalazine.

3.5.2 Square wave voltammetry

The advance SWV technique was executed for further quantification of SSZ, as it possesses numerous advantages including selectivity, sensitivity with low background current in comparison to CV. The SWVs recorded for 500 nM SSZ at four varied working sensors in 1 M PBS at pH 7.2 is showcased in Fig. 3C. The electrochemical response for bare GCE and Fe_3O_4/GCE gives oxidation peak at ~1052 and ~1034 mV respectively. At SWNTs/GCE, SSZ oxidized at ~998 mV with rise in the peak current. The peak potential at Fe_3O_4/SWNTs/Naf/GCE corresponding to ~945 mV along with noteworthy increment in the peak current in comparison to the rest of the sensors indicated highest sensitive response. The voltammetric current response at Fe_3O_4/SWNTs/Naf/GCE is ~7.5 and ~2.8 times higher in comparison to the bare GCE and SWNTs/GCE respectively. The results signify the supremacy of the developed sensor over the other working electrodes for electro oxidation of SSZ.

3.6 Optimization of experimental variables

3.6.1 Effect of pH

A noteworthy effect on the peak potential and peak current has been perceived with the change in pH. Therefore, optimization of pH is one of the crucial parameters in the

investigation of SSZ which was effectuated at Fe_3O_4/SWNTs/Naf/GCE employing SWV. The influence of pH ranging from 2.0 to 11.0 was investigated for the electrochemical response of 500 nM SSZ at a f of 15 Hz. It demonstrated that with an increment in the pH the peak potential of the analyte shifted to less positive values. The E_p versus pH plot was found to be linear and is depicted as:

$$E_p \text{ (pH 2.0 – 11.0)} = [1318.10 – 53.84 \text{ pH}] \text{ mV versus Ag/AgCl}$$

with correlation coefficient of 0.9951 with a corresponding slope of 53.84 mV pH^{-1}. Since the value of slope is within close range to the Nernstian equation thereby indicating that the electrochemical oxidation involves same number of electrons and protons. The influence of pH on the oxidative peak current of the compound was also analyzed. pH 7.2 was used as the supporting electrolyte for further analysis because it exhibited the maximum peak current response.
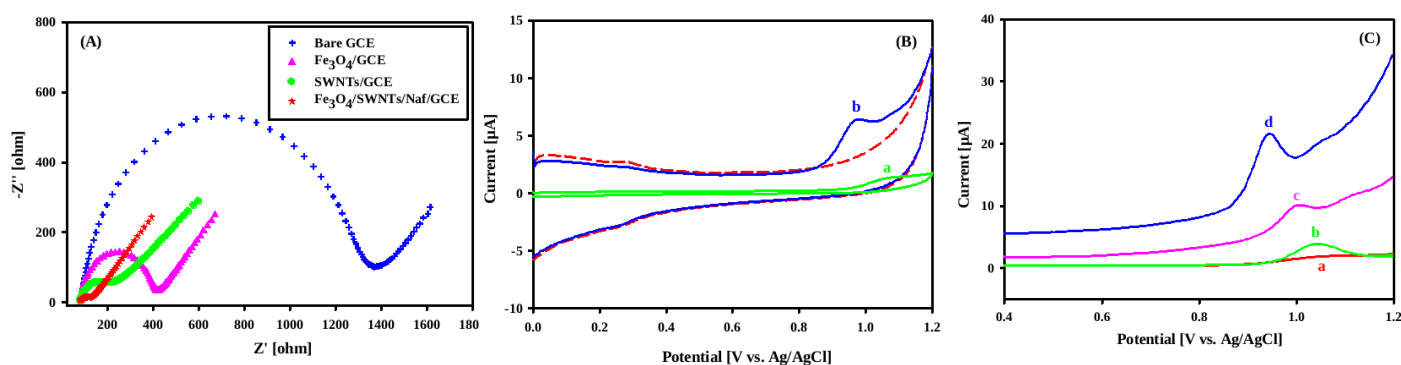
Fig. 3 (A) Nyquist plots of different electrodes in 5 mM $[Fe(CN)_6]^{-3/-4}$ solution containing 0.1 M KCl. **(B)** CVs obtained for 500 nM SSZ in PBS of pH 7.2 at (a) bare GCE and (b) Fe_3O_4/SWNTs/Naf/GCE at 25 mVs^{-1}. Voltammetric response recorded for PBS (background) at Fe_3O_4/SWNTs/Naf/GCE (- - -). **(C)** SWVs obtained for 500 nM SSZ in PBS of pH 7.2 at (a) bare GCE, (b) Fe_3O_4/GCE, (c) SWNTs/GCE and (d) Fe_3O_4/SWNTs/Naf/GCE at 15 Hz.

3.6.2 Influence of square wave frequency

The consequence of square wave frequency in the range of 10 – 100 Hz was investigated on the electrochemical response of SSZ. The values of oxidative peak current enhance linearly with an increment in f and the dependence between i_p and f can be represented by the equation:

$$i_p \ (\mu A) = 0.3989 \, f + 3.46$$

having a correlation coefficient of 0.9992. The peak potential of SSZ was observed to be shifted towards higher values with an increment in f at the fabricated sensor. The linear plot of E_p versus log f can be expressed as:

$$E_p \ (mV) = 117.73 \log f + 810.58$$

with a correlation coefficient of 0.9937. This electrochemical behavior of SSZ infers that the oxidation reaction is irreversible in nature with adsorption properties.

3.7 Concentration study

Under the optimal conditions, the electrochemical performance of the Fe_3O_4/SWNTs/Naf/GCE was studied for the determination of SSZ at pH 7.2. The oxidation peak current response of SSZ increased conspicuously with an augmentation in the concentration. The current values were obtained by subtracting the background current and are reported as an average of at least three replicate determinations with a standard deviation of less than 3.9% for n = 3. A linearity in the working concentration range of 25 – 1500 nM is depicted in Fig. 4 and the regression equation is as follows:

$$i_p \ (\mu A) = 0.0186 \ C \ (nM) + 0.8576$$

having a correlation coefficient of 0.9960. The efficacy of the proposed method can be assessed by two significant parameters which are detection limit and sensitivity. In the present investigation, the limit of detection was estimated to be 1.6 nM with the highest sensitivity of

18.6 µA µM^{-1}. Hence, the fabricated sensor corroborates remarkable electrocatalytic activity, providing a suitable platform for the determination of SSZ.
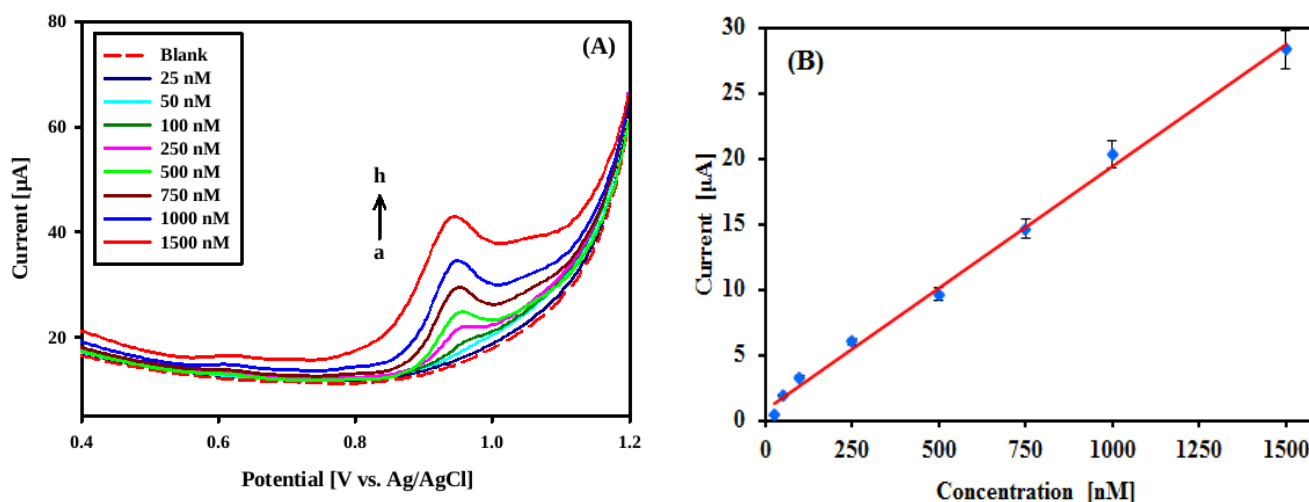
Fig. 4 (A) SWVs recorded for (i) PBS (background) (- - -) and (ii) increasing concentration of SSZ (—) at Fe$_3$O$_4$/SWNTs/Naf/GCE. [Curves were recorded at (a) 25, (b) 50, (c) 100, (d) 250, (e) 500, (f) 750, (g) 1000 and (h) 1500 nM concentration in PBS of pH 7.2] **(B)** Corresponding linear calibration plot.

3.8 Selectivity

Selectivity is another pivotal factor for a sensor, which was examined for the determination of 500 nM SSZ under optimized conditions as described above. A variety of interferents which coexist with SSZ in real samples such as glucose, ascorbic acid, paracetamol, uric acid, xanthine and dopamine were analyzed. The investigations distinctly reveal that even 100-fold concentration of the interfering species did not affect the quantitation of SSZ at Fe$_3$O$_4$/SWNTs/Naf/GCE. The peak current value of SSZ was minimally altered after the spiking of the interferents. Tolerance limit refers to the maximum content of the interfering species which can cause a relative error less than ±5% in the detection of SSZ. The investigation showcased that the developed sensor favorably attributed to the high selective recognition of SSZ in biological matrix.

3.9 Stability and reproducibility

The reliability of the developed sensor was endorsed by assessing the stability and reproducibility at optimized conditions. The prolonged stability was evaluated by assessing the peak current response of 500 nM SSZ at Fe_3O_4/SWNTs/Naf/GCE over the period of 30 days. The peak current response for the first day was considered as 100% and after a period of 30 days, there was a retention of 96.88% of voltammetric current response thereby suggesting notable longevity of the developed electrode. The reproducibility of Fe_3O_4/SWNTs/Naf/GCE was corroborated by analyzing the same concentration of SSZ at six different sensors with similar modification. The relative standard deviation (RSD) was acquired to be 1.06% for 500 nM SSZ that certifies the analytical reproducibility of the sensor. The intra-day current response at Fe_3O_4/SWNTs/Naf/GCE was assessed by recording seven consecutive scans with an unchanged concentration of 500 nM SSZ. The RSD value was estimated to be 1.88% manifesting acceptable reproducibility of the sensor. Furthermore, the day-to-day precision of the sensor was investigated for seven consecutive days utilizing 500 nM SSZ which indicated a RSD value of 1.67%. Thus, the Fe_3O_4/SWNTs/Naf/GCE proclaims distinctive stability and adequate reproducibility for the electro oxidation of SSZ.

3.10 Pharmaceutical analysis

The performance of the fabricated sensor was explored for the determination of SSZ in commercial tablets which substantiates the applicability of the sensor as a potential diagnostic tool. The tablets namely, Sazo, Saaz, and Salazar were weighed and crush into fine powder. The stock solution was thereafter prepared by dissolving an apt amount of the respective tablet in 0.1 M NaOH followed by filtration and dilution up to the mark. Finally, the voltammograms were recorded at optimized conditions by taking suitable aliquots and diluting with buffer of pH 7.2. The content of SSZ in the pharmaceutical formulations was accurately assessed via calibration equation. The amount of SSZ found in the tablets through the proposed method

showed variance of not more than 3.7% of RSD for n=3. Table 1 summarizes the obtained results which were found to be in good agreement with the claimed content having relative error less than 5% for all commercial samples. Hence, it vividly reveals that the crafted sensor possesses remarkable recognition selectivity for the sensing of SSZ in pharmaceutical formulations without interference of the drug excipients.

Table 1 Determination of SSZ in pharmaceutical preparations using Fe_3O_4/SWNTs/Naf/GCE.

Sample	Stated content	Detected content	Error (%)
Sazo	500 mg	484.0 mg	- 3.20
Saaz	500 mg	512.5 mg	2.50
Salazar	500 mg	488.4 mg	- 2.32

3.11 Real sample assay

To demonstrate the viability of the developed method in complex biological systems, the detection of SSZ in normal human serum and patient human serum samples was analyzed for the first time at Fe_3O_4/SWNTs/Naf/GCE in physiological pH 7.2. Initially, the serum samples were diluted 50 times with pH 7.2 to reduce the effect of matrix. The recovery studies in the normal human serum samples displayed the absence of oxidation peak of SSZ before the spiking of the analyte as demonstrated in Fig. 5A (curve a). Thereafter, voltammograms were obtained with standard addition of SSZ with known concentrations such as 100, 300 and 600 nM as showcased in Fig. 5A (curves b, c and d). The recoveries exhibited a range of 96.36% to 103.81% in normal human serum samples as showcased in Table 2 thereby indicating satisfactory practicality of the proposed method.

The serum samples of patient after 6h of administration of Salazar containing 500 mg of SSZ were investigated. The voltammogram of patient samples in this case demonstrated a clearly marked oxidation peak of SSZ at ~945 mV before spiking as displayed in Fig. 5B (curve a). To confirm the oxidation of SSZ, known concentrations of 100 and 200 nM were spiked which reflected an increase in the peak current at the identical oxidation potential as illustrated in Fig. 5B (curves b and c). The SSZ concentration before and after spiking was calculated using regression equation and represented in Table 2. The promising results affirm that the developed sensing system can be employed for the preliminary detection of SSZ in clinical diagnosis.
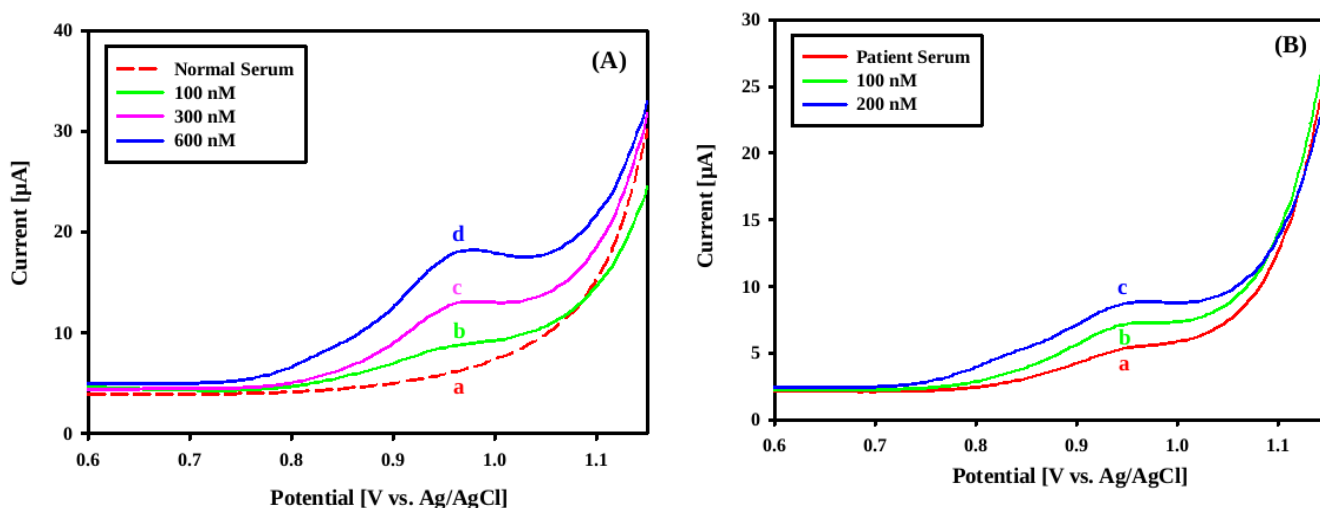
Fig. 5 Voltammograms recorded at Fe_3O_4/SWNTs/Naf/GCE for **(A)** normal human serum sample 1 and **(B)** patient serum sample 1 before and after spiking different concentrations of SSZ.

Table 2 Concentration of SSZ in normal human and patient human serum samples at Fe_3O_4/SWNTs/Naf/GCE at pH 7.2.

	Spiked (nM)	Detected (nM)	Recovery (%)
Normal Human Serum			
Sample 1	0.0	-------	-------
	100.0	96.36	96.36

	300.0	311.42	103.81
	600.0	585.61	97.60
Sample 2	0.0	-------	-------
	100.0	101.20	101.20
	300.0	294.80	98.27
	600.0	595.80	99.30
Patient Human Serum			
Sample 1	0.0	89.38	-------
	100.0	186.15	98.29
	200.0	276.47	95.54
Sample 2	0.0	90.40	-------
	100.0	190.15	99.87
	200.0	280.50	96.59

The RSD value for determination was less than 3.4% for n=3

4. Conclusions

The present investigation utilizing the synergism of SWNTs and Fe_3O_4 nanoparticles as a sensing platform accorded new feasibility for the electro-oxidative study of SSZ. Due to enhanced electrical conductivity, remarkable electron transfer capacity, immense electroactive surface area and strong adsorption ability, the Fe_3O_4/SWNTs/Naf/GCE exhibited extensive electrocatalytic activity towards SSZ oxidation. Under optimized conditions, a dynamic linear correlation was acquired between the concentration of SSZ and its peak current response within the calibration range of 25 – 1500 nM at the developed sensor manifesting the lowest limit of detection (1.6 nM) and highest sensitivity (18.6 $\mu A\ \mu M^{-1}$) reported so far by electrochemical determination of SSZ. The developed prototype was distinctly selective for the targeted compound in the presence of frequently existing biological analytes. The fabricated sensor was furthermore endorsed by the quantitative determination of SSZ in varied pharmaceutical formulations thereby augmenting its pragmatic application. The noteworthy utilitarian segment

of Fe_3O_4/SWNTs/Naf/GCE is the adequate detection of SSZ for the first time in rheumatoid arthritis patient serum sample. This article corroborates that the expeditious results described herein will instigate realistic application of the crafted sensor as a robust diagnostic tool for *in vivo* analysis.

Acknowledgements

References

[1] S. Jayashree, K. Nirekshana, G. Guha, D. Bhakta Guha, Cancer chemotherapeutics in rheumatoid arthritis: A convoluted connection, Biomed. Pharmacother. 102 (2018) 894.

[2] S. Won, S. K. Cho, D. Kim, M. Han, J. Lee, E. J. Jang, Y. K. Sung, S. C. Bae, Update on the prevalence and incidence of rheumatoid arthritis in Korea and an analysis of medical care and drug utilization, Rheumatol. Int. 38 (2018) 649.

[3] A. D. Woolf, B. Pfleger, Burden of major musculoskeletal conditions, Bull. World Health Organ. 81 (2003) 646.

[4] Q. Yao, B. Shen, A systematic analysis of treatment and outcomes of NOD_2-associated autoinflammatory disease, Am. J. Med. 130 (2017) 365.

[5] B. Nigovic, B. Simunic, S. Hocevar, Voltammetric measurements of aminosalicylate drugs using bismuth film electrode, Electrochim. Acta 54 (2009) 5678.

[6] M. Kandula, K. Sunil Kumar, S. Palanichamy, A. Rampal, Discovery and preclinical development of a novel prodrug conjugate of mesalamine with eicosapentaenoic acid and caprylic acid for the treatment of inflammatory bowel diseases, Int. Immunopharmacol. 40 (2016) 443.

[7] S. Sadeghi, A. Motaharian, A. Z. Moghaddam, Electroanalytical determination of sulfasalazine in pharmaceutical and biological samples using molecularly imprinted polymer modified carbon paste electrode, Sens. Actuat. Chem. B 168 (2012) 336

[8] S. Sadeghi, A. Garmroodi, Sensitive detection of sulfasalazine at screen printed carbon electrode modified with functionalized multiwalled carbon nanotubes, J. Electroanal. Chem. 727 (2014) 171.

[9] A. Khataee, S. Arefi Oskoui, M. Fathinia, A. Fazli, A. Shahedi Hojaghan, Y. Hanifehpour, S. W. Joo, Photocatalysis of sulfasalazine using Gd-doped PbSe nanoparticles under visible light irradiation: kinetics, intermediate identification and phyto-toxicological studies, J. Ind. Eng. Chem. 30 (2015) 134.

[10] M. Z. Ma, G. Chen, P. Wang, W. H. Lu, C. F. Zhu, M. Song, J. Yang, S. Wen, R. H. Xu, Y. Hu, P. Huang, Xc− Inhibitor sulfasalazine sensitizes colorectal cancer to cisplatin by a GSH-dependent mechanism, Cancer Lett. 368 (2015) 88.

[11] K. Shitara, T. Doi, O. Nagano, C. K. Imamura, T. Ozeki, Y. Ishii, K. Tsuchihashi, S. Takahashi, T. E. Nakajima, S. Hironaka, M. Fukutani, H. Hasegawa, S. Nomura, A. Sato, Y. Einaga, T. Kuwata, H. Saya, A, Ohtsu, Dose-escalation study for the targeting of CD44v$^+$ cancer stem cells by sulfasalazine in patients with advanced gastric cancer (EPOC1205), Gastric Cancer 20 (2017) 341.

[12] B. Nigovic, S. Komorsky Lovric, B. Simunic, Electroanalytical studies of biologically active azosalicylic acid at a hanging mercury drop electrode, Electroanalysis 17 (2005) 839.

[13] B. M. Peskar, K. W. Dreyling, B. May, K. Schaarschmidt, H. Goebell, Possible mode of action of 5-aminosalicylic acid, Dig. Dis. Sci. 32 (1987) 51.

[14] N. Pastor Navarro, E. Gallego Iglesias, A. Maquieira, R. Puchades, Immunochemical method for sulfasalazine determination in human plasma, Anal. Chim. Acta 583 (2007) 377.

[15] B. Nigovic, S. Juric, I. Mitrovic, Bismuth nanoparticles-carbon nanotubes modified sensor for sulfasalazine analysis, Talanta 164 (2017) 201.

[16] M. J. Cosentino, W. Y. Chey, H. Takihara, A. T. K. Cockett, The effects of sulfasalazine on human male fertility potential and seminal prostaglandins, J. Urol. 132 (1984) 682.

[17] R. A. Levy, G. R. de Jesus, N. R. de Jesus, E. M. Klumb, Critical review of the current recommendations for the treatment of systemic inflammatory rheumatic diseases during pregnancy and lactation, Autoimmun. Rev. 15 (2016) 955.

[18] G. Z. Gu, H. M. Xia, Z. Q. Pang, Z. Y. Liu, X. G. Jiang, J. Chen, Determination of sulphasalazine and its main metabolite sulphapyridine and 5-aminosalicylic acid in human plasma by liquid chromatography/tandem mass spectrometry and its application to a pharmacokinetic study, J. Chromatogr. B 879 (2011) 449.

[19] G. Palumbo, G. Carlucci, P. Mazzeo, G. Frieri, M. T. Pimpo, D. Fanini, Simultaneous determination of 5-aminosalicylic acid, acetyl-5-aminosalicylic acid and 2, 5-dihydroxybenzoic acid in endoscopic intestinal biopsy samples in humans by high-performance liquid chromatography with electrochemical detection, J. Pharm. Biomed. Anal. 14 (1995) 175.

[20] M. S. Elmasry, I. S. Blagbrough, M. G. Rowan, H. M. Saleh, A. A. Kheir, P. J. Rogers, Quantitative HPLC analysis of mebeverine, mesalazine, sulphasalazine and dispersible aspirin stored in a venalink monitored dosage system with co-prescribed medicines, J. Pharm. Biomed. Anal. 54 (2011) 646.

[21] G. Font, A. Juan Garcia, Y. Pico, Pressurized liquid extraction combined with capillary electrophoresis–mass spectrometry as an improved methodology for the determination of sulfonamide residues in meat, J. Chromatogr. A 1159 (2007) 233.

[22] R. M. Buoro, V. C. Diculescu, I. C. Lopes, S. H. P. Serrano, A. M. Oliveira Brett, Electrochemical oxidation of sulfasalazine at a glassy carbon electrode, Electroanalysis 26 (2014) 924.

[23] T. A. M. Msagati, J. C. Ngila, Voltammetric detection of sulfonamides at a poly (3-methylthiophene) electrode, Talanta 58 (2002) 605.

[24] H. Beitollahi, R. Yoonesfar, Sensitive detection of sulfasalazine at a carbon paste electrode modified with NiO/CNT nanocomposite and ionic liquid in pharmaceutical and biological samples, Inorg. Nano Met. Chem. 47 (2017) 1441.

[25] Z. Amani Beni, A. Nezamzadeh Ejhieh, NiO nanoparticles modified carbon pate electrode as a novel sulfasalazine sensor, Anal. Chim. Acta 1031 (2018) 47.

[26] A. P. Tsapenko, A. E. Goldt, E. Shulga, Z. I. Popov, K. I. Maslakov, A. S. Anisimov, P. B. Sorokin, A. G. Nasibulin, Highly conductive and transparent films of $HAuCl_4$ doped single-walled carbon nanotubes for flexible applications, Carbon 130 (2018) 448.

[27] S. Mane, R. Narmawala, S. Chatterjee, Selective recognition of atropine in biological fluids and leaves of *Datura stramonium* employing a carbon nanotube-chitosan film based biosensor, New J. Chem. 42 (2018) 10852.

[28] A. P. Lima, A. C. Catto, E. Longo, E. Nossol, E. M. Richter, R. A. A. Munoz, Investigation on acid functionalization of double-walled carbon nanotubes of different lengths on the development of amperometric sensors, Electrochim. Acta 299 (2019) 762.

[29] R. Savalia, S. Chatterjee, Sensitive detection of brucine an anti-metastatic drug for hepatocellular carcinoma at carbon nanotubes – nafion composite based biosensor, Biosens. Bioelectron. 98 (2017) 371.

[30] R. N. Goyal, S. Chatterjee, A. R. S. Rana, A single-wall carbon nanotubes modified edge plane pyrolytic graphite sensor for determination of methylprednisolone in biological fluids, Talanta 80 (2009) 586.

[31] J. Yao, K. Zhang, W. Wang, X. Zuo, Q. Yang, M. Wu, G. Li, Great enhancement of electrochemical cyclic voltammetry stabilization of Fe_3O_4 microspheres by introducing 3DRGO, Electrochim. Acta 279 (2018) 168.

[32] C. He, M. Xie, F. Hong, X. Chai, H. Mi, X. Zhou, L. Fan, Q. Zhang, T. Ngai, J. Liu, A highly sensitive glucose biosensor based on gold nanoparticles/bovine serum albumin/Fe_3O_4 biocomposite nanoparticles, Electrochim. Acta 222 (2016) 1709.

[33] D. Cabrera, A. Coene, J. Leliaert, E. J. Artes Ibariez, L. Dupre, N. D. Telling, F. J. Teran, Dynamical magnetic response of iron oxide nanoparticles inside live cells, ACS Nano 12 (2018) 2741.

[34] S. Venkateswarlu, D. Lee, M. Yoon, Bioinspired 2D-carbon flakes and FeO nanoparticles composite for arsenite removal, ACS Appl. Mater. Interfaces 8 (2016) 23876.

[35] Y. Hu, S. Mignani, J. P. Majoral, M. Shen, X. Shi, Construction of iron oxide nanoparticle-based hybrid platforms for tumor imaging and therapy, Chem. Soc. Rev. 47 (2018) 1874.

[36] Y. Cheng, Y. Liu, J. Huang, K. Li, Y. Xian, W. Zhang, L. Jin, Amperometric tyrosinase biosensor based on Fe_3O_4 nanoparticles-coated carbon nanotubes nanocomposite for rapid detection of coliforms, Electrochim. Acta 54 (2009) 2588.

[37] A. Chen, S. Chatterjee, Nanomaterials based electrochemical sensors for biomedical applications, Chem. Soc. Rev. 42 (2013) 5425.

[38] L. Yang, X. Ren, F. Tang, L. Zhang, A practical glucose biosensor based on Fe_3O_4 nanoparticles and chitosan/nafion composite film, Biosens. Bioelectron. 25 (2009) 889.

[39] H. Keypour, S. G. Saremi, H. Veisi, M. Noroozi, Electrochemical determination of citalopram on new Schiff base functionalized magnetic Fe_3O_4 nanoparticle/MWCNTs modified glassy carbon electrode, J. Electroanal. Chem. 780 (2016) 160.

[40] F. A. N. Xiu-juan, L. I. Xin, Preparation and magnetic property of multiwalled carbon nanotubes decorated by Fe_3O_4 nanoparticles, New Carbon Mater. 27 (2012) 111.

Article-5

Performance evaluation of photoanodes used for PEC water splitting: Discussion on a few techniques and their applications

Sudipa Manna[1,2], and A.K.Satpati[1, 2*]

[1]Analytical Chemistry Division, Bhabha Atomic Research Centre, Mumbai-400085, India

[2]Homi Bhabha National Institute, Anushaktinagar, Mumbai 400094, India

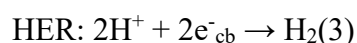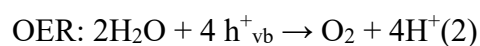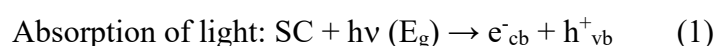*Corresponding author: (A. K. Satpati) email: asatpati@barc.gov.in

Abstract

The article has placed a short review on the photoelectrochemical splitting of water describing the techniques involved in the evaluation of the efficiency in the catalysis process. The energy states of the interface play important role in determining the performance of the catalysts, electrochemical and Spectro-electrochemical techniques are well suited in the evaluation of kinetics and thermodynamics of the interfaces during PEC processes. In addition to discuss some pf the basic techniques, present article described the intensity modulated photocurrent spectroscopy (IMPS) and intensity modulated photo voltage spectroscopy (IMVS). These two techniques are applied to bismuth vanadate and hematite photoanodes in evaluating the OER photoelectrochemical kinetics. The modulation of charge recombination and charge transfer processes through the modification in the PEC catalysts in overall enhancement of the OER efficiency have been presented.

1. Introduction:

With the current development targets by various countries the global energy demand is projected to rise by 11-18% over the present requirements by 2050. Global temperature rise will break the ceiling the 1.5 while the carbon dioxide emission will be 18 giga tons even if the countries meet their respective targets. To address this global issue, techniques have to evolve for green energy production. In this regard, H_2 emerges as the strongest contender due to its high energy density of 141.9MJ kg $^{-1}$, zero carbon emission during combustion, ease of transport & storage, on-site utilization and integration with presently available technologies. In the recent years among many technologies photoelectrochemical (PEC) water splitting has evolved as a very promising technology for H_2 generation due to lower energy consumption, spatial deconvolution of cathodic and anodic processes, flexibility of electrode design in terms of band gap and band edge positions, allowing utilization of semiconductor with band gap in the visible spectrum etc. In spite of the edges over other available technologies, being quite recent technique, it is still in nascent stage and has not matured as an industrial technology. Hence, proper understanding of the fundamentals of water splitting, performance evaluation of the photoelectrodes along with molecular mechanism of the process and fine tuning the parameters to optimize the performance are the need of present time.

The mechanism of photocatalytic water splitting over semiconductor (SC) electrode is as follows:

Absorption of light: $SC + h\nu\ (E_g) \rightarrow e^-_{cb} + h^+_{vb}$ (1)

OER: $2H_2O + 4\ h^+_{vb} \rightarrow O_2 + 4H^+$(2)

HER: $2H^+ + 2e^-_{cb} \rightarrow H_2$(3)

Thus, the overall water splitting reaction: $2H_2O \rightarrow 2\ H_2 + O_2$ $\Delta G = 237.2$ kJ mol^{-1} (4)

The energetics of different steps of the water splitting process has been indicated in Scheme 1
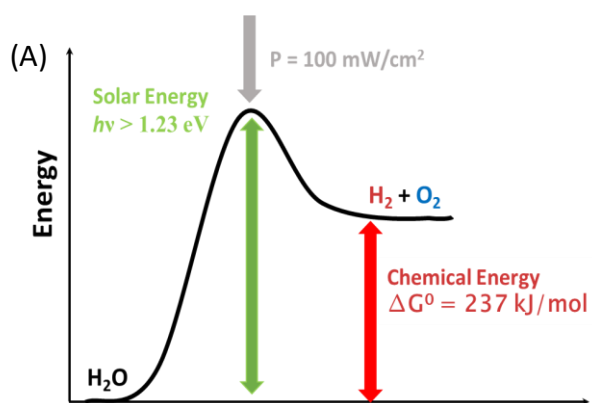
Scheme 1 (A) The energy level diagram depicting the energy requirements of water splitting process

Light absorbed by a semiconductor (SC) generates electron-hole pairs, which facilitate the redox reactions necessary to convert water into hydrogen and oxygen at their respective surface sites. The feasibility of these reactions depends on the energy levels of the electrons and holes created in the SC upon photon absorption. Consequently, the catalyst must possess an appropriate band gap (Eg > 1.23 eV) and valence band edges that align with the potentials for hydrogen evolution reaction (HER) and oxygen evolution reaction (OER).

Photocatalysis offers the advantage of directly utilizing solar energy without relying on other energy sources. However, only a few catalysts meet the stringent requirements for band gap and band alignment. Finding catalysts made from low-cost, earth-abundant elements with a high absorption coefficient in the visible spectrum is even more challenging. Moreover, since electrons and holes are generated in the conduction band (CB) and valence band (VB) of the same material, the high likelihood of recombination limits efficiency.

In the case of photoelectrochemical (PEC) processes, solar light serves as the primary energy source, supplemented by a small electrical potential to enhance the efficient separation of electron-hole pairs. This application of a low bias potential is a key distinction between photocatalysis and photoelectrocatalysis. In PEC, water oxidation and reduction occur at separate electrodes—photoanode and photocathode, respectively—decoupling the processes spatially within the PEC cell. This enables the use of different catalyst materials for the fabrication of each electrode.

The PEC approach offers significant advantages, such as relaxing the stringent requirements for both large band gaps and precise band edge positions. Photoanodes require a valence band

maximum more positive than the O_2/H_2O potential (1.23 V on the NHE scale), while photocathodes need a conduction band minimum more negative than the H_2O/H_2 potential (0 V). This separation allows independent optimization of photoanodes and photocathodes to maximize efficiency for oxygen evolution and hydrogen evolution, respectively, ultimately facilitating overall water splitting. Additionally, the PEC route minimizes the risk of oxygen and hydrogen mixing, a common issue in conventional water-splitting methods.

The water-splitting mechanism in the PEC route consists of three key steps:

(i) Charge Carrier Generation: Solar illumination on the photoelectrode generates electron-hole pairs.

(ii) Charge Carrier Transport: These charge carriers move from the bulk of the semiconductor to its surface interface.

(iii) Charge Transfer to Electrolyte: The charges are transferred to the electrolyte, facilitating the electrochemical oxidation or reduction of water.

The water-splitting mechanism in the PEC route consists of three key steps:

(iv) Charge Carrier Generation: Solar illumination on the photoelectrode generates electron-hole pairs.

(v) Charge Carrier Transport: These charge carriers move from the bulk of the semiconductor to its surface interface.

(vi) Charge Transfer to Electrolyte: The charges are transferred to the electrolyte, facilitating the electrochemical oxidation or reduction of water.

The schematic re-presentation of the PEC water splitting process is shown in the scheme 2.
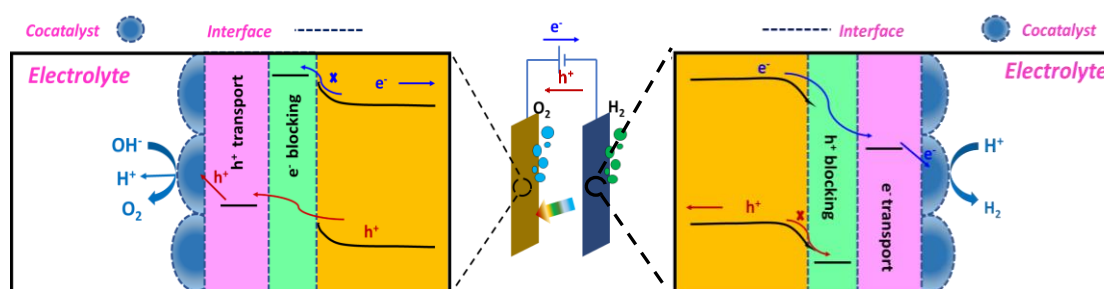
Scheme 2: Schematic of the photo-electrocatalytic splitting of water using photocathode and photoanode

For effective PEC water splitting, the semiconductor must meet several critical criteria:

i. Band Gap: The band gap should exceed 1.23 eV to drive the water-splitting reaction, but it must not be excessively high. A band gap above 3.2 eV is not ideal, as it falls within the UV range, which constitutes a small portion of the solar spectrum.

ii. Electrical Conductivity: The material must exhibit good electrical conductivity to transport the charge carriers generated by solar absorption to the interface for subsequent reactions.

iii. Charge Transfer Efficiency: Once charge carriers reach the surface, they must transfer efficiently to the water to drive the redox reactions.

iv. Stability: The catalyst must withstand prolonged use in a reactive environment where continuous generation of electrons and holes occurs. These reactive species can degrade the catalyst over time, so durability is essential.

v. Sustainability: The catalyst should be made from earth-abundant materials to ensure economic and environmental sustainability.

While the challenges associated with photoanodes and photocathodes are similar, there are distinctions. Oxygen evolution, at the photoanode, is more complex than the hydrogen evolution process occurring at the photocathode. In this article we will discuss the basic parameters which define the photoanode performance as well as advanced techniques which allow us to comprehend detailed mechanism and thereby design better catalysts.

2. Representative parameters in photoelectrochemical (PEC) measurements

The separation of charges generated by photoexcitation plays a key role in the catalysis process. Two important efficiencies are evaluated:

Surface Charge Separation Efficiency ($\eta_{tranfer}$): This indicates the efficiency of charge transfer at the electrode-electrolyte interface.

Bulk Charge Separation Efficiency ($\eta_{trasport}$): This reflects the efficiency of charge carrier transport from the bulk of the material to the surface.

These are calculated using the following equations:

$$\eta_{tranfer} = \frac{J_{H_2O}}{J_{Na_2SO_3}} \times 100\,\% \qquad (5)$$

$$\eta_{trasport} = \frac{J_{Na_2SO_3}}{J_{max.}} \times 100\,\% \qquad (6)$$

$$J_{max.} = \frac{integration\ of\ light\ absoption}{integration\ of\ solar\ light\ spectrum} \qquad (7)$$

Where, $J_{max.}$ is calculated from the photocurrent obtained from the silicon detector. J_{H_2O} is photocurrent density of the water and $J_{Na_2SO_3}$ is the photocurrent of the oxidation of the sulfite which is a hole scavenging agent (sacrificial agent) ensuring 100% utilization of the holes produced for the photoanodes. For the photocathode the ethylene glycol, sodium sulphite, mixtures of sodium sulphide and sodium sulphite, glucose and lactic acid is generally used as the sacrificial agents.[1, 2] To evaluate the performance of the catalysis process, several efficiency parameters are considered. One key parameter is the Incident Photon-to-Current Efficiency (IPCE), which is calculated using the following equation:

$$IPCE\ \% = \left(\frac{J\left(\frac{A}{cm^2}\right)}{P_{in}\left(\frac{w}{cm^2}\right)} \times \frac{1240}{\lambda(nm)} \right) \times 100\ \% \qquad (8)$$

Where J is the measured photocurrent density, P_{in} is the power of the incident monochromatic light (measured by the silicon-based detector) and λ is the wavelength in nm. The IPCE measures the efficiency with which incident photons are converted into an electrical current, providing valuable insight into the photoelectrode's performance. IPCE % represents the ratio of photon utilization i.e. fraction of the photons which produces photo current to the total number of photons falling on the photoelectrode. IPCE% does not account for the photons lost due to reflection or transmission without getting absorbed by the semiconductor photoelectrode. A more accurate parameter for comparing photoanodes is the Absorbed Photon-to-Current Conversion Efficiency (APCE). APCE measures the ratio of photons generating photocurrent to the total photons absorbed by the photoelectrode, factoring in the material's absorptivity in the visible spectrum. It provides a clearer representation of the photoelectrode's efficiency. APCE is calculated using the equation

$$APCE\ \% = IPCE/(1-10^{-OD}) \times 100 \qquad (9)$$

Where OD is absorbance of the material. The measurements of IPCE and APCE provide valuable insights into the performance of the catalysis process. Both parameters rely on the catalytic current obtained during the process. In cases where the concentration of evolved hydrogen is not determined, IPCE and APCE are widely accepted as reliable metrics for comparing the efficiency of different catalytic systems.

Finally, the solar to hydrogen efficiency (STH %) defines efficiency at which the PEC cell is able to generate hydrogen due to the exposure of one sun light. The STH % is defined as,

$$\text{STH \%} = \left[\frac{\left(\frac{\text{mol H}_2}{\text{s}} \right) \times \left(237{,}000 \, \frac{\text{J}}{\text{mol}} \right)}{P_{\text{in}} \left(\frac{\text{W}}{\text{cm}^2} \right) \times A(\text{cm}^2)} \right] \times 100 \qquad (10)$$

In the PEC process, the moles of hydrogen generated are normalized based on the energy input from the solar simulator. Additionally, the Applied Bias Photon-to-Current Efficiency (ABPE) is an important parameter used when experiments are conducted at a bias potential other than the water-splitting redox potential (1.23 V). ABPE accounts for the electrical energy corresponding to the applied bias by subtracting it from the total energy input during efficiency calculations.

$$\text{ABPE} = \frac{J_{H_2O} \times (1.23 - V_{\text{bias}})}{P_{\text{in}}} \times 100 \, \% \qquad (11)$$

The Faradaic efficiency (FE%) of the photoelectrodes are determined by measuring the evolved oxygen gas using the gas chromatography measurements and using the following equation (6)

$$\text{FE (\%)} = Q_{(O2)}/Q_{(\text{total})} \qquad (6)$$

Where $Q_{(O2)}$ is the charge equivalent to the evolved oxygen, which is determined from the measured O_2 concentration in moles from the GC measurements and converting it to charge considering the number of holes transferred as 4. [3, 4] $Q_{(\text{total})}$ is the total charge passed in the PEC cell at the specified applied potential for a predetermined amount of time.

The electronic property of semiconductor is evaluated from the Mott-Schottky measurements, where the experiments are performed at a fixed frequency with the variation of the applied bias potentials. The parameters like, donor density (ND) and flat band potential (VFB) are determined from the plot of 1/C2 vs applied bias potentials in correlation with the equation 12.

$$\frac{1}{C^2} = \frac{2}{q A^2 \varepsilon \varepsilon_0 N_D} \left(V - V_{FB} - \frac{k_B T}{q} \right) \qquad (12)$$

Where, C is the space charge capacitance, q is elementary charge, A is electrode surface area, ε_0 vacuum permittivity (8.854×10^{-12} F m-1), ε is relative permittivity of the photoanode, V is applied potential, k_B is the Boltzmann constant (1.38×10^{-23} J K-1), and T is absolute temperature. The flat band potential (V_{FB}) indicates the extent of band bending, more is the band bending more is the energy available for the minority carriers for the redox processes.

With these parameters, the bulk efficiency of the materials can be determined but the processes occurring at the interface is of prime importance especially the charge transfer and charge recombination as recombination is the major hole loss pathway. Traditional techniques can not decouple the charge transfer and recombination process. The efficiency of the overall photoelectrochemical response is determined by surface processes, which can be analyzed through specific techniques. During EIS measurements, potential perturbation at the semiconductor/electrolyte interface affects the equilibrium density of electrons and holes within the space charge region in the absence of illumination. In contrast, at a metal/electrolyte interface, applying potential directly impacts the Helmholtz layer, allowing potential perturbations during EIS measurements to influence the rate constant. Additionally, variations in light intensity over time control the generation and collection rate of non-equilibrium charge carriers. Electrical responses measured under open-circuit conditions, where photovoltage is fundamental, form the basis of IMVS, whereas photocurrent measurements under controlled potential form the basis of IMPS. The perturbation in light intensity is sinusoidal, given by equation (13) [5].

$$I(t) = I_0(1 + \delta \sin(\omega t)) \tag{13}$$

Where, δ is the depth of modulation and I_0 is the mean intensity.
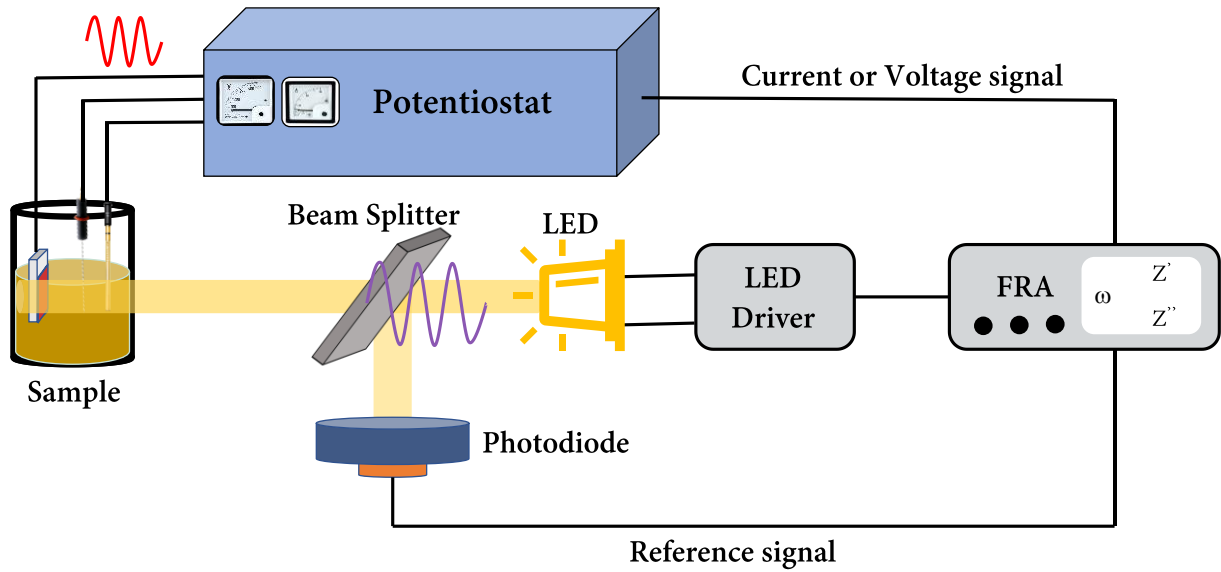
Scheme 3 Basic experimental setup of IMPS/IMVS measurements

Intensity modulation is achieved using a frequency response analyzer (FRA) in combination with an LED light source and a beam splitter. The light emitted by the LED is split into two parts: one is directed into the PEC cell, while the other is sent to a high-speed Si photodiode. The FRA generates a small-amplitude modulated sinusoidal light intensity, which is then superimposed onto a constant intensity illumination. The modulated photocurrent, which is sum of hole current and electron current, has same frequency as that of the light but with different magnitude and phase. Phase shift in photocurrent in relation to sinusoidal modulation of light intensity is measured. The model to understand IMPS responses of semiconductor/electrolyte interface was provided by Ponomarev and Peter [6, 7]

This model tells about the competition between transfer of minority charge carrier to electrolyte(k_{ct}) and recombination to electron in conduction band (k_{rec}). The normalized transfer function for IMPS can be represented as a function of angular frequency as in equation (14)[8]

$$\frac{J_{photo}}{J_h} = \frac{k_{ct} + i\omega}{k_{ct} + k_{rec} + i\omega} \ (i^2 = -1)$$

$$(14)$$

Where J_{photo} is the measured photocurrent, J_h is hole current, k_{ct} and k_{rec} are the pseudo-first order charge transfer and recombination rate constants. It is important to understand that k_{ct} and k_{rec} are phenomenological rate constants as actual rate constants would require to investigate each elementary step involved in the water oxidation process. Now these in and out of phase components leads to real and imaginary part of photocurrent which can be plotted as Nyquist plot.

The expressions for the real and imaginary photocurrents in the Nyquist plot are represented in equation (15) and equation (16) respectively[8].

$$Re(J_{photo}/j_h) = (k_{ct}(k_{ct} + k_{rec}) + \omega^2)/((k_{ct} + k_{rec})^2 + \omega^2)$$

$$(15)$$

$$Im(J_{photo}/j_h) = k_{rec}\omega/((k_{ct} + k_{rec})^2 + \omega^2)$$

$$(16)$$

A typical IMPS plot consists of two semicircles in the positive real plane of Nyquist plot as shown in Fig. 1b. One semicircle in negative plane of imaginary part while other in positive plane of imaginary part. Two semicircles are resulting since phase shift associated with the effect from recombination and of $R_{sol}C_{SC}$ have opposite sign. Where R_{sol} is the series resistance, essentially the solution resistance and C_{sc} is the space charge capacitance.

The frequency of semicircle in positive real half plane decreases as the series resistance of PEC increases. In this plot, at high frequency intercept (HFI) with real photocurrent axis, the surface recombination rate is insufficient to match the rate at which holes are produced with light modulation. HFI provide information about hole flux moving to photoelectrode surface. The low frequency intercept (LFI) on real photocurrent axis measure the rate at which charges are transfers to solution for water oxidation. The ratio of Low frequency intercept and high frequency intercept provides the Charge transfer efficiency of the process as shown in equation (17)

$$\eta_{ct} = \frac{k_{ct}}{k_{ct}+k_{rec}} = \frac{LFI}{HFI}$$

$$(17)$$

From the Nyquist plot, frequency at which maximum imaginary photocurrent (ω_{LF}) is related with the characteristic relaxation constant of the system by equation (18).

$$\omega_{LF} = k_{ct} + k_{rec}$$

$$(18)$$

From these two equations the rate constants for the charge transfer process and that of the recombination process are evaluated.

3. Illustration of application of these techniques for evaluating photoanodes

3.1 Bismuth Vanadate and 3D-Graphene Composite Photoanodes for Enhanced Photoelectrochemical Oxidation of Water

3D graphene incorporated $BiVO_4$ was synthesized by spin coating followed by annealing. The synthesized photoanodes were characterized using various methods viz. XRD, UV-Vis spectroscopy, Raman spectroscopy, SEM, XPS etc. 3D graphene inclusion aimed at enhancing the conductivity of the material and thereby enhance the charge transport. In this regard transient time constant evaluation provides valuable insight.
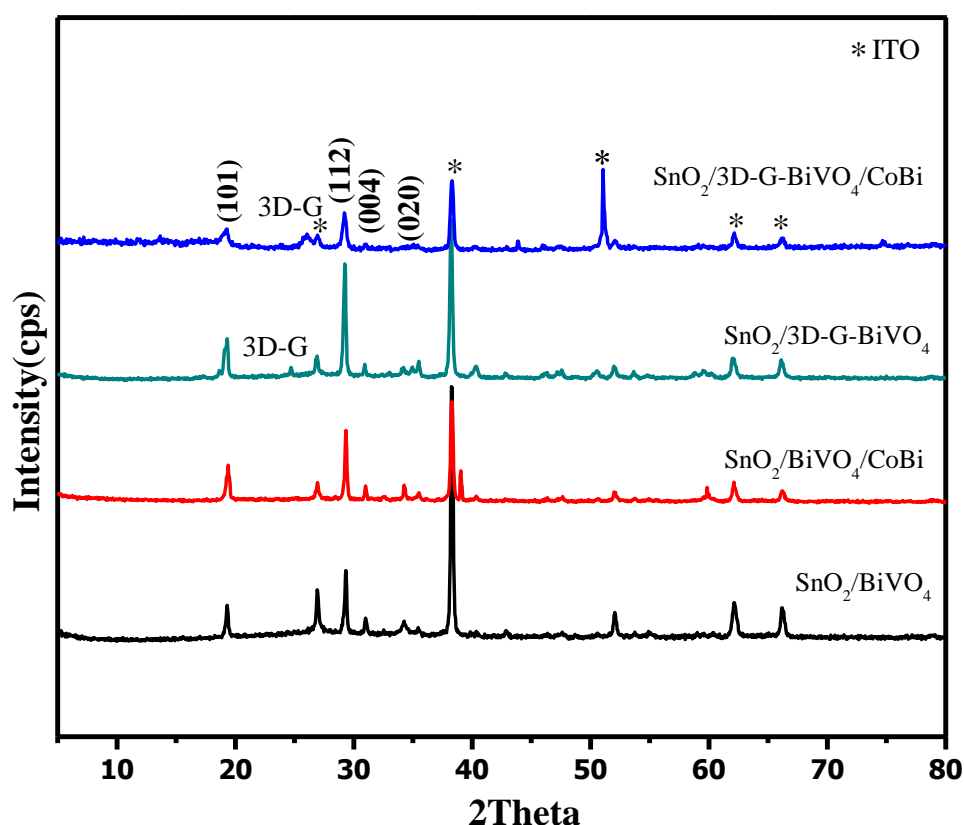
Fig. 1. XRD pattern of $SnO_2/BiVO_4$ (black), $SnO_2/BiVO_4$ /Co-B_i (red), $SnO_2/3D$-G-$BiVO_4$ (green), $SnO_2/3D$-G-$BiVO_4$/Co-B_i (blue)

The XRD peaks at 26.37˚, 34.58˚, 37.45˚, 61.37˚ and 65.45˚ shows underneath ITO (JCPDS card 41-1445) substrate. XRD peaks at 2θ values of 18.46˚, 28.48˚, 30.10˚, 34.95˚ correspond to (011), (121), (040) and (002) planes of monoclinic $BiVO_4$ (JCPDS 014-0688)

respectively (Fig. 1). Upon incorporation of 3D-G weak peak around 25° appears indicating the presence of 3D-G. $BiVO_4$ phase is preserved after introduction of Co-B_i into the system as no change is observed in peak positions. The XRD plots indicated that the crystallinity of the ITO/SnO_2/3D-G-$BiVO_4$/Co-B_i sample is relatively lower compared to the other three samples.
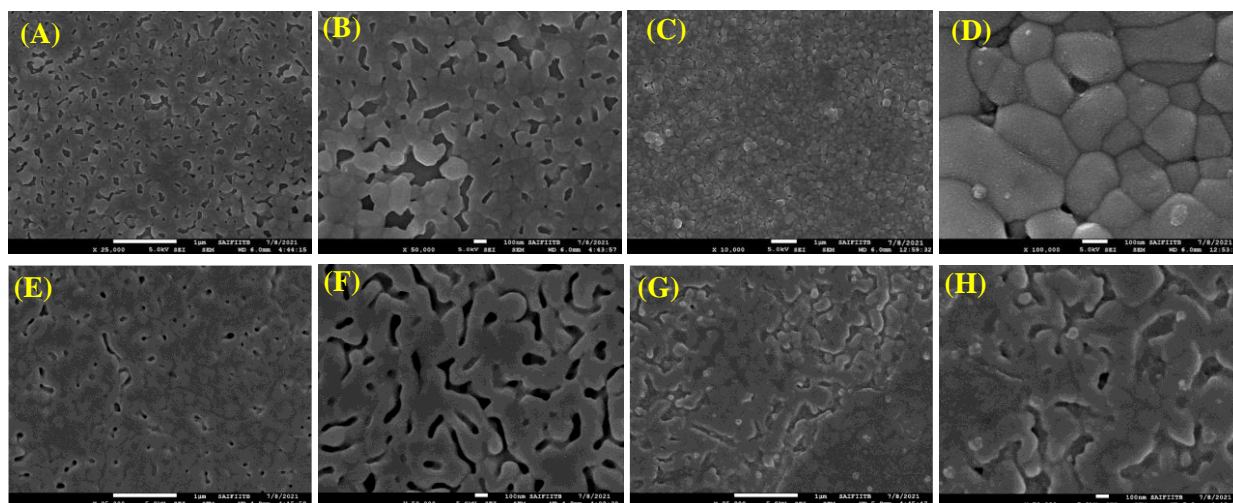
Fig.2 SEM images of (A) & (B) SnO_2/$BiVO_4$, (C) & (D) SnO_2/$BiVO_4$ /Co-B_i, (E) & (F) SnO_2/3D-G-$BiVO_4$, (G) & (H) SnO_2/3D-G-$BiVO_4$/Co-B_i

Photoelectrochemical investigation

Photoelectrochemical investigations have been carried out for all the photoanodes under AM 1.5 G simulated illumination using xenon lamp. The 0.5M Na_2SO_4 in borate buffer of pH 8 has been used as electrolyte, instead of using phosphate buffer due to its corrosive nature for $BiVO_4$ systems. [9] Performance of the photoanodes were investigated by LSV and chopped light voltammetry (CLV) and the results are shown in Fig. 6A & 6B. Current densities obtained at 1.19V vs RHE for SnO_2/$BiVO_4$, SnO_2/3D-G $BiVO_4$, SnO_2/$BiVO_4$/Co-B_i and SnO_2/3D-G-$BiVO_4$/Co-B_i are 0.74, 0.90, 1.23 and 1.48 mAcm^{-2} respectively. The incorporation of 3D-G leads to an approximate 165% enhancement in PEC current, highlighting its significant and quantifiable role in boosting the photocurrent density of the electrodes. Furthermore, photoanodes with 3D-G exhibit high current density even at lower applied biases, with the improvement being particularly pronounced at lower potentials. Additionally, the shape of the LSV plot differs for samples containing 3D-G compared to those without it.[10, 11] he presence of 3D-G has enhanced conductivity, resulting in an increased photocurrent at lower overpotentials. In contrast, for samples without 3D-G, the photocurrent

remained low at lower bias potentials. However, once the bias potential (1.3 V vs. RHE) was sufficient to drive the majority carriers back to the sink, the current increased rapidly.

Chopped light voltammetry experiments, shown in Fig. 4B, revealed a similar trend in current density across all catalyst materials, consistent with the observations from linear sweep voltammetry. A noticeable reduction in current was observed immediately after the light-off stage in samples lacking 3D-G. With increase in overpotential the reduction current disappears. The absence of the reduction current in SnO_2/3D-G-$BiVO_4$ even at lower overpotential than that of SnO_2/$BiVO_4$ indicates the efficient transfer of electrons towards the sink and effective separation of e-h pair by the enhanced conductivity of 3D-G. It is worth noting that the reduction current becomes more pronounced with the introduction of Co-B_i into the system. This supports the rationale behind incorporating Co-B_i to enhance the interfacial transfer of holes to the solution. Consequently, after the illumination is turned off, excess electrons accumulate in Co-B_i-containing samples without 3D-G, leading to a minor reduction current. However, this reduction current is absent when 3D-G is introduced into the Co-Bi system, as 3D-G facilitates the transfer of electrons to the sink. The current transient behaviors have indicated the enhancement of life time of the charge carriers. The quantification of improvement of performance to the surface charge recombination and the bulk charge recombination has been evaluated from the measurements of the surface charge separation ($\eta_{transfer}$) and bulk charge separation ($\eta_{trasport}$) efficiencies of the photoanodes using the procedures as explained in the equations 5, 6 and 7. The results are plotted in Fig. 3A & 3B. The $\eta_{transfer}$ has been improved upon inclusion of Co-B_i in the $BiVO_4$ sample due to the electro-catalytic activity and efficient transfer of surface charges to the solution. Presence of 3D-G has significant enhancement in the surface charge separation process, which indicates that 3D-G has positive role in the enhancement of surface conductivity of the material, which resulted in the efficient transfer of holes to the solution. The variation of $\eta_{trasport}$ with respect to the applied bias potentials are also plotted and shown in Fig. 3B. The significant enhancement of the ($\eta_{trasport}$) especially at the lower overpotentials upon incorporation of 3D-G has the clear indication about the improvements in e-h recombination of the materials.
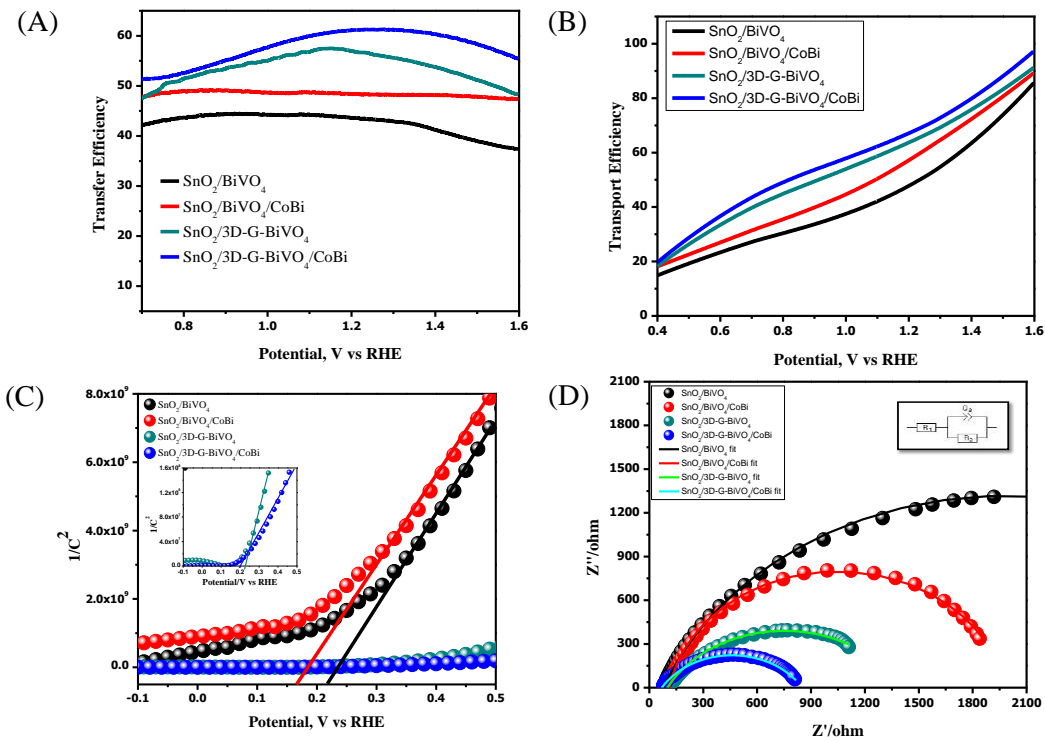
Fig. 3. (A) Transfer efficiency (B) Transport Efficiency (C) Mott Schottky Plot at 100Hz (D) Nyquist Plot of $SnO_2/BiVO_4$ (black), $SnO_2/BiVO_4/Co-B_i$ (red), $SnO_2/3D-G-BiVO_4$ (green), $SnO_2/3D-G-BiVO_4/Co-B_i$ (blue)

The transient behavior of the photocurrent for all materials was recorded and is presented in Fig. 4C. Upon illumination of the photoelectrode, an initial spike occurs due to the rapid separation of electron-hole pairs. Electrons migrate toward the ITO, while holes move toward the electrolyte interface to oxidize water. Additionally, some holes recombine with conduction band electrons during this process.. The decay in the initial photocurrent has been observed with the $SnO_2/BiVO_4$ and $SnO_2/BiVO_4/Co-B_i$ photoanodes, whereas the decay has been less significant with the $SnO_2/3D-G-BiVO_4$ and $SnO_2/3D-G-BiVO_4/Co-B_i$ photoanodes. In order to obtain the decay profile of the photocurrent, the transient photocurrent is fitted using the following dimensionless parameter D,

$$D = (I_{(t)} - I_{(st)})/(I_{(in)} - I_{(st)}) \qquad (19)$$

Where $I_{(t)}$ is the photocurrent at time t, $I_{(in)}$ is the initial photocurrent measured at t=0 and $I_{(st)}$ is the steady photocurrent. Transient time constant (τ) is defined as the time at which ln(D)= -1. [12] Transient behaviour of the photoanodes has been studied by illuminating the

photoanodes for a short time period of 1 s at 1.19V vs RHE and the decay characteristic is observed (Fig. 4D). Value of observed τ are 0.17s, 0.19 s and 0.5 s for $SnO_2/BiVO_4$, $SnO_2/BiVO_4/Co-B_i$ and for $SnO_2/3D-G-BiVO_4$ samples respectively. While $SnO_2/3D-G-BiVO_4/Co-B_i$ does not show any significant decay. Photoelectrochemical efficiency of $BiVO_4$ remains low due to the fast charge recombination owing to numerous recombination and charge trapping centers. Incorporation of 3D-G provide low energy pathways for the photogenerated charges due to high electronic conductivity, thereby reducing the recombination as reflected by the transient time constant. Lower recombination is the reason underneath the enhanced photocurrent   density.
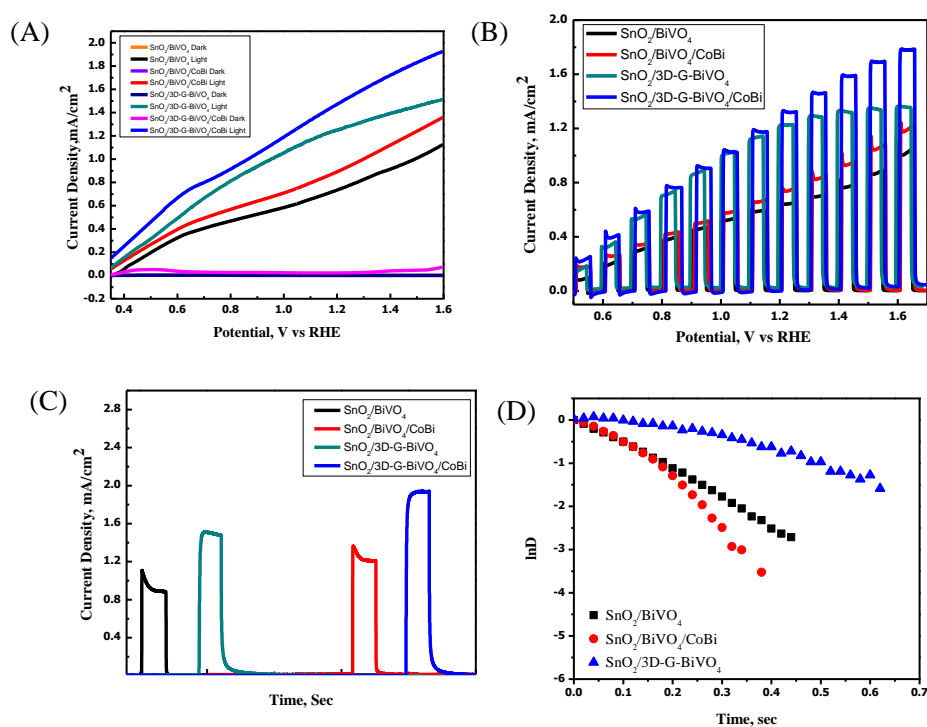
Fig. 4. (A) Linear Sweep Voltammetry (BBS Buffer pH 8), (B) Chopped light Voltammetry for $SnO_2/BiVO_4$ (black), $SnO_2/BiVO_4 /Co-B_i$ (red), $SnO_2/3D-G-BiVO_4$ (green), $SnO_2/3D-G-BiVO_4/Co-B_i$ (blue) (C) Transient Study for $SnO_2/BiVO_4$ (black), $SnO_2/BiVO_4 /Co-B_i$ (red), $SnO_2/3D-G-BiVO_4$ (green), $SnO_2/3D-G-BiVO_4/Co-B_i$ (blue) , (D) ln D vs Time graph for $SnO_2/BiVO_4$ (black), $SnO_2/BiVO_4 /Co-B_i$ (red), $SnO_2/3D-G-BiVO_4$ (blue)

Correlation between the efficiency and wavelength is extracted from IPCE measurements and plotted in Fig. 5 of the supporting information. IPCE of $SnO_2/BiVO_4$ is ~20% while efficiency

of SnO$_2$/3D-G-BiVO$_4$, SnO$_2$/BiVO$_4$/Co-B$_i$ and SnO$_2$/3D-G-BiVO$_4$/Co-B$_i$ are ~27%, 23% and 32% respectively.[13, 14]
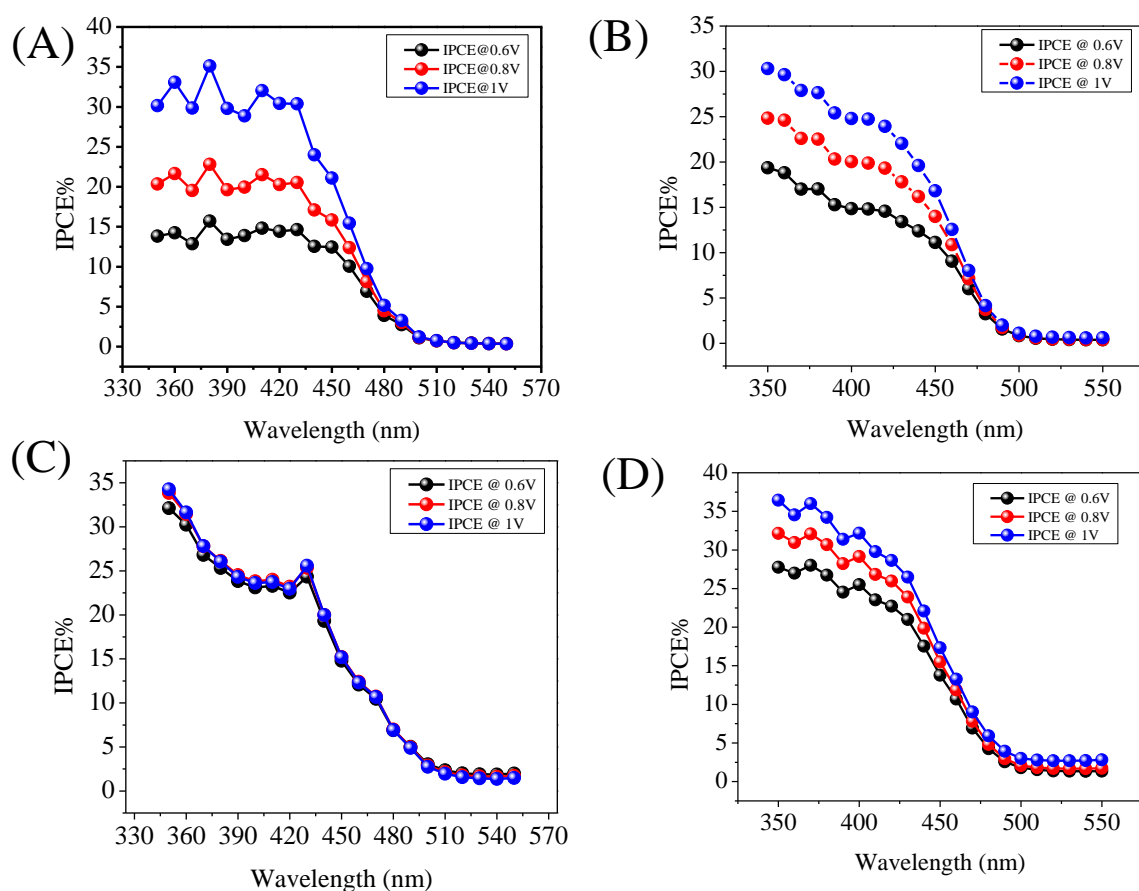
Fig 5: IPCE plot for (A) SnO$_2$/BiVO$_4$ (B) SnO$_2$/BiVO$_4$/Co-B$_i$ (C) SnO$_2$/3D-G-BiVO$_4$ (D) SnO$_2$/3D-G-BiVO$_4$/Co-B$_i$

The APCE has also been measured and the values are plotted in Fig. S4 of the supporting information. As expected, the APCE results follow the same trend as that of IPCE. APCE increases as the applied bias increases due to efficient e-h separation. APCE increases for SnO$_2$/BiVO$_4$ as higher potential is applied. (Fig. 6) Similar pattern is seen in case of SnO$_2$/BiVO$_4$/Co-B$_i$. While in case of SnO$_2$/3D-G-BiVO$_4$ enhancement in current is observed due to effective separation of photogenerated charge carriers even at lower applied potential. As Co-B$_i$ is introduced, APCE of SnO$_2$/3D-G-BiVO$_4$/Co-B$_i$ again increases with increase in applied bias as new redox centers are available and activity of the co-catalyst increases with the applied bias. The FE (%) for the samples SnO$_2$/BiVO$_4$, SnO$_2$/3D-G BiVO$_4$, SnO$_2$/BiVO$_4$/Co-B$_i$ and SnO$_2$/3D-G-BiVO$_4$/Co-B$_i$ are 87, 86, 90 and 89 respectively. The

results thus indicate the insignificant contribution of the non-Faradaic processes in the overall current during PEC oxidation of water.[3, 4, 15]
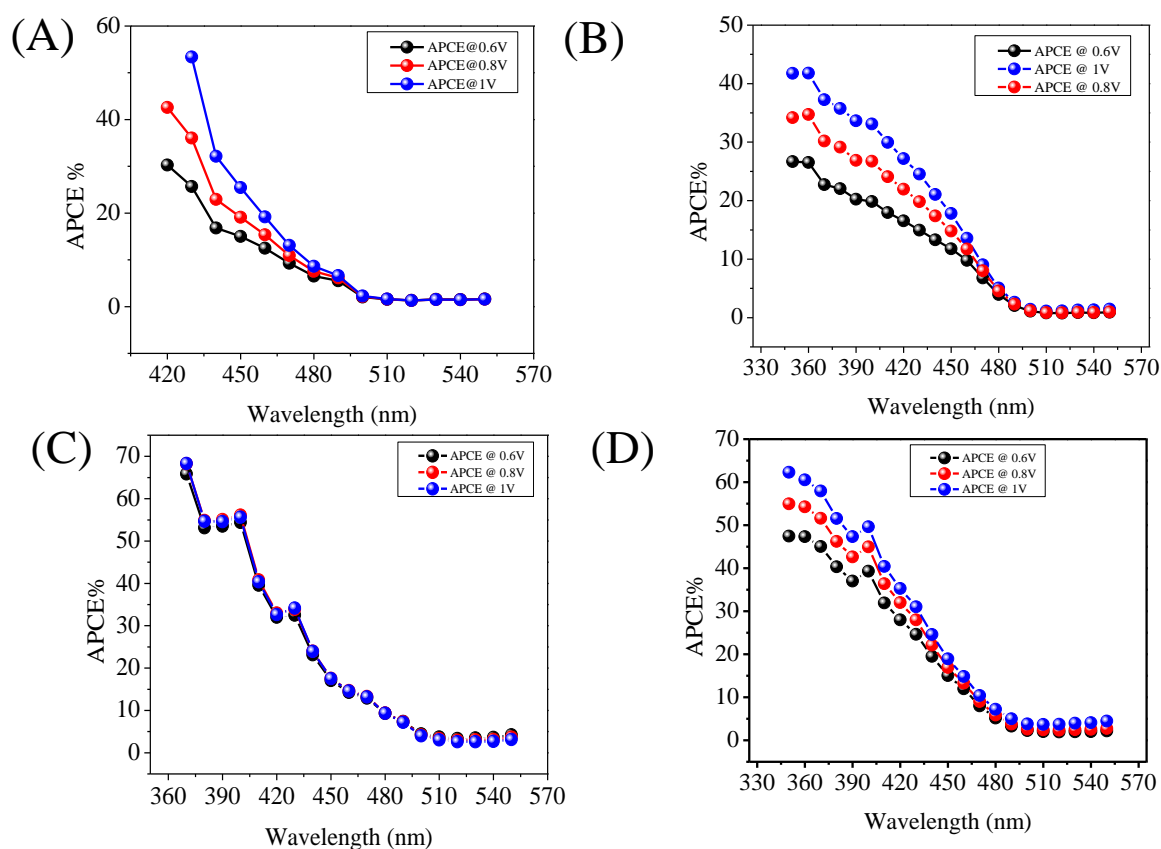
Fig 6: APCE plot for (A) $SnO_2/BiVO_4$ (B) $SnO_2/BiVO_4/Co-B_i$ (C) $SnO_2/3D-G-BiVO_4$ (D) $SnO_2/3D-G-BiVO_4/Co-B_i$

3.2 Application of IMPS for evaluation of hematite photoanodes

Hematite was electrochemically deposited followed by annealing. Iron hydroxide films were deposited onto the FTO substrate from an iron precursor solution ($FeCl_3$) by applying a constant potential of -0.2 V (versus Ag/AgCl electrode) with varying deposition times. During the deposition process, a yellow-colored iron (III) hydroxide (FeOOH) compound was formed according to the following reactions:

$$H_2O_2 + 2e^- \rightarrow 2OH^- \tag{20}$$

$$FeF^{2+} + 3OH^- \rightarrow FeOOH + F^- + H_2O \tag{21}$$

As-deposited samples underwent annealing in ambient air at 550°C for 2 hours, with a subsequent annealing step of 750°C for 10 minutes. This rapid annealing phase at elevated temperatures facilitated the crystallization and activation of the iron oxide nanostructures, resulting in highly activated α-Fe$_2$O$_3$ films with optimized properties for various applications. Photoanodes of varous thickness was synthesized to understand the effect of thickness on charge transfer and recombination process.

The photoanodes were characterized by XRD, UV-Vis and Raman spectroscopy. For PEC efficiency evaluation LSV, CLV, EIS, Mott-Schottky, transient photocurrent, IMPS was carried out. The obtained results revealed varying current densities at 0.6 V, indicating the efficiency of the photoelectrode under different conditions. Specifically, current densities of 0.53 mAcm^{-2}, 0.71 mAcm^{-2}, 0.89 mAcm^{-2}, 0.42 mAcm^{-2}, and 0.21 mAcm^{-2} were observed for 0.807 μm, 0.903 μm, 1.00 μm, 1.12 μm and 1.38 μm, respectively. Notably, the photoelectrode fabricated with 1.00 μm displayed the highest photoelectroactivity among the tested conditions. The relevant PEC performance are plotted in fig 6.
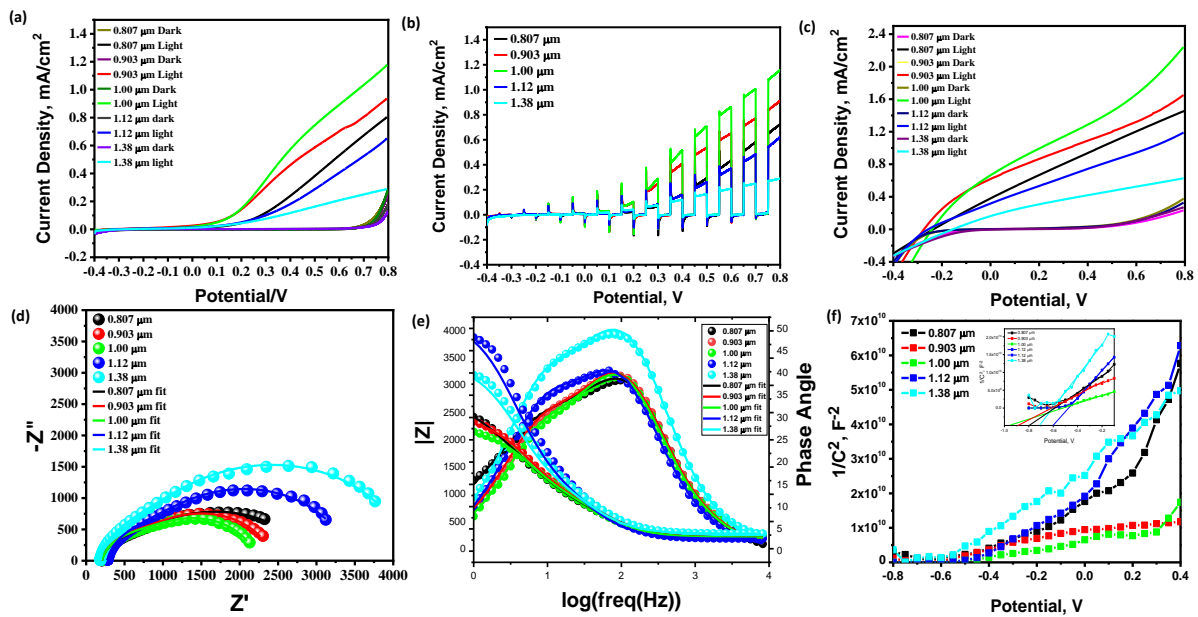
Figure 6 (a) Linear Sweep Voltammetry (b) Chopped light Voltammetry (c) Linear Sweep Voltammetry (Sulphite) (d) Nyquist Plot at 0.6V (e) Bode plot (f) Mott Schottky Plot of 0.807 μm (black), 0.903 μm (red), 1.00 μm (green), 1.12 μm (blue), 1.38 μm (sky blue)

To gain deeper insight into the intricate relationship between the material properties and the charge transfer dynamics in the prepared electrodes, a detailed IMPS analysis was performed. The IMPS analysis model relies on linear circuit equations to describe surface state charging, charge transfer, and recombination processes at the solid-electrolyte interface (SEI). However, it is important to recognize that the model is built on specific assumptions. First, it presumes that bulk recombination dominates over surface charge recombination. Second, it assumes that surface recombination takes place within the timescale of IMPS measurements, with light modulation exerting no influence on band bending in the space charge region. The IMPS spectra, when plotted as a function of potential is spread over the fourth and the first quadrant with a real x axis and imaginary y axis similar to Nyquist plot. Simple way of reading an IMPS plot is to correlate the intersection on the real axis with improved charge transfer efficiency. Additionally, the diameter of the upper arc represents charge recombination process. Diminishing upper arc at more positive potentials, indicates a reduction in the charge recombination process.

The IMPS data is modelled using simple equivalent circuit. The semicircle in the upper quadrant corresponds to a time constant formed by the series resistance and the bulk capacitance. The corresponding high frequency intercept on the real axis is given by equation (22).

$$HFI = (1 + \frac{R_s}{R_{HF}})^{-1}$$

$$(22)$$

At the Low frequency limit, the LF capacitor is blocked, and the LF resistor acts like an extra series resistor, giving the LF intercept on the real axis as given by equation (23)

$$LFI = (1 + \frac{R_s + R_{LF}}{R_{HF}})^{-1} \tag{1}$$

ω_{HF} and ω_{LF} are related with different characteristics constants which are presented in equation (23).

$$\omega_{HF} = (R_s C_{bulk})^{-1} \; ; \; \omega_{LF} = (R_{LF} C_{LF})^{-1} \tag{24}$$

In case of hematite IMPS spectra is recorded at different potential values plotted as fig. 8 and a noticeable trend is observed. With increase in potential the intersection on real axis shifted towards higher value and upper arc was smaller. While the former signifies better charge transfer the latter signifies lesser recombination, which can be explained on the basis that with

potential increase the driving force for photogenerated charge separation is stronger. Another trend was noticed across the samples, the sample of 1 µM had the longest real axis intersection and smallest upper arc.
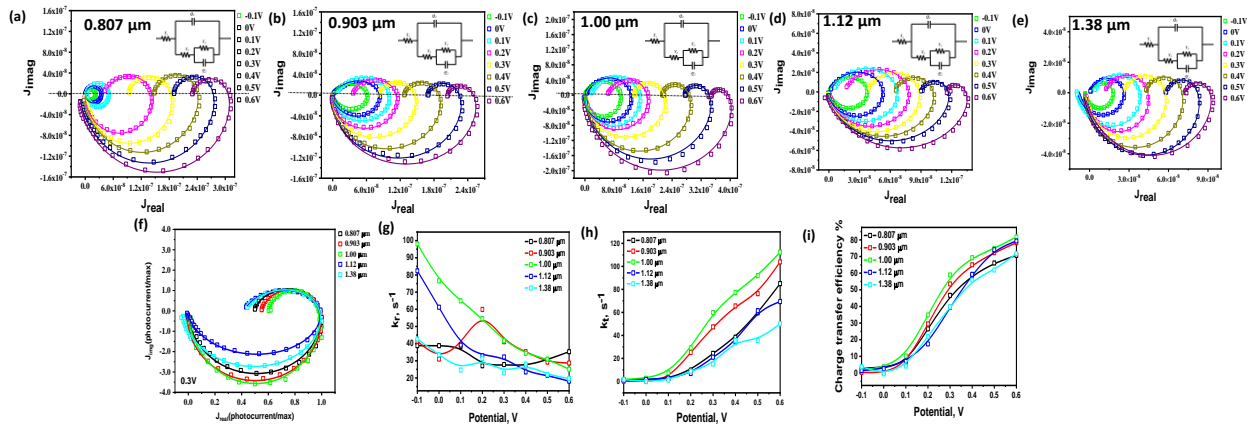

Figure 8 IMPS spectra of (a) 0.807 µm, (b) 0.903 µm, (c) 1.00 µm, (d) 1.12 µm, (e) 1.38 µm at different potential (f) Normalized IMPS plot for 0.807 µm (black), 0.903 µm (red), 1.00 µm (green), 1.12 µm (blue), 1.38 µm (sky blue) at 0.3V (g) Variation of K_t with potential (h) Variation of Kr with potential (i) Charge transfer efficiency for 0.807 µm (black), 0.903 µm (red), 1.00 µm (green), 1.12 µm (blue), 1.38 µm (sky blue)

Even though with increasing thickness the light harvesting efficiency and number of charge carriers were better but the very intrinsic property of the material namely, the hole diffusion length limits the utilization of the charge carriers and they heavily recombine, limiting the efficiency of the thicker samples. Thus, for hematite of optimum thickness would have best efficiency.

1. Conclusion:

By these two representative examples one can have a clearer picture of the parameters important for evaluation of photoanodes. Along with the basic studies parameters like transient time constant and its physical meaning with respect to charge carrier dynamics is also focused. Theory of advanced techniques like IMPS has been thoroughly discussed along with interpretation of the IMPS plots and application of the same for evaluating charge transfer and recombination rate.

References:

1. Clarizia, L., M.N. Nadagouda, and D.D. Dionysiou, *Recent advances and challenges of photoelectrochemical cells for hydrogen production.* Current Opinion in Green and Sustainable Chemistry, 2023. **41**: p. 100825.
2. Thakur, A., et al., *Current progress and challenges in photoelectrode materials for the production of hydrogen.* Chemical Engineering Journal, 2020. **397**: p. 125415.
3. Meng, Q., et al., *R. d. Marco, GA Crespo and L. Sun, Efficient BiVO 4 photoanodes by postsynthetic treatment: remarkable improvements in photoelectrochemical performance from facile borate modification.* Angew. Chem., Int. Ed, 2019. **58**(52): p. 19027-19033.
4. Wang, M., et al., *Enhancing the photoelectrochemical water oxidation reaction of BiVO4 photoanode by employing carbon spheres as electron reservoirs.* ACS Catalysis, 2020. **10**(21): p. 13031-13039.
5. Peter, L.M., *Dynamic aspects of semiconductor photoelectrochemistry.* Chemical Reviews, 1990. **90**(5): p. 753-769.
6. Ponomarev, E. and L. Peter, *A generalized theory of intensity modulated photocurrent spectroscopy (IMPS).* Journal of Electroanalytical Chemistry, 1995. **396**(1-2): p. 219-226.
7. Kandiel, T.A., M.G. Ahmed, and A.Y. Ahmed, *Physical Insights into Band Bending in Pristine and Co-Pi-Modified BiVO4 Photoanodes with Dramatically Enhanced Solar Water Splitting Efficiency.* The Journal of Physical Chemistry Letters, 2020. **11**(13): p. 5015-5020.
8. Peter, L., E. Ponomarev, and D. Fermin, *Intensity-modulated photocurrent spectroscopy: reconciliation of phenomenological analysis with multistep electron transfer mechanisms.* Journal of Electroanalytical Chemistry, 1997. **427**(1-2): p. 79-96.
9. Toma, F.M., et al., *Mechanistic insights into chemical and photochemical transformations of bismuth vanadate photoanodes.* Nature communications, 2016. **7**(1): p. 12012.
10. Seabold, J.A. and K.-S. Choi, *Efficient and stable photo-oxidation of water by a bismuth vanadate photoanode coupled with an iron oxyhydroxide oxygen evolution catalyst.* Journal of the American Chemical Society, 2012. **134**(4): p. 2186-2192.
11. Shi, L., et al., *Annealing temperature effects on photoelectrochemical performance of bismuth vanadate thin film photoelectrodes.* RSC advances, 2018. **8**(51): p. 29179-29188.
12. Tafalla, D., P. Salvador, and R. Benito, *Kinetic approach to the photocurrent transients in water photoelectrolysis at n-TiO2 electrodes: II. Analysis of the photocurrent-time dependence.* Journal of the Electrochemical Society, 1990. **137**(6): p. 1810.
13. Lee, M.G., et al., *Tailored BiVO4/In2O3 nanostructures with boosted charge separation ability toward unassisted water splitting.* Carbon Energy, 2023: p. e321.
14. Ye, H., H.S. Park, and A.J. Bard, *Screening of electrocatalysts for photoelectrochemical water oxidation on W-doped BiVO4 photocatalysts by scanning electrochemical microscopy.* The Journal of Physical Chemistry C, 2011. **115**(25): p. 12464-12470.
15. Lee, M.G., et al., *Crystal facet engineering of TiO2 nanostructures for enhancing photoelectrochemical water splitting with BiVO4 nanodots.* Nano-micro letters, 2022. **14**(1): p. 48.

EIHE 2025

Members of Accommodation, Transport, Catering, registration & Hall management Committees

N. Raje	Swarup K. Gupta
P. S. Remya Devi	N. Ajith
B. N. Singh	Suvarna Sounderajan
A. A. Dalvi	H. Parab
B. B. Kalekar	J. Ramkumar
Shiny S. Kumar	Kavita Jayachandran
Sujata Pawar	H. Basu
Pratibha S. Bhaye	N. Ajith
A. S. Ambolikar	Kalpesh Tembe
Preeti Awasthi	V. Kasar
Ashutosh Srivastava	M. Ghosh
R. D. Ghadigaonkar	N. Udamale
Alok Mahato	Nidhi Tyagi

PG Tech Group of Companies
(Established Since 2001)

PGTech®
Planet Green Technology

PG TECH PVT. LTD.

R2
RAM2 LABORATORIES
PVT. LTD.

GYAN PREM
Education & Social Development Society

Manufacturers

भा प अ कें
BARC
ATOMS IN THE SERVICE OF THE NATION

Technology Partner with BARC

Rare Earth Metals and Magnets

Chemical Storage Cabinet (CSC)

Clean System (CS)

Authorised Import Distributors

Waters™

HPLC   UPLC
HRMS   LCMSMS

mBRAUN
Clean. Engineering. Expertise.

GLOVE BOX

WATER PURIFICATION

VERDER scientific
CARBOLITE GERO
ELTRA   Retsch
QATM   MICROTRAC MRB

BALL MILL   TUBE & BOX FURNACE
ONH ANALYSER

MICRO BALANCE

Testing & Training Laboratory
(Food & Pharma)

MSME
MICRO, SMALL & MEDIUM ENTERPRISES
सूक्ष्म, लघु एवं मध्यम उद्यम

GMP CERTIFIED

CE

MAKE IN INDIA

ISO 9001:2015

GeM
Government e Marketplace
Efficient • Transparent • Inclusive

एन एस आई सी
NSIC
ISO 9001 : 2008

📞 +91-9826969100   ✉ admin@pgtech.in   🌐 www.pgtech.in

📍 Address:-38, Electronic Complex, Opp. ITI, Pradeshipura, INDORE-452001 (M.P.)

GENERAL TRADING CORPORATION

INTRODUCTION

We introduce ourselves as one of the Leading Dealers, Importers & Stockiest of Laboratory Glasswares, Chemicals & Scientific Instruments, ESTABLISHED SINCE 1952, an if you give us a chance by registering your firm in your Vendor's list and send us your Regular Valued Enquiries, from time to time, we assure you to give you our most competitive rates, backed by our services, for the available items.

We specialize and maintain regular stock of the following items

➢ **Quartz and Silica tubes, rods, wools, boats, beakers, crucibles, plates, disc, etc**
➢ **All sizes of Agate Mortar & Pestles, Basins, etc**
➢ **All sizes of Laboratory Teflon materials, Silicon tubings**
➢ **High Purity Alumina wares such as crucibles, tubes, trays, boats, etc**
➢ **Quartz Single and Double distillation apparatus**
➢ **Digital balances (Analytical, Top-loading, Industrial, etc)**
➢ **Silver & Platinum Paste**
➢ **High purity metals such as: Platinum, tungsten, tantallum, molybdenum in the form of foils, wires powders etc.**
➢ **Chemicals / Solvents /Speciality Chemicals / Biochemicals / Kits / Antibodies**

We also deal in the following:

➢ All types of Laboratory Instruments such as Ovens, Incubators, Hot Plates, pH Meters, Ultrasonic baths, Water Baths, Water Stills, Gas Flow Meters, BOD Incubators, Furnaces, Constant Temperature Water Baths, Microscopes, Karl Fisher Apparatus, Autoclaves, Gas Generators, KBR Hydraulic Press, Portable & Oil-sealed Vacuum Pumps
➢ All types of Imported Instruments such as Spectrophotometers, Viscometers, Weighing Balances, Pocket pH Meters, Digital Conductivity Meters, Portable pH/mV/Temperature Meter, Dissolved Oxygen Meter
➢ Rotameters of all types
➢ **Whatman** Filter Papers, Membrane Filters, Syringe filters, Nylon Filters, Butter Papers, etc
➢ **Borosil / Duran / JSil / JSGW** Glasswares
➢ Test Sieves & Sieve Shaker
➢ Spares for GC & HPLC Systems
➢ Ice Flakers, Deep freezers, Refrigerators, Microwave Oven
➢ Laminar Air Flow, Bio-safety Cabinet, Fume Hoods
➢ Hydrometers, Thermometers with certificate
➢ **Tarsons** Make Labware Products
➢ Oil & Petroleum Products

Major Principal Companies : Mettler Toledo, TCI, Sigma, Thermo, Meck Millipore, Tarsons, Abdos, Athena, NEB, CST, Santacruz, R&D Systems, Eppendorf, Kubota, Avantor, Promega, Bioxcell, Invivogen, Himedia, ElabScience, Epigentek, Veego, Cayman, MPBio, GE (Cytiva), Labman/Wensar, Heidolph, Aczet, Bandelin, Sartorius, Brand, Qiagen, Rocker, Starna, Remi, Mltenyi, Chromotek, Bioassay, Wheaton, Moltox, Medchem Express, TargetMol, Horizon Discovery (Dharmacon), Biolegend, Roche, Hanna, TechResource, Waters, Polylab, Lovibond, Sujay, White-Westinghouse, Novita, Ika, Brookfield, Licor, Exciton, Cambridge Isotope, Spectrum (Repligen), Tedpella, Combi-Blocks, Advent, Axygen, Corning, Falcon, Laxbro, Hellma, Shimadzu, PerkinEelmer, Becnhmark, Borosil, JSil, Klasspack, JSGW, Ibidi, Matrix, Metalab, Shanti Scientific, PolyScience, TRC, Technics, Trident, Cole-Parmer, Micro Scientific, Oscacr, Eltek, Electrolab, Jayant, Contech, Schott-Duran, Toshniwal, Systronics, Gilson, Kasablanka, Hamilton, BioRad, LabIndia, Leimco, Rescholar, Star, Horiba, Amber, Genaxy, Strem, & many more

![αtech logo]

Utilising the power of small to make BIG changes

· · · · · · · · · · · · ·

Scanning Electron Microscope

Raman Spectrometer

Confocal Laser Scanning Microscope

Confocal Raman Microscope

X-Ray Microscope

Micro- and Nano-Indentation System

SEM-EDS I micro-Raman I X-Ray CT I Nano-indentation I CLSM | Aerosol Spectrometer | Dust Monitors
Nanoparticle Sizers & Counters | Onboard Vehicular Emission | Heavy Metals in Air Monitor | Bio-aerosol Air Monitor

भारी पानी बोर्ड, मुंबई
परमाणु ऊर्जा विभाग

Heavy Water Board, Mumbai
Department of Atomic Energy

प्रौद्योगिकीय संपदा के माध्यम से राष्ट्र का गौरवान्वयन
Creating Pride for the Nation through Technological Wealth

नाभिकीय एवं विशेष ग्रेड का भारी पानी
Nuclear & Special Grade Heavy Water

पोटैशियम धातु **Potassium Metal**

डयूटेरियम गैस **Deuterium Gas**

एनएमआर विलायक **NMR Solvents**
(CDCl$_3$; Acetone-d6; DMSO-d6; Acetonitrile-d3 etc.)

बोरॉन-10&11 **Boron-10&11**

नाभिकीय ग्रेड सोडियम
Nuclear Grade Sodium

TBP   D2EHPA
D2EHPA-II   DHOA
TiAP   TOPO

निष्कर्षण धातुकर्म हेतु विलायक
Solvents for Extractive Metallurgy

Supporting Fast Breeder Reactor Programme

Heavy Water & Allied Products

Societal Initiatives

बहुविध गतिविधियां
Multifold Activities

Nuclear Solvents

Environment Care

Technological Initiatives

स्वास्थ्य सेवा हेतु सामग्री
Materials for Healthcare
(पीईटी स्कैनिंग हेतु ऑक्सीजन-18 जल
^{18}O Water for PET Scanning;
कैंसर के उपचार हेतु डयूटेरियम क्षीण जल
Deuterium Depleted Water for Cancer Care)
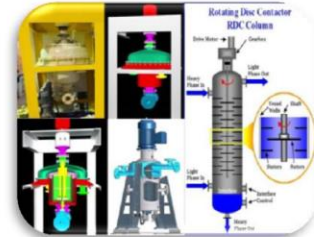
नए उपकरण, पदार्थों और प्रकियाओं का विकास तथा अभियांत्रिकी सेवाएं
Development of Novel Equipment, Materials & Processes and Engineering Services

सौर ऊर्जा का उपयोग **Harnessing Solar Power**
फ्लू गैस कंडीशनिंग **Flue Gas Conditioning**
वर्षा जल संचयन **Rain Water Harvesting**

www.hwb.gov.in

Bringing Tomorrow's Technology Today

COHERENT

COMPex
Most stable Excimer laser

Applications :
- PLD – Pulsed Laser Deposition
- Thin Wafer Processing

DEMCON

Pulse Laser Deposition Chamber

Applications :
- EY Applications
- Pt ALD on nanotubes for photocatalysis

BENEQ

Atomic Layer Deposition System
BENEQ TFS 200

Applications:
- Al2O3 on barrier applications
- HfO2, SiO2 and SiN for semiconductor applications

LIOPTEC
light is our profession

Pulsed Dye Laser
LiopStar

Applications:
- Laser-induced fluorescence: LIF
- Light detection and ranging: LIDAR

Litron Lasers

Litron LPY Series
High Energy Laser

Applications :
- OPO Pumping
- Dye Laser Pumping
- Spectroscopy
- LIBS
- LIDAR
- LIDT
- Laser Shock Peening

NANOMAGNETICS INSTRUMENTS

Vibrating Sample Magnetometer

Applications :
- Measurement of Magnetisation "M" with Applied field "H"
- Measurement of Magnetisation "M" with Temperature "T"

COHERENT

ASTRELLA
Femtosecond Amplifier

Applications:
- Time-resolved Spectroscopy
- Multidimensional Spectroscopy
- THz Spectroscopy
- fs Micromachining

LIGHT CONVERSION

HARPIA : SPECTROMETER

Applications:
- Transient absorption and reflection in bulk and microscopy
- Multi-pulse transient absorption and reflection

---

www.laserscience.co.in   info@laserscience.in   +91 77100 12972   laserscienceservices